THE UNIVERSITY OF CHICAGO

NUCLEON MASS AND CHARGES WITH LATTICE QUANTUM CHROMODYNAMICS

A DISSERTATION SUBMITTED TO
THE FACULTY OF THE DIVISION OF THE PHYSICAL SCIENCES
IN CANDIDACY FOR THE DEGREE OF
DOCTOR OF PHILOSOPHY

DEPARTMENT OF PHYSICS

BY
YIN LIN

CHICAGO, ILLINOIS
JUNE 2021

Table of Contents

List of Figures

List of Tables

Acknowledgments

“No man is an island” is a quote that comes into my mind, as I ponder how can I possibly encapsulate all the supports, either directly or indirectly, that I have received in my Ph.D. career both at the University of Chicago and Fermilab in few short paragraphs. But one can always try.

I will be always grateful to my advisor, Andreas Kronfeld, who was willing to take on the difficult task of mentoring a student. Your mentoring over the years has made my Ph.D. experience a pleasant and productive one. I would like to thank my thesis committee members – Edward Blucher, LianTao Wang, and Pavel Wiegmann – for their helps in making this degree possible. I would like to especially thank LianTao Wang for handling administrative tasks at the university so I can work at Fermilab.

I have learned many valuable lessons from members of the Fermilab Lattice and MILC collaborations and other colleagues that I have worked and interacted with including, but not limited to, Aida El-Khadra, Alexei Strelchenko, Carleton DeTar, Rich Brower, Ruth Van de Water, Steve Gottlieb, Will Jay, and Zech Gelzer. Their collective wisdom is embodied throughout the text of this work.

Then there are friends: Aaron Meyer, Chih-Kai Chang, Ciaran Hughes, Holger Schulz, Jessica Turner, Jim Simone, Jody Chou, Mao Tian Tan, Monica Martinez, Olivia Vizcarra, Xining Zhang, and Yikun Wang. “Maybe the real treasure was the friends we made along the way?”[1]

Without the supports from my parents and brother, I would not be who I am today. So, thank you. And of course, I have to thank Tianyue, who is sitting right next to me because of the pandemics. This thesis is for you, so please read it carefully from cover to cover.

As of the completion date of the thesis, countless lives have been upended by or lost to the ongoing COVID-19 pandemics. This work is dedicated to all these people, as well as

---

[1] It is a common internet phrase with complicated origins.

many others who are working tirelessly to restore a sense of normalcy in this crazy time.

Abstract

Neutrino oscillation experiments are designed to measure neutrino masses and mixing parameters by scattering them off nuclei such as carbon, oxygen, and argon in detectors. Predictions of neutrino-nuclei cross sections from the Standard Model are needed to extract these parameters, but their theoretical uncertainties remain large due to the complexity of nuclear and hadronic physics. This situation needs to be improved in order to satisfy the precision needs of future experiments.

In this dissertation, we focus on working towards a first-principles calculation of the nucleon axial form factor with lattice quantum chromodynamics (QCD). Nucleon axial form factor, which parametrizes the weak responses of a proton or neutron, is difficult to measure experimentally, and it is a dominant uncertainty in neutrino-nuclei cross-section calculations for incoming neutrino energies at around 1 GeV. So a theoretical calculation with lattice QCD provides a non-ambiguous determination of the form factor that could help reducing the uncertainty.

The notorious signal-to-noise problem renders calculations of nucleon observables computationally intensive in lattice QCD. In this work, we investigate the use of staggered fermions in nucleon calculations. Staggered fermions are the most computationally efficient fermion discretization in lattice field theory, but certain theoretical issues have so far prevented their applications to nucleon physics. As a stepping stone towards a full calculation of the nucleon axial form factor, this dissertation provides a comprehensive theoretical framework on how to calculate the nucleon mass, vector charge, and axial charge with staggered fermions, together with numerical results demonstrating the methodology. This framework can be generalized to the form factor calculation that will appear in the near future.

Chapter 1

Introduction

1.1 Probing new physics with neutrinos

Within the Standard Model of particle physics, masses of elementary particles are derived from the vacuum expectation value of the Higgs field after spontaneous symmetry breaking. The Higgs mechanism generates equal masses for both left- and right-handed particles, and because we have yet to observe any right-handed neutrinos, this would then imply that (left-handed) neutrinos must be massless to conform to the Standard Model. In 1998, the Super-Kamiokande (Super-K) experiment announced the first discovery of masses to neutrinos [5] through detecting atmospheric neutrino oscillations. To understand why this result demonstrates neutrinos have non-zero masses, we have to understand why neutrinos oscillate. Similar to six flavors of leptons, neutrinos also come into six different flavors: ν_e, $\bar{\nu}_e$, ν_μ, $\bar{\nu}_\mu$, ν_τ, $\bar{\nu}_\tau$. Six flavors of neutrinos are interaction eigenstates of the Standard-Model Lagrangian but not the mass eigenstates. A direct consequence of this is that massive neutrinos have to transform into different interaction eigenstates as they propagate through space. The mixing of neutrino flavors are characterized by the Pontecorvo–Maki–Nakagawa–Sakata (PMNS) matrix, which is similar to the Cabibbo–Kobayashi–Maskawa (CKM) matrix in the quark sector except the CKM matrix is found in experiments to be mostly diagonal whereas the PMNS matrix is found to have large off-diagonal entries; see [6] for estimates of neutrino parameters from global analyses of oscillation experiment data as of 2020. The existence of small neutrino masses is therefore one of the few telltales of physics beyond the Standard Model.

What makes neutrinos even more interesting is the fact they also play important roles in cosmology and astrophysics. For one, massive relic neutrinos from the Big Bang is one of the known components of hot and warm dark matters that leaves imprints on many cosmological observables such as the cosmic microwave background spectrum; see [7, 8] for reviews on this topic. Neutrinos are also emitted in abundance in core-collapse supernovae. Depending on the precise condition in which the star collapses, the event may be difficult to detect electromagnetically so studying the neutrino spectrum is irreplaceable to understand the nature of such phenomenon [9]; also, a possible solution to the puzzle of the observed asymmetry between particle and antiparticles in our Universe is provided by the leptogenesis [10], which introduces new species of neutrinos through the seesaw mechanism; see [11] for a review.

Motivated by the tremendous phenomenological interest, many experiments are currently underway or planned to investigate many facets of neutrinos with different sources. For examples, the neutrinoless double-beta-decay experiments [12], such as CUORE [13], Gerda [14], KamLAND-Zen [15], and KATRIN [16], are designed to search for double beta decays of heavy nuclei. If experiments are able to discover such events without emitted neutrinos, we can confirm that neutrinos are Majorana fermions through the black box theorem [17]. This will be the first observed Majorana particle in the Nature. The absolute masses, as opposed to mass squared differences, of neutrinos can also be constrained; see the latest results in [18]. Another example is neutrino oscillation experiments, such as DUNE [19], JUNO [20], NOvA [21], and MicroBooNE [22], which measure neutrino fluxes produced by either nuclear reactors or particle accelerators to extract neutrino oscillation parameters. Many of these aforementioned experiments are also looking for atmospheric, solar, and cosmic neutrinos which can provide better estimates on neutrino parameters, help understand the working mechanisms of those neutrino sources, or provide hints towards beyond-the-Standard-Model physics.

1.2 Neutrino oscillation experiments and neutrino-nuclei cross sections

This thesis is motivated primarily by the need of the future long-baseline neutrino experiment DUNE. The Deep Underground Neutrino Experiment (DUNE) is designed to deliver a neutrino beam of unprecedented intensity by upgrading the existing accelerator facility at Fermilab to investigate the fundamental properties of neutrinos. Neutrino masses and mixing parameters are extracted by comparing event rates at both the near and far detectors located 1300 km apart. Given that the incoming neutrinos are nearly invisible, oscillation experiments measure the final states of neutrino interactions and, through the use of Monte-Carlo event generators such as GENIE [23], GiBUU [24], and NuWro [25], reconstruct probabilistic distributions of neutrino events based on the observed kinematics and topologies to infer neutrino energies. A relatively heavy nucleus, ^{40}Ar, is used in the DUNE time-projection chamber to maximize the sensitivity to the weak interaction, so an accurate determination of the neutrino-argon cross sections for energy reconstruction is necessary to unleash the full discovery potential of DUNE. This poses significant challenges to our understanding of nuclear physics. Further, the sooner such results mature, the better chance they have of informing analyses at current and near-term oscillation experiments, such as ICARUS [26], MicroBooNE, MINERvA [27], NOvA, SBND [28], and T2K [29].

Calculating the neutrino-nucleus cross section is a multi-scale problem. In the energy regime from about 0.5 to 5 GeV relevant to DUNE, three distinct neutrino-nucleus scattering mechanisms come into play: quasielastic scattering (QE), resonance production (RES), and deep-inelastic scattering (DIS) [30]. Figure 1.1 shows the total neutrino and antineutrino cross sections per nucleon for all three regions and how they overlap. In future long baseline experiments, the theoretical uncertainties on cross sections will become the dominant sources of systematic errors [31], so better cross-section estimates to within a few percent of all interaction processes are needed to avoid limiting the precision of extracted neutrino parameters. This is a challenge that requires ingenious solutions from both experimentalists and theorists; see [30] for a review of the current status.

In this dissertation, we focus on how lattice quantum chromodynamics (QCD) calculations can contribute to our understanding of neutrino-nucleus scattering. Lattice QCD, first proposed by Kenneth Wilson in 1974 [32], is a non-perturbative regularization scheme of QCD on Euclidean lattices. Any lattice results with complete error budgets should be treated as the predictions of QCD. Even though ^{40}Ar nucleus is too complex to be simulated on the lattice directly, lattice QCD can provide systematically improvable calculations based solely on QCD, which will serve as inputs to nuclear models and are essential to reduce the cross-section systematics to the required level. The USQCD collaboration has published a white paper [33] that demonstrates how lattice-QCD predictions are integral parts of the cross-section calculations in all three aforementioned neutrino-nuclei scattering processes. In some cases, such as the overlap between the RES and DIS regions, lattice QCD is the *only* tool that is able to produce consistent predictions. We will come back to a quick overview of the lattice QCD methodology in Section 1.4.

This dissertation is part of a research program aiming at providing a first-principles calculation of the nucleon axial form factor with quantifiable uncertainties to reduce systematic errors in the QE scattering region. Neutrino-nucleus QE scattering is the dominant interaction process for neutrino energies between few MeV and about 1 GeV. It is mediated by a weak current exchange contributed by both neutral- and charged-current (CC) interactions. Technical difficulties in lattice QCD render the neutral-current calculations more challenging compared to their CC counterparts. Neutral-current interactions are also less important in oscillation experiments because the scattered neutrinos cannot be observed, so only the charged-current QE (CCQE) cross section will be considered in this work. The complete description of neutrino-nucleus CCQE cross section requires careful nuclear physics modeling. A recent paper [34] demonstrated the successful calculation of the CCQE cross

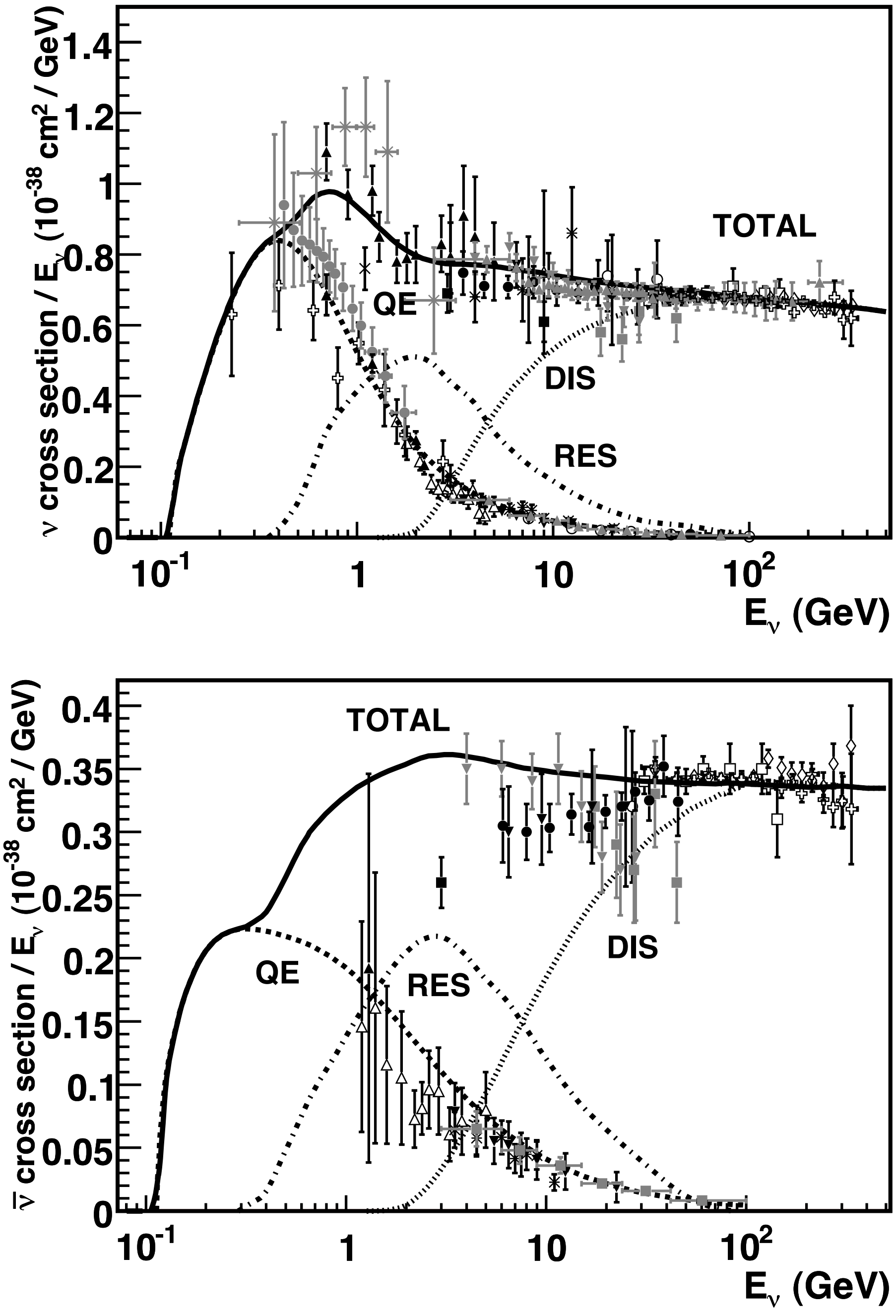

Figure 1.1: Total neutrino and antineutrino cross sections per nucleon on a isoscalar target as functions of incoming energy reproduced from [1]. Data points show results from different experiments.

section of ^{12}C with a nuclear *ab inito* method. In their work, they highlighted the need for a more precise lattice-QCD calculation of the nucleon axial form factor for their models, stating "first-principles LQCD calculations of nucleon (and, possibly, nucleon-to-Δ) electroweak form factors potentially have a significant impact on calculations of neutrino-nucleus cross sections, since these form factors constitute essential inputs to the nuclear CC."

The nucleon axial form factor parametrizes the weak response of a nucleon and is responsible for a large theoretical uncertainty of the neutrino-nucleon CCQE scattering depicting in figure 1.2. Three different deuterium bubble chamber experiments [35–37] performed in the 1970s and 80s have access to the nucleon cross section with small nuclear corrections. Modern neutrino experiments use heavy nuclei as targets, so the form factor cannot be cleanly extracted without significant systematics from nuclear modeling. Recent studies [38, 39] found that the uncertainties of the nucleon axial form factor were underestimated by previous analyses, and with no planned experiments in sight, lattice-QCD calculations are then needed to achieve the precision goals of DUNE. Note that the vector form factor also contributes to the electroweak cross section in figure 1.2. However, it can be extracted precisely from high statistics study of electron-nucleon scattering data from experiments such as the ones conducted by the A1 [40] and PRad [41] collaborations.[1] Once we have the techniques to properly control systematic errors in the axial form factor calculation, the same techniques can be easily generalized to a calculation of the vector form factor in the future.

There have been many activities in the lattice-QCD community to calculate the nucleon axial form factor (for example, see [43–45]), but the statistical and systematic uncertainties on those results are large due to high computing costs to calculate nucleon observables. This work focuses on working towards building the theoretical foundation for a calculation of the nucleon axial form factor with fully controlled systematics in lattice QCD in the near future.

---

1. It was pointed out recently in [42] that there are still unresolved systematic errors in vector form factor global analyses due to tensions between different datasets. This leads to larger-than-expected uncertainties on the vector form factor, comparable to those of the axial form factor, at large energy transfers. It is therefore desirable to calculate it with lattice QCD to cross check results.

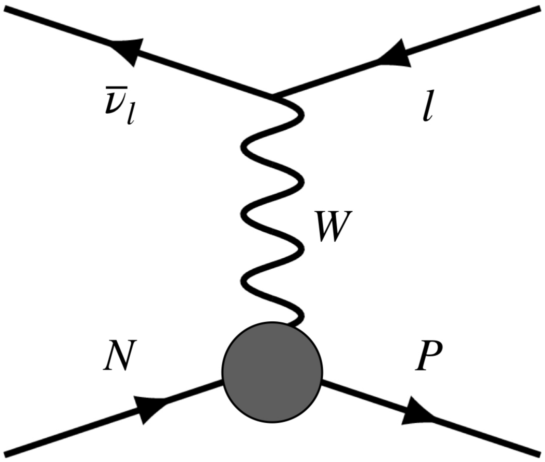

Figure 1.2: Charged current (anti)neutrino-nucleon interaction. N, P, $\bar{\nu}_l$, and l are neutron, proton, antineutrino, and lepton, respectively. The blob denotes the non-perturbative contributions from vector and axial form factors which are amenable to lattice QCD calculations.

Our work distinguishes itself from others by the use of the staggered fermion discretization which is one of the most efficient lattice fermions to simulate. Despite the appeal of staggered fermion simulations, their applications to nucleon observables are complicated by unresolved theoretical issues and no nucleon matrix element calculations had been performed with this formalism. In this work, we present the first-ever calculation of the nucleon mass, vector charge, and axial charge with the staggered formalism based on our results in [2, 3]. The nucleon axial charge $g_A = 1.2756(13)$ [46] is the nucleon axial form factor at zero momentum transfer at zero momentum that is related to the neutron lifetime of 15 minutes. We also calculate the conserved nucleon vector charge $g_V = 1$ which serves as a validation observable for our new lattice methodology. These three observables are necessary stepping stones towards a full calculation of the nucleon axial form factor, and our results are consistent with expectations. This work enables calculations of the nucleon axial form factor with staggered fermions that we are currently working on. We expect the first full result on the nucleon axial form within the next couple of years from the publication date of this thesis.

1.3 Notations in this work

Throughout this work, we will use the natural units of particle physics by setting the speed of light and reduced Planck constant $c = \hbar = 1$. In addition, we will also adopt the lattice natural unit by setting the lattice spacing $a = 1$ unless explicitly shown. To restore dimensional quantities, we can simply insert unique combinations of c, $\hbar$, and a to the expressions.

1.4 A (short) introduction to lattice QCD

There are many excellent textbooks and preprints offering pedagogical introductions to lattice QCD (for example, see [47–52]). The goal of this section is therefore to only give a high-level overview of lattice QCD methodologies by highlighting some aspects of calculations that are important to this particular work. The materials presented here should give sufficient background to understand the rest of this thesis.

In the path integral formulation of the quantum field theory (QFT) [53] in the Euclidean metric, the expectation value of an observable $\mathcal{O}$ can be calculated via

$$\begin{aligned} \langle \mathcal{O} \rangle &= \int \mathcal{D}\psi \mathcal{D}\overline{\psi} \mathcal{D}A \left(\frac{e^{iS[\psi,\overline{\psi},A]}}{Z} \right) \mathcal{O}[\psi, \overline{\psi}, A], \\ Z &\equiv \int \mathcal{D}\psi \mathcal{D}\overline{\psi} \mathcal{D}A e^{iS[\psi,\overline{\psi},A]} \end{aligned} \tag{1.1}$$

where Z is the partition function, S is the action, ψ, $\overline{\psi}$ are fermion fields, and A is the gauge field. In calculations of hadron masses and matrix elements, we only need to consider two types of observables: two-point and three-point correlation functions (or simply correlators) which are defined by

$$\begin{aligned} C_{\mathrm{2pt}}(t) &\equiv \big\langle \mathcal{O}(t)\overline{O}(t=0)\big\rangle, \\ C_{\mathrm{3pt}}(t,\tau) &\equiv \big\langle \mathcal{O}(t)J(\tau)\overline{O}(t=0)\big\rangle \end{aligned} \tag{1.2}$$

where $t > \tau > 0$. $\overline{O}$ is a so-called source interpolating/creation operator which has the same quantum numbers as the state we want to study located at $t = 0$, and $O(t)$ is its sink counterpart located at t. $J(\tau)$ is a current operator located at τ and interacts with particles created by $\overline{O}$. Two-point correlators allow us to extract hadron energies, and three-point correlators allow us to extract matrix elements when combined with data from two-point correlators.

(1.1) in its present form is divergent and ill-defined. A regularization scheme is thus required to make predictions in not only the path integral but also in the canonical formulations of QFT. The most commonly used one is the $\overline{\mathrm{MS}}$ scheme based on the perturbative expansion with Feynman diagrams. Regardless of the regularization scheme used, physical observables should all agree with one another after renormalizations and removing regularizers. Many regularization schemes such as $\overline{\mathrm{MS}}$ and Pauli-Villar rely on theories having well-defined perturbative expansions at the energy range considered. For low-energy systems in QCD, however, the strong coupling is large due to asymptomatic freedom and there are no well-defined expansion parameters so perturbative regularization schemes cannot be applied. Rather, a non-perturbative regularization scheme is needed, which in this case is provided by discretizing the theory on a four-dimensional Euclidean lattice.

To obtain lattice regularized QCD, we start with (1.1), rotate the time coordinate to the imaginary axis (Wick rotation), and discretize the QCD action and observable using your preferred lattice action. This results in a discretized path integral

$$\begin{aligned}\langle \mathcal{O}_L \rangle &= \int \prod d\psi \prod d\overline{\psi} \prod dU \left(\frac{e^{-S_L[\psi,\overline{\psi},U]}}{Z} \right) \mathcal{O}_L[\psi,\overline{\psi},U], \\ Z &\equiv \int \prod d\psi \prod d\overline{\psi} \prod dU e^{iS[\psi,\overline{\psi},U]}\end{aligned} \tag{1.3}$$

where we are integrating over field values at all lattice sites. In the continuum QCD, the path integral in (1.1) is integrating over the $\mathfrak{su}(3)$ Lie-algebra valued fields A_μ. But on the lattice we work with gauge link fields U_μ that take values in the SU(3) Lie group. They are simply Wilson line operators or parallel transporters

$$U_\mu = e^{iaA_\mu} \quad (\mu = 1, 2, 3, 4) \tag{1.4}$$

which are simple to work with to preserve the exact gauge invariance even when we break the spacetime symmetry. Intuitively, we can think of fermion field ψ and $\overline{\psi}$ as living on the lattice sites and gauge links U_μ as links connecting different sites. Because of the Wick rotation, the factor in the bracket of (1.3) can now be interpreted as a probability density function (pdf) of a given fermion and gauge field configurations, which they are usually referred to as simply “gauge configurations” or “gluon configurations”. After performing importance sampling of the pdf, we obtain a set of gauge field configurations in which the observable can be calculated. The same observable has to be calculated on multiple “ensembles” – or sets of gauge configurations – with the same lattice action but different lattice parameters such as lattice spacing, quark masses[2], volumes, etc. QCD predictions can be obtained by first renormalizing results on all ensembles if necessary then extrapolating to a result at the physical quark masses (chiral extrapolation), infinite volume, and zero lattice spacing (continuum extrapolation). Here we summarize important steps in a lattice calculation:

---

[2] Simulations at unphysically high quark masses are much cheaper to perform due to smaller correlation lengths; see, for example, [54] for details. Many calculations, therefore, choose to simulate at multiple quark masses and extrapolate results to the physical point.

1. Determine the lattice gauge and fermion actions to use in simulations as long as they belong to the same universality class as QCD in the continuum limit $a \to 0$.
2. Generate multiple ensembles at different lattice bare parameters tuned to the critical surface.
3. Measure correlation functions on each lattice configuration in different ensembles.
4. Perform statistical analyses to extract physical observables in physical units.
5. Perform necessary extrapolations (chiral, continuum, and infinite volume) to obtain predictions of QCD.

There are many subtleties involving in each step of the process, and we have greatly simplified them here just to give an idea of the necessary ingredients that go into a lattice calculation. The bottlenecks for all lattice simulations right now are prohibitive costs involving steps 2 and 3 which limit the statistical precision of lattice results. Generating ensembles in step 2 is the more expensive of those two and it boils down to repeatedly solving for systems of linear equations $Ax = b$ for a large, sparse matrix A on the order of 10-million-by-10-million and applying numerical integrations. At small lattice spacing near the continuum limit, generating statistical independent samples becomes much harder due to the well-known phenomenon of critical slowing down. Fortunately, once the gauge ensembles are generated with large computing resources for a given lattice action, we can reuse them over and over again to measure different observables. In this work, we use the gauge ensembles generated by the MILC collaboration [4, 55].

Even when gauge ensembles are readily available, computing correlation functions in step 3 still requires a non-trivial amount of computing resources that are typically done on supercomputers for large lattices. The problem here is again solving for systems of linear equations with the same dimensions as in step 2. For nucleon observables we are interested in this work, the signal-to-noise ratios are exponentially damped for large t and τ in (1.2) due to well-known reasons [56, 57], so they require many more measurements on different gauge configurations to achieve the desired precision. We will come back to this problem when we discuss our work in Chapter 4.

The main novelty of this work comes from solving theoretical issues associated with calculating nucleon observables with staggered quarks and presenting the first numerical results using this formalism. This method has the potential to be one of the fastest nucleon simulations in lattice QCD, which could translate into the most precise measurement of nucleon properties in the near future. In the next section, we will briefly describe what the problems are and how we plan to tackle them in the rest of the chapters.

1.5 Problem statement

Discretizing fermions on the lattice is a complicated issue. In the continuum QCD, we have the free, Euclidean fermion action

$$S = \int d^4x \Big(\overline{\psi}(x)\gamma^\mu \partial_\mu \psi(x) + m\overline{\psi}(x)\psi(x) \Big) \tag{1.5}$$

To simulate it on the lattice, we have to choose an approximation to partial derivatives ∂_μ. The choice is not unique and one of the simplest one is the finite difference

$$\partial_\mu f(x) \approx \frac{1}{2a}\Big(f(x+\hat{\mu}) - f(x-\hat{\mu}) \Big) \tag{1.6}$$

(1.6) is the so-called naive quark discretization and it leads to a theory with $2^d = 16$, $d = 4$ fermions even though we only put one in (1.5). This is the well-known fermion doubling problem which is deeply intertwined with the difficulty in preserving chiral symmetry on the lattice. The Nielsen-Ninomiya no-go theorem [58–60] states that under some mild assumptions on the form of the action, the theory cannot be both chirally symmetric and free of fermion doublers. This is also the reason why we have yet to see any lattice regularizations of chiral gauge theories such as the Standard Model that work well; see [61–63] for reviews.

Fortunately, QCD is not a chiral gauge theory as the chiral symmetry here is a global one, but we still have to reduce the number of quarks to match what the Nature has provided to us. For Wilson fermions [32], this is done by explicitly breaking the chiral symmetry via an irrelevant operator to decouple fermion doublers; and for some others such as domain wall [64, 65] and overlap fermions [66, 67], their actions satisfy the Ginsparg-Wilson equation [68] which ensures the existence of a remnant chiral symmetry on the lattice.

In this work, the action of choice is the staggered fermion [69, 70]. This lattice discretization is special in that it represents quarks with one-component spinor fields instead of the usual four-component ones. In addition, it also has a remnant chiral symmetry on the lattice which has many additional benefits compared to non-chirally symmetric fermions. These two features have also made the staggered action one of the most efficient, if not the most efficient, lattice actions to simulate. However, the price we have to pay for is that fermion doublers are in fact not completely eliminated in this discretization. Instead of 16 fermion doublers in the naive quark action, we are now left with 4 fermion doublers which are degenerate in the continuum limit. They are usually called the four tastes of a staggered fermion. This is problematic as the Nature does not give us four degenerate quark species in QCD, so they must be removed.

The problem of redundant tastes can be partially dealt with in the ensemble generation process by employing the so-called fourth-root trick. We first integrate out fermions in (1.3) and rewrite it as

$$\langle \mathcal{O}_L \rangle = \int \prod dU \prod_i \det[D(m_i)] \left(\frac{e^{-S_g[U]}}{Z} \right) \mathcal{O}_L[U] \tag{1.7}$$

where D is the lattice Dirac operator, S_g is the gauge part of the action, and m_i are the explicit mass terms we put into the theory. Note that we have performed Wick contractions to remove the fermionic dependence of O_L. Each determinant factor represents one sea quark contribution with mass m_i in an undoubled theory but represents four degenerate sea quarks contributions for the staggered action. So in the so-called rooted staggered fermion simulation, each quark determinant is replaced by

$$\det[D(m_i)] \rightarrow \det[D(m_i)]^{1/4} \tag{1.8}$$

The rooted determinant is then expected to represent one sea quark contribution in the continuum limit. There was a debate in the mid 2000s about the validity of such a procedure in a field theory context [71–73]. Backed by many theoretical and numerical evidence, it is now believed that the rooting procedure gives the correct continuum limit of QCD and has since produced many results that are consistent with experiments; see, for example, [74–77].

The rooting procedure eliminates redundant fermion tastes in the sea, but it does not eliminate them in the valence sector. This is because when we try to calculate observables in (1.7) with rooted determinants, we still have to invert the Dirac operator to construct O_L according to the Wick theorem. Even though the sea action used for constructing quark determinants is undoubled, the valence action used for constructing O_L is agnostic about the rooting procedure, so there are still four valence tastes left. Now the question this thesis tries to answer is how can we relate observables calculated in this rooted-staggered-fermion theory to the ones in physical QCD without explicitly removing valence taste degrees of freedom? For mesonic observables, the answer is known for a long time [78, 79] and some of the most precise predictions there nowadays are calculated with staggered fermions [80]; for nucleon observables, there were some initial work on relating baryon masses calculated with staggered fermions to their physical counterparts [81, 82] but the progress stalled ever since. This has so far prevented any calculations of nucleon matrix elements with staggered fermions.

In this work, we extend the arguments in [81, 82] to nucleon matrix elements and show, for the first time, i) a complete calculation of the nucleon mass based on those two references and ii) how to calculate nucleon vector and axial charges with a method which relies on the generalized Wigner-Eckart theorem of SU(4) taste symmetry that we developed. Materials here are based on our published work of [2, 3] but we have provided a more detailed account of the group theory aspect of our calculations.

The rest of the chapters are organized as follows: in Chapter 2, we provide an introduction to the group theory of SU(4) taste group and show how to relate staggered observables to physical QCD observables with the generalized Wigner-Eckart theorem in the continuum limit; in Chapter 3, we study the staggered action in details on the lattice to derive nucleon creation/annihilation operators and their continuum quantum numbers. In combination with results in the previous chapter, a complete description of how to calculate nucleon matrix elements with staggered fermions can be obtained; in Chapter 4, we highlight some numerical computations on the nucleon mass and charges appearing in [2, 3] using results derived in previous two chapters; and finally in the last chapter, we give a summary and future directions of this work.

Chapter 2

On SU(4) ⊃ SU(2) × SU(2) symmetries and staggered observables

We learned in Section 1.5 that QCD simulations with staggered valence quarks and rooted staggered sea quarks result in a theory, which will be oftentimes referred to as staggered QCD to distinguish it from the actual QCD, with one sea quark and four degenerate valence quarks for each quark species in the continuum limit. That is four too many quark tastes for QCD. Staggered simulations can only be useful to extract QCD observables if we are able to somehow deal with this extra multiplicity, which shows up as the extra SU(4) taste symmetry for valence quarks in the continuum action. For observables constructed from simple quark bilinears such as meson spectra, decay constants, and matrix elements, the relationship between QCD and staggered QCD can be inferred by rewriting staggered quark bilinears as four-component naive quark spinors – see [49, 78, 79, 83] for discussions. This approach, however, has proven to be difficult for staggered quark trilinears that are needed for baryon calculations because of large degrees of freedom in tastes.

We offer here a complementary approach that works well for both meson and baryon observables based on group-theoretical arguments. We can even extend its result to show that for any observables we want to calculate in QCD, there are corresponding observables in staggered QCD that we can simulate that would be identical up to normalization factors in the continuum limit. It turns out, these factors are easy to derive for mesonic observables but become non-trivial for baryonic observables. The idea of this approach is that for a given observable we want to calculate in QCD, there are single-taste observables made of valence quarks with the same taste, which otherwise are identical in constructions to the QCD one, that are equivalent. We can then apply a series of flavor and taste symmetry transformations to show that other non-single-taste observables can also be used to infer the QCD observable given we know how to relate the single-taste to non-single-taste observables, which are direct applications of the generalized Wigner-Eckart theorem.

We need two components for this approach to work: i) knowing the generalized Wigner-Eckart theorem in a basis that is the most convenient to work with, and ii) knowing the continuum flavor and taste quantum numbers for the nucleon states we create on the lattice. This chapter addresses the former question and Chapter 3 addresses the latter. Most current lattice simulations are done in the isospin limit where up and down quarks are identical. So in principle we need the generalized Wigner-Eckart theorem for SU(8). It turns out for our applications here, we can simplify the problems by solely performing SU(4) transformations in different SU(4) subgroups of SU(8), so the Wigner-Eckart theorem for SU(4) is all we need.

The theorem requires the knowledge Clebsch–Gordan (CG) coefficients which are basis-dependent quantities. Working with a suitable basis is crucial as using the "wrong" basis will greatly obscure the transformation properties of observables and render the analyses almost impossible; if we do not care about the basis, there are algorithms readily available [84] that computes SU(N) CG coefficients. In this work, we adopt a basis in which the states have definite quantum numbers in the subgroup of $\mathrm{SU}(2) \times \mathrm{SU}(2) \subset \mathrm{SU}(4)$. States created by lattice operators take simple forms in this basis as this is the first in many steps in breaking the taste symmetry under lattice discretization that will be discussed in Chapter 3.

Most group theory materials presented here are based on the discussions in [85], which have worked out all the relevant SU(4) CG coefficients in the context of nuclear physics. We will start with a short introduction to the SU(4) group theory then go into details on how they can be applied to relate observables in staggered QCD, especially the ones with SU(2) isospin symmetry, to experimental values.

2.1 Fundamentals of SU(4) ⊃ SU(2) × SU(2)

The fundamental representation of the SU(4) taste group is represented by 4-by-4 unitary matrices with unit determinants. We can write any SU(4) element U locally as

$$U = e^{iH} = e^{i\sum_{a=1}^{15} c_a \rho_a} \tag{2.1}$$

where H is a Hermitian matrix in the Lie algebra $\mathfrak{su}(4)$. H can then be expanded in the basis of $4^2 - 1 = 15$ Hermitian traceless generators ρ_i with real coefficients c_i, which satisfy the commutation relations

$$[\rho_a, \rho_b] = i f_{abc} \rho_c \tag{2.2}$$

with the totally antisymmetric structure constant $f_{abc} = f_{[abc]}$. Here we adopt the Einstein notation so the repeated indices are summed over.

We can find an explicit representation of ρ_a's by noticing that the four-dimensional fundamental representation of SU(4) is still irreducible[1] under the decomposition SU(4) → $\mathrm{SU}(2)_S \times \mathrm{SU}(2)_T$. In [85], SU(4) corresponds to the Wigner supermultiplet of spin (S) and isospin (T) symmetries in nuclear systems; whereas SU(4) corresponds to the taste symmetry of staggered quarks in this work. Nevertheless, we will keep the S and T subscripts in this chapter to distinguish those two SU(2) subgroups and their quantum numbers, but one should not take them literally as spins and isospins; in other chapters, we will use $\mathrm{SU}(2)_{D_4}$ and $\mathrm{SU}(2)_{\mathbb{Q}_8}$ to denote the same $\mathrm{SU}(2)_S$ and $\mathrm{SU}(2)_T$ subgroups, respectively.

This group decomposition means that the fundamental representation of SU(4) can be written as the tensor product of the two-dimensional fundamental representations of SU(2)

$$4 = \frac{1}{2} \otimes \frac{1}{2} \tag{2.3}$$

---

[1] We are not considering the decomposition in which the irrep is reducible and becomes $4 = \frac{1}{2} \oplus \frac{1}{2}$.

An irrep is always denoted by its dimension with a potential subscript of S (symmetric), A (antisymmetric), or M (mixed) to distinguish various irreps with the same dimensions, or a bar on top to denote a conjugate representation. However, an irrep of SU(2) is always denoted by the conventional spin notation. Because the Pauli matrices $\sigma_a, a = 1, 2, 3$ form a basis of the fundamental representation of $\mathfrak{su}(2)$, together with the identity matrix $\sigma_4 \equiv I$, their Kronecker products then form a fundamental representation of ρ_a in $\mathfrak{su}(4)$ given by

$$M_{\mu\nu} \equiv \sigma_\mu \otimes \sigma_\nu, \quad (\mu, \nu = 1, 2, 3, 4) \tag{2.4}$$

The identity matrix M_{44} is not one of the generators because it is not traceless. In practice, the most convenient basis of $M_{\mu\nu}$ that we will be using is defined via the ladder operators

$$\begin{aligned}
&S_0 \equiv \frac{1}{2}\big(\sigma_3 \otimes I\big),\ T_0 \equiv \frac{1}{2}\big(I \otimes \sigma_3\big),\ E_{00} \equiv \frac{1}{2}(\sigma_3 \otimes \sigma_3),\\
&S_\pm \equiv \frac{1}{2\sqrt{2}}\big(\sigma_\pm \otimes I\big),\ T_\pm \equiv \frac{1}{2\sqrt{2}}\big(I \otimes \sigma_\pm\big),\\
&E_{\pm\pm} \equiv \frac{1}{4}\big(\sigma_\pm \otimes \sigma_\pm\big),\ E_{0\pm} \equiv \frac{1}{2\sqrt{2}}\big(\sigma_3 \otimes \sigma_\pm\big),\ E_{\pm 0} \equiv \frac{1}{2\sqrt{2}}\big(\sigma_\pm \otimes \sigma_3\big)
\end{aligned} \tag{2.5}$$

where

$$\begin{aligned}
\sigma_- &= \sigma_1 - i\sigma_2,\\
\sigma_+ &= \sigma_1 + i\sigma_2
\end{aligned} \tag{2.6}$$

Note that the operators defined here are identical to those in Table. I of [85]. This matrix representation of ρ_a provides an easy way to compute the commutation relations between all 15 operators, and the structure constants are normalized to be either ±1 or 0.

2.2 Classifying states of SU(4) irreps

From (2.5) we can work out that four operators $\mathbf{S}^2 = S_0 + S_0^2 + S_- S_+$, $\mathbf{T}^2 = T_0 + T_0^2 + T_- T_+$, T_0, and S_0 are mutually commuting. So the states in an irrep of SU(4) can be specified by orthonormal kets

$$\left| [f] \left[j^S, m^S \right]_S \left[j^T, m^T \right]_T \right\rangle \tag{2.7}$$

where f is the irrep label, and j and m are the usual SU(2) spin quantum numbers for S or T operators. The states are constructed to eigenvectors of S_0 with eigenvalue of m^S, $\mathbf{S}^2$ with eigenvalue of $j^S(j^S+1)$, T_0 with eigenvalue of m^T, and $\mathbf{T}^2$ with eigenvalue of $j^T(j^T+1)$. It is clear that S and T can be derived from the operators in the $\mathrm{SU}(2)_S$ and $\mathrm{SU}(2)_T$ subgroups, respectively. The E operators are the unique ones that only exist in the full SU(4) group. As we shall see later, they can be used to construct step operators that raise or lower the values of j^S and j^T.

Irreps in this basis have definite quantum numbers in both $\mathrm{SU}(2)_S$ and $\mathrm{SU}(2)_T$ subgroups. This is particularly important for our purpose because $\mathrm{SU}(4) \to \mathrm{SU}(2)_S \times \mathrm{SU}(2)_T$ is the first step in decomposing the continuum symmetry group of the staggered action to the lattice one. Hence, all the states we excite on the lattice can be expressed simply in this basis. In Table 2.1, we have listed all the irreps of SU(4) that will be considered in this work, along with their irrep components $\left(j^S, j^T\right)$ in the $\mathrm{SU}(2)_S \times \mathrm{SU}(2)_T$ subgroup and Young diagrams. Similar to the eightfold way of SU(3) flavors, these irreps completely classify the tastes of single-particle staggered mesons and baryons.

As an example, the fundamental representation of SU(4) can be labeled by the four basis vectors

$$\left| \left[4 \right] \left[\frac{1}{2}, \pm\frac{1}{2} \right]_S \left[\frac{1}{2}, \pm\frac{1}{2} \right]_T \right\rangle \tag{2.8}$$

because $4 \to \left(\frac{1}{2}, \frac{1}{2}\right)$. Another example is the 15-dimensional adjoint representation of SU(4)

Table 2.1: SU(4) irreps and their irrep components $\left(j^S, j^T\right)$ in the $\mathrm{SU}(2)_S \times \mathrm{SU}(2)_T$ subgroup. These irreps completely classify the tastes of staggered mesons and baryons.

SU(4) irrep	$\mathrm{SU}(2)_S \times \mathrm{SU}(2)_T$ irrep components	Young diagram
1 (trivial, meson)	$(0,0)$	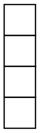
4 (fundamental)	$\left(\frac{1}{2},\frac{1}{2}\right)$	
$\bar{4}$ (anti-fundamental, baryon)	$\left(\frac{1}{2},\frac{1}{2}\right)$	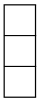
15 (adjoint, meson)	$(1,1)\oplus(1,0)\oplus(0,1)$	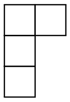
20_S (baryon)	$\left(\frac{3}{2},\frac{3}{2}\right)\oplus\left(\frac{1}{2},\frac{1}{2}\right)$	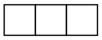
20_M (baryon)	$\left(\frac{3}{2},\frac{1}{2}\right)\oplus\left(\frac{1}{2},\frac{3}{2}\right)\oplus\left(\frac{1}{2},\frac{1}{2}\right)$	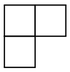

which can be labeled by the 15 basis vectors

$$\begin{aligned} &\left|[15]\left[1, m^S\right]_S[0,0]_T\right\rangle, \\ &\left|[15][0,0]_S\left[1, m^T\right]_T\right\rangle, \\ &\left|[15]\left[1, m^S\right]_S\left[1, m^T\right]_T\right\rangle \end{aligned} \tag{2.9}$$

because $15 \rightarrow (1,0)\oplus(0,1)\oplus(1,1)$.

A general irrep of SU(4) needs 6 quantum numbers from the 6 commuting operators to uniquely label its components. However, for all the irreps we will be working with in this work, those four quantum numbers are sufficient to label all their components.

2.2.1 Step operators and state normalizations

Consider the example of the basis of the adjoint representation defined in (2.9), we can apply $S_\pm$ and $T_\pm$ to raise or lower the z-component angular momenta m^S and m^T, respectively. However, for those kets to belong to the same irrep, this means that there exists a suite of new step operators O's that can raise or lower the total angular momenta j^S and j^T. A particular set is defined in Table II of [85]. As an example, let's consider the action of the step-up operator

$$O_{0+} = E_{0+} + S_- E_{++} (S_0 + 1)^{-1} \tag{2.10}$$

Using the representation in (2.5), we find the commutation relations

$$[S_0, E_{0+}] = 0,\ [S_0, S_-] = -S_-,\ [S_0, E_{++}] = E_{++} \tag{2.11}$$

which implies

$$[S_0, O_{0+}] = 0 \tag{2.12}$$

as expected. Similarly, the commutation relations

$$[T_0, S_0] = [T_0, S_-] = 0,\ [T_0, E_{0+}] = E_{0+},\ [T_0, E_{++}] = E_{++} \tag{2.13}$$

imply

$$[T_0, O_{0+}] = E_{0+} + S_- E_{++} (S_0 + 1)^{-1} = O_{0+} \tag{2.14}$$

So if we act O_{0+} on $\big|[15]\,[1,1]_S[0,0]_T\big\rangle$, we will find that

$$\begin{aligned} T_0 O_{0+}\Big|[15]\,[1,1]_S[0,0]_T\Big\rangle &= [T_0, O_{0+}]\Big|[15]\,[1,1]_S[0,0]_T\Big\rangle \\ &= O_{0+}\Big|[15]\,[1,1]_S[0,0]_T\Big\rangle \end{aligned} \tag{2.15}$$

In other words,

$$O_{0+}\Big|[15]\,[1,1]_S[0,0]_T\Big\rangle \propto \Big|[15]\,[1,1]_S[1,1]_T\Big\rangle \tag{2.16}$$

We can repeat the same exercise with $\mathbf{T}^2$ and $\mathbf{S}^2$ to further confirm (2.16). In general, if we apply a step operator to a state with $j^S = m^S$ and $j^T = m^T$, it will raise and/or lower j^S, m^S and/or j^T, m^T by one unit. The resulting state will be zero, however, if it is not one of the states in the irrep, just like how applying the raising operator to the highest weight states in SU(2) will be zeros.

The step operators are key ingredients for constructing CG coefficients. But to uniquely determine the action of O's onto the basis kets, we need to adopt a set of phase conventions to normalize the states. In the SU(2) case, the Condon-Shortley convention [86] is used throughout the literature that defines the commonly seen CG coefficients. However, no such consensus exists for other SU(N) groups partly because there is not a single natural basis to use. The most popular one is the Gelfand-Tsetlin basis and there is a program [84] that can readily compute their CG coefficients. But it is cumbersome to work in the Gelfand-Tsetlin basis and mapping it to our preferred basis is also difficult. In this work, we will follow the same normalization conventions as defined in [85].

2.2.2 Continuum staggered meson irreps of SU(4)

In the seminal work [87, 88] of Murray Gell-Mann and Yuval Ne'eman in 1961, they proposed to understand the observed hadron spectrum of QCD using irreps of SU(3). Gell-Mann, inspired by the Noble Eightfold Path in Buddhism, coined the term "Eightfold Way" to describe this classification scheme that we are familiar with today.

The classification scheme is rather easy to understand from the modern perspective. We start with the approximate isospin symmetry of SU(3) where up, down, and strange quark have equal masses and transform in the fundamental 3 irreps of SU(3). The meson and baryon wavefunctions can be constructed from the tensor product of 3 irreps

$$\begin{aligned} 3 \otimes \bar{3} &= 8_M \oplus 1 \\ 3 \otimes 3 \otimes 3 &= 10_S \oplus 2 \cdot 8_M \oplus 1 \end{aligned} \tag{2.17}$$

So to understand the spectrum of staggered QCD, we also need to classify the states of staggered mesons and baryons starting with the fundamental staggered quark fields of SU(4). Staggered mesons can be constructed from the tensor product

$$4 \otimes \bar{4} = 1 \oplus 15 \tag{2.18}$$

If we denote the four tastes of a continuum staggered quark as

$$\psi = \begin{pmatrix} \psi_1 \\ \psi_2 \\ \psi_3 \\ \psi_4 \end{pmatrix} \equiv \begin{pmatrix} \left| [4] \left[\frac{1}{2}, \frac{1}{2}\right]_S \left[\frac{1}{2}, \frac{1}{2}\right]_T \right\rangle \\ \left| [4] \left[\frac{1}{2}, \frac{1}{2}\right]_S \left[\frac{1}{2}, -\frac{1}{2}\right]_T \right\rangle \\ \left| [4] \left[\frac{1}{2}, -\frac{1}{2}\right]_S \left[\frac{1}{2}, \frac{1}{2}\right]_T \right\rangle \\ \left| [4] \left[\frac{1}{2}, -\frac{1}{2}\right]_S \left[\frac{1}{2}, -\frac{1}{2}\right]_T \right\rangle \end{pmatrix} \tag{2.19}$$

where only the SU(4) labels are included. Other quantum numbers, such as flavors and colors, are ignored. We define a Hermitian matrix of tensor products $\Pi^{\mu\nu} \equiv \psi_\mu \bar{\psi}_\nu$. The state in the trivial representation is then proportional to its trace

$$\left| [1] \left[0, 0\right]_S \left[0, 0\right]_T \right\rangle \propto \mathrm{Tr}(\Pi) = \sum_{\mu=1}^{4} \psi_\mu \bar{\psi}_\mu \tag{2.20}$$

where $\bar{\psi}^{\mu}$ transforms in the conjugate $\bar{4}$ representation. This state corresponds to the so-called tastes-singlet meson that plays important roles in determining the properties of flavor-singlet mesons [74]. As we will show in Section 2.3, the taste-singlet quark bilinears are also necessary for computing three-point correlators with flavor-singlet currents.

We can take out the singlet component by defining a Hermitian, traceless matrix $\widetilde{\Pi} \equiv \Pi - \frac{1}{4}\operatorname{Tr}\bigl(\Pi\bigr)$. Under a finite SU(4) transformation U, $\widetilde{\Pi}$ transforms by conjugation

$$\widetilde{\Pi} \to U\widetilde{\Pi}U^{\dagger} \tag{2.21}$$

which is the definition of the adjoint representation. (2.9) devises a standard basis for this irrep with definite $\mathrm{SU}(2)_S$ and $\mathrm{SU}(2)_T$ taste quantum numbers, so we have to find a set of 15 matrices $\widetilde{\Pi}^{\mu\nu}_{(a)}, a = 1, \cdots, 15$ from Π that maps onto that basis. Fortunately, we already have those matrices in hand – they are just the generators S's, T's, and E's defined in (2.5). Furthermore, these generators are constructed from the tensor products of SU(2) ladder operators, which transform as spin-1 spherical vectors with definite j and m quantum numbers. This means we can easily map those SU(4) generators or $\widetilde{\Pi}^{\mu\nu}_{(a)}$ onto the basis vectors $\bigl|[15]\,[1, m^S]_S [1, m^T]_T\bigr\rangle$, $\bigl|[15]\,[1, m^S]_S [0, 0]_T\bigr\rangle$, or $\bigl|[15]\,[0, 0]_S [1, m^T]_T\bigr\rangle$ according to their transformation properties.

In the staggered fermion literature (see, for example, [79, 83]), 16 tastes of staggered mesons (15 adjoint tastes + one singlet taste) are conventionally labeled by the products of Euclidean gamma matrices ξ_μ. If we write ξ_μ in the Dirac representation

$$\begin{aligned} \xi_i &= \sigma_2 \otimes \sigma_i, \\ \xi_4 &= \sigma_3 \otimes I \end{aligned} \tag{2.22}$$

that satisfies

$$\{\xi_\mu, \xi_\nu\} = 2\delta_{\mu\nu} I \tag{2.23}$$

we observe that the generator matrices in (2.5), hence the tastes of staggered mesons, can be written as linear combinations of ξ_μ and vice versa. For example, a staggered meson with ξ_4 taste corresponds to the S_0 operator which has quantum numbers $\big|[15]\,[1,0]_S\,[0,0]_T\big\rangle$. So the gamma matrices prescription is just another convenient method to label the states in the trivial and adjoint representations. In Table 2.2, we have enumerated all 16 tastes of the staggered mesons in both notations.

The third column of Table 2.2 represents either the eigenkets for staggered mesons or the quark-bilinear tensor operators for currents – they both transform identically under SU(4) rotations – even though we abuse the notations and write them as kets. The absolute normalizations of the kets/tensor operators are arbitrary, however, the relative normalizations (if there is one) are fixed again by the normalization conditions defined in [85]. For example, the ξ_5 taste transforms as

$$S_+ + S_- = \mathcal{T}^{[15][1,1]_S[1,0]_T} - \mathcal{T}^{[15][1,-1]_S[1,0]_T} \tag{2.24}$$

where a relative negative sign is placed between two tensor operators $\mathcal{T}$, which are denoted by their SU(4) quantum numbers in the superscripts. This can be understood in the context of SU(2) rotations, in which the spherical tensors can be defined as

$$V_+ = -\frac{1}{\sqrt{2}}J_+,\ V_- = \frac{1}{\sqrt{2}}J_-,\ V_0 = J_z \tag{2.25}$$

where J's are the angular momentum operators. $V_\pm$ transform as the plus and minus components of a spin-1 operator, and a relative negative sign and $1/\sqrt{2}$ are needed when we define them via the ladder operators $J_\pm$. Table I of [85] has listed all the proper normalizations for the tensor operators that we adopt here. The second column of Table I shows the non-zero entries of the gamma matrices, and the normalization factors in front, along with the sign in the fourth column, are needed to properly normalize the tensor operators $\mathcal{T}$ that will be needed by the Wigner-Eckart theorem. We will come back to this issue in the later section.

Table 2.2: Tastes of staggered mesons and their generators and quantum numbers. Basic kets/tensor operators are arbitrarily normalized.

Taste	Generators	Basis ket/Tensor Operator
1	I	$\left\|[1]\,[0,0]_S[0,0]_T\right\rangle$
ξ_4	S_0	$\left\|[15]\,[1,0]_S[0,0]_T\right\rangle$
$\xi_1\xi_2$	T_0	$\left\|[15]\,[0,0]_S[1,0]_T\right\rangle$
$\xi_3\xi_5$	E_{00}	$\left\|[15]\,[1,0]_S[1,0]_T\right\rangle$
ξ_5	$S_+ + S_-$	$\left\|[15]\,[1,1]_S[0,0]_T\right\rangle -$ $\left\|[15]\,[1,-1]_S[0,0]_T\right\rangle$
$\xi_4\xi_5$	$S_+ - S_-$	$\left\|[15]\,[1,1]_S[0,0]_T\right\rangle +$ $\left\|[15]\,[1,-1]_S[0,0]_T\right\rangle$
$\xi_2\xi_3$	$T_+ + T_-$	$\left\|[15]\,[0,0]_S[1,1]_T\right\rangle -$ $\left\|[15]\,[0,0]_S[1,-1]_T\right\rangle$
$\xi_1\xi_3$	$T_+ - T_-$	$\left\|[15]\,[0,0]_S[1,1]_T\right\rangle +$ $\left\|[15]\,[0,0]_S[1,-1]_T\right\rangle$
$\xi_3\xi_4$	$E_{+0} + E_{-0}$	$\left\|[15]\,[1,1]_S[1,0]_T\right\rangle -$ $\left\|[15]\,[1,-1]_S[1,0]_T\right\rangle$

(continue on the next page)

(Table 2.2, continued)

ξ_3	$E_{+0} - E_{-0}$	$\big\|[15]\,[1,1]_S[1,0]_T\big\rangle +$ $\big\|[15]\,[1,-1]_S[1,0]_T\big\rangle$
$\xi_1\xi_5$	$E_{0+} + E_{0-}$	$\big\|[15]\,[1,0]_S[1,1]_T\big\rangle -$ $\big\|[15]\,[1,0]_S[1,-1]_T\big\rangle$
$\xi_2\xi_5$	$E_{0+} - E_{0-}$	$\big\|[15]\,[1,0]_S[1,1]_T\big\rangle +$ $\big\|[15]\,[1,0]_S[1,-1]_T\big\rangle$
ξ_1	$E_{++} - E_{-+} + E_{+-} - E_{--}$	$\big\|[15]\,[1,1]_S[1,1]_T\big\rangle +$ $\big\|[15]\,[1,-1]_S[1,1]_T\big\rangle -$ $\big\|[15]\,[1,1]_S[1,-1]_T\big\rangle -$ $\big\|[15]\,[1,-1]_S[1,-1]_T\big\rangle$
ξ_2	$E_{++} - E_{-+} - E_{+-} + E_{--}$	$\big\|[15]\,[1,1]_S[1,1]_T\big\rangle +$ $\big\|[15]\,[1,-1]_S[1,1]_T\big\rangle +$ $\big\|[15]\,[1,1]_S[1,-1]_T\big\rangle +$ $\big\|[15]\,[1,-1]_S[1,-1]_T\big\rangle$
$\xi_1\xi_4$	$E_{++} + E_{-+} + E_{+-} + E_{--}$	$\big\|[15]\,[1,1]_S[1,1]_T\big\rangle -$ $\big\|[15]\,[1,-1]_S[1,1]_T\big\rangle -$ $\big\|[15]\,[1,1]_S[1,-1]_T\big\rangle +$ $\big\|[15]\,[1,-1]_S[1,-1]_T\big\rangle$

(continue on the next page)

(Table 2.2, continued)

$\xi_2\xi_4$	$E_{++} + E_{-+} - E_{+-} - E_{--}$	$\lvert[15]\,[1,1]_S[1,1]_T\rangle -$ $\lvert[15]\,[1,-1]_S[1,1]_T\rangle +$ $\lvert[15]\,[1,1]_S[1,-1]_T\rangle -$ $\lvert[15]\,[1,-1]_S[1,-1]_T\rangle$

In practice, the gamma matrix scheme is particularly useful for constructing correlators that conserve taste quantum numbers. Consider an n-point correlator consisting of operators that transform in the adjoint representation

$$C_{\text{npt}}^{(g_1,\cdots,g_n)} = \left\langle O_1^{(g_1)} \cdots O_n^{(g_n)} \right\rangle \tag{2.26}$$

$O_i^{(g_i)}$ is an operator with g_i taste. For example, using the definition of ψ in (2.19) we can construct the simplest ξ_5 taste quark bilinear

$$O^{(\xi_5)} = \overline{\psi}\xi_5\psi \tag{2.27}$$

where the spinor structure is irrelevant in this discussion, and therefore, omitted. Note that (2.26) can also accommodate for anti-quark operators because the adjoint representation is real. We claim that the correlator is non-vanishing if the product of gamma matrices is the identity matrix up to a sign, namely,

$$g_1 \times \cdots \times g_n = \pm I \tag{2.28}$$

In other words, the taste gamma matrices must "cancel out" in order to obtain non-zero answers. We can prove this by considering the n-point correlator as a tensor product of 15 irreps and decomposing it to irrep components

$$\underbrace{15 \otimes \cdots \otimes 15}_{\text{n times}} = 1 \overbrace{\oplus \cdots}^{\text{non-trivial irreps}} \tag{2.29}$$

The trivial irrep 1 can only appear once due to Schur's lemma. (2.29) implies that (2.26) can be written as a linear combination of a new set of operators $\widetilde{O}^{(r)}$ that transform as irreps of SU(4)

$$C_{\text{npt}}^{(g_1,\cdots,g_n)} = c_1\langle\widetilde{O}^{(g_1)}\rangle + \cdots + c_k\langle\widetilde{O}^{(g_k)}\rangle \tag{2.30}$$

c_j are some coefficients and the sum terminates at the k-th term. By the Great Orthogonality theorem,

$$\langle\widetilde{O}^{(r)}\rangle = 0 \quad \text{if} \quad r \neq \text{trivial irrep} \tag{2.31}$$

The only way to form the trivial irrep is to satisfy the condition in (2.28), so this proves our claim.

For example, suppose we want to study the mass of a ξ_5 taste meson from a two-point correlator. The only way to construct it is by enforcing the same taste for both operators

$$C_{\text{2pt}}^{(\xi_5,\xi_5)} = \langle O_1^{(\xi_5)} O_2^{(\xi_5)}\rangle \tag{2.32}$$

Similarly, if we want to study the matrix element of a ξ_5 taste meson with a ξ_4 taste current operator, the only non-vanishing three-point correlators will be

$$C_{\text{3pt}}^{(\xi_4\xi_5,\xi_4,\xi_5)} = \langle O_1^{(\xi_4\xi_5)} O_2^{(\xi_4)} O_3^{(\xi_5)}\rangle \tag{2.33}$$

and

$$C_{\text{3pt}}^{(\xi_5,\xi_4,\xi_4\xi_5)} = \langle O_1^{(\xi_5)} O_2^{(\xi_4)} O_3^{(\xi_4\xi_5)}\rangle \tag{2.34}$$

As we can see, the gamma matrix scheme simplifies all group-theoretical considerations into gamma matrix multiplications, and it is used ubiquitously in all staggered meson calculations. Unfortunately, this method only works if all operators in an n-point correlator transform in the trivial or adjoint representations. In calculating baryon matrix elements, only the current operator transforms in those representations, whereas the baryon creation and annihilation operators transform in other baryonic irreps such as 20_S or 20_M. We have to then carefully construct correlators that conserve the taste quantum numbers. This is why Table 2.2 will be particularly useful in those situations.

2.2.3 *Continuum staggered baryon irreps of SU(4)*

In the previous section, we have gone to great lengths to figure out the exact valence taste wavefunction of quark bilinears using the fundamental quark fields. As we will show later, it is particularly important to know the taste compositions of quark bilinears which are used for current insertions in matrix elements as it will affect the overall normalizations of physical observables.

However, it is not so important to know the precise valence taste wavefunction of staggered baryons for the observable of interest except for the so-called single-taste baryons [82], which are the baryons that consist of a single valence taste.[2] Knowing the quantum numbers of these single-taste baryons will allow us to normalize the matrix elements with the Wigner-Eckart theorem.

The 64 tastes of continuum staggered baryons transform as the tensor product

$$4 \otimes 4 \otimes 4 = 20_S \oplus 20_M \oplus 20_M \oplus \bar{4} \tag{2.35}$$

We can use Table 2.1 to enumerate all the basis kets for each irrep. If one inclines, he or she

---

[2] Analogously in QCD, we have single-flavor baryons of Δ^{++} and Δ^{-} which consist of only up or down quarks in their valence wavefucntions.

can compute the valence wavefunction of each ket by successively applying step and ladder operators to the highest weight states just like in SU(2). In this work, however, we will only need the single-taste valence wavefunctions listed in Table 2.3.

Table 2.3: Taste of single-taste baryons and their quantum numbers.

Taste	Basis ket
$\psi_1\psi_1\psi_1$	$\left\|[20_S]\,[\frac{3}{2},\frac{3}{2}]_S[\frac{3}{2},\frac{3}{2}]_T\right\rangle$
$\psi_2\psi_2\psi_2$	$\left\|[20_S]\,[\frac{3}{2},\frac{3}{2}]_S[\frac{3}{2},-\frac{3}{2}]_T\right\rangle$
$\psi_3\psi_3\psi_3$	$\left\|[20_S]\,[\frac{3}{2},-\frac{3}{2}]_S[\frac{3}{2},\frac{3}{2}]_T\right\rangle$
$\psi_4\psi_4\psi_4$	$\left\|[20_S]\,[\frac{3}{2},-\frac{3}{2}]_S[\frac{3}{2},-\frac{3}{2}]_T\right\rangle$

We notice two things from Table 2.3: all single-taste baryons reside within the totally symmetric representation 20_S because three valence quarks are identical, and their quantum numbers are such that $\left|j^S\right| = \left|j^T\right| = \left|m^S\right| = \left|m^T\right| = \frac{3}{2}$ which can be easily derived from the definitions in (2.19). Single-taste baryons play prominent roles in relating the observables of four-taste, staggered QCD to physical ones without taste degrees of freedom. We will come back and discuss how to achieve this in Section 2.3.

We will not list the valence taste wavefunctions for all states in this section, as they are not needed for our purposes here. But for completeness, we list the states with highest weights in Table 2.4. The relative normalizations of states are fixed, but their absolute normalizations are again arbitrary. Other states can be obtained by applying step operators defined in Table II of [85].

Table 2.4: Tastes of states with highest weights and their quantum numbers.

Taste	Basis ket
$\psi_1\psi_1\psi_1$	$\Big\vert[20_S]\,[\frac{3}{2},\frac{3}{2}]_S[\frac{3}{2},\frac{3}{2}]_T\Big\rangle$
$\psi_1\psi_2\psi_1+\psi_2\psi_1\psi_1-2\psi_1\psi_1\psi_2$	$\Big\vert[20_M]\,[\frac{3}{2},\frac{3}{2}]_S[\frac{1}{2},\frac{1}{2}]_T\Big\rangle$
$\psi_1\psi_2\psi_1-\psi_2\psi_1\psi_1$	$\Big\vert[20_M]\,[\frac{3}{2},\frac{3}{2}]_S[\frac{1}{2},\frac{1}{2}]_T\Big\rangle$
$\sum_{i,j,k=1}^{3}\epsilon_{ijk}\psi_i\psi_j\psi_k$	$\Big\vert[\bar{4}]\,[\frac{1}{2},\frac{1}{2}]_S[\frac{1}{2},\frac{1}{2}]_T\Big\rangle$

2.3 Clebsch–Gordan coefficients, Wigner-Eckart theorem, and physical observables

The goal of this work is to compute physical observables, such as masses, decay constants, and matrix elements, with the staggered action. For example, after performing analyses to eliminate lattice systematic errors (finite lattice spacing, finite volume, excited contamination, etc.), we arrive at a matrix element

$$M = \langle r_2|J^{(r_3)}|r_1\rangle \tag{2.36}$$

The bra and ket are mesons or baryons transforming in the r_2 and r_1 irreps of SU(4), respectively, and $J^{(r_3)}$ is a quark bilinear that transforms in the r_3 irrep. In this example, let

$$\begin{aligned} |r_1\rangle = |r_2\rangle &= \left|\left[20_S\right]\left[\frac{1}{2},\pm\frac{1}{2}\right]_S\left[\frac{1}{2},\pm\frac{1}{2}\right]_T\right\rangle, \\ J^{(r_3)} &= \overline{\psi}\xi_3\xi_5\psi \end{aligned} \tag{2.37}$$

Now the question is how can we, if at all, relate the result of (2.37) to the physical QCD one? Fortunately, this can be done since there are no gluon exchanges in the continuum staggered QCD that can alter the tastes of quarks (see, for example, [83]). So if all the operators are constructed from staggered quarks of the same tastes, we know the correlator must coincide with the physical ones; on the other hand, if the hadrons in a correlator are not of single tastes as in (2.37), we can still apply the Wigner-Eckart theorem to rotate it to the single-taste ones with appropriate Clebsch–Gordan coefficients.

In the next section, we will provide a quick overview of the Clebsch–Gordan coefficients and Wigner-Eckart theorem of SU(4). In Section 2.3.3 and 2.3.4, we will examine observables with meson and baryons and show how to apply the theorem we just learned to extract physical observables.

2.3.1 Clebsch–Gordan coefficients and the Wigner-Eckart theorem of SU(4)

Clebsch–Gordan (CG) coefficients (or Wigner coefficients as called in [85]) are the factors appearing in front of the state when we decompose the tensor product of two irreps to its irrep components. In SU(2), they are given by the inner product

$$\langle j_1, m_1; j_2, m_2 \big| J, M \rangle \tag{2.38}$$

where m_1, m_2, and M are the z-component angular momenta, and j_1, j_2, and J are the total angular momenta. Following the same notation, SU(4) CG coefficients are given by [85]

$$\Big\langle [r_1]\,[j_1^S, m_2^S]\,[j_1^T, m_1^T]; [r_2]\,[j_2^S, m_1^S]\,[j_2^T, m_2^T] \;\Big|\; [r_3]\,[J^S, M^S]\,[J^T, M^T] \Big\rangle_\rho \tag{2.39}$$

where m's and M's are again z-component angular momenta, and j's and J's are total angular momenta. r's are the irrep labels. The S and T superscripts differentiate between quantum numbers in the $\mathrm{SU}(2)_S$ and $\mathrm{SU}(2)_T$ subgroups. (2.39) is similar in structure to

(2.38) except for an additional index ρ which can take on the value of 1 and 2, depending on r_1, r_2, and r_3. We need this additional index in SU(4) because an irrep can appear more than once in the irrep components of a tensor product. For example,

$$15 \otimes 15 = 15 \oplus 15 \oplus \cdots \tag{2.40}$$

and

$$20_M \otimes 15 = \overline{20}_M \oplus \overline{20}_M \oplus \cdots \tag{2.41}$$

where the 15 irrep appears twice on the right-hand side of (2.40) and the $\overline{20}_M$ irrep (conjugate of the 20_M irrep) also appears twice on the right-hand side of (2.41). We then need ρ to distinguish between two unique irrep components. A general irrep of SU(4) needs six quantum numbers to completely classify their states. Even if we are to include the extra two quantum numbers in our basis, we will still need the extra label of ρ in (2.39). In comparison, the tensor product of any two irreps of SU(2) always decompose into irrep components that have multiplicities of one, so ρ label is not needed there. In this work, the ρ labels are needed only when $\{r_1, r_2, r_3\} = \{15, 15, 15\}$ or $\{r_1, r_2, r_3\} = \{20_M, 15, 20_M\}$.

We can further factor out (2.39) as products of SU(2) CG coefficients

$$\begin{aligned} &\Big\langle [r_1]\,[j_1^S, m_2^S]\,[j_1^T, m_1^T];\, [r_2]\,[j_2^S, m_1^S]\,[j_2^T, m_2^T] \;\Big|\; [r_3]\,[J^S, M^S]\,[J^T, M^T] \Big\rangle_\rho \\ &= \Big\langle [r_1]\,[j_1^S, j_1^T];\, [r_2]\,[j_2^S, j_2^T] \;\Big\|\; [r_3]\,[J^S, J^T] \Big\rangle_\rho \times \\ &\qquad \langle j_1^S, m_1^S; j_2^S, m_2^S | J^S, M^S \rangle \langle j_1^T, m_1^T; j_2^T, m_2^T | J^T, M^T \rangle \end{aligned} \tag{2.42}$$

The last two factors are the SU(2) CG coefficients for $\mathrm{SU}(2)_S$ and $\mathrm{SU}(2)_T$ subgroups, and the first factor is the coefficient unique to SU(4) that needs to be determined. The factorization is easy to understand if we consider a state with height weights for both of its SU(2) subgroups, namely,

$$\begin{aligned} &j_i^S = m_i^S, \; j_i^T = m_i^T \; (i=1,2), \\ &J^S = M^S = j_1^S + j_2^S, \; J^T = M^T = j_1^T + j_2^T \end{aligned} \tag{2.43}$$

In this case, the SU(2) CG coefficients are trivial and (2.42) simplifies to

$$\begin{aligned} &\Big\langle [r_1]\,[j_1^S, m_2^S]\,[j_1^T, m_1^T]; [r_2]\,[j_2^S, m_1^S]\,[j_2^T, m_2^T] \;\Big|\; [r_3]\,[J^S, M^S]\,[J^T, M^T] \Big\rangle_\rho \\ &= \Big\langle [r_1]\,[j_1^S, j_1^T]; [r_2]\,[j_2^S, j_2^T] \;\Big\|\; [r_3]\,[J^S, J^T] \Big\rangle_\rho \end{aligned} \tag{2.44}$$

The first factor in (2.42) is no more than the CG coefficients for states with height weights on both of its SU(2) subgroups. Given a set of conventions, we can find CG coefficients of SU(4) by applying step operators to obtain their recursion relations. The procedures and final results are described in details in [85] and will not be repeated here.

Once we have CG coefficients of SU(4), we can state the Wigner-Eckart theorem

$$\begin{aligned} &\Big\langle [r_1]\,[j_1^S, m_1^S]\,[j_1^T, m_1^T] \;\Big|\; \mathcal{T}^{[r_2][j_2^S, m_2^S][j_2^T, m_2^T]} \;\Big|\; [r_3]\,[J^S, M^S]\,[J^T, M^T] \Big\rangle \\ &= F\left([r_1]\,[j_1^S, j_1^T]; \mathcal{T}^{[r_2][j_2^S, j_2^T]}; [r_3]\,[J^S, J^T] \right) \times \\ &\qquad \langle j_1^S, m_1^S; j_2^S, m_2^S | J^S, M^S \rangle \langle j_1^T, m_1^T; j_2^T, m_2^T | J^T, M^T \rangle \end{aligned} \tag{2.45}$$

where

$$\begin{aligned} &F\left([r_1]\,[j_1^S, j_1^T]; \mathcal{T}^{[r_2][j_2^S, j_2^T]}; [r_3]\,[J^S, J^T] \right) \equiv \\ &\qquad \sum_\rho \Big\langle [r_1] \;\Big\|\mathcal{T}^{[r_2]}\;\Big\| [r_3] \Big\rangle_\rho \Big\langle [r_1]\,[j_1^S, j_1^T]; [r_2]\,[j_2^S, j_2^T] \;\Big\|\; [r_3]\,[J^S, J^T] \Big\rangle_\rho \end{aligned} \tag{2.46}$$

Similar to the reduced matrix element in SU(2), $\langle [r_1] \, \big\| \mathcal{T}^{[r_2]} \, \big\| [r_3] \rangle_\rho$ is the reduced matrix element of SU(4) that also depends on the ρ index. Note that the reduced matrix element is a function of r_1, r_2, and r_3 only, we can only obtain its value via direction simulations.

$\mathcal{T}^{[r_2][j_2^S,m_2^S][j_2^T,m_2^T]}$ is a tensor operator that has the same transformation properties as the ket $\left|[r_2]\,\left[j_2^S,m_2^S\right]_S\left[j_2^T,m_2^T\right]_T\right\rangle$. We write (2.45) as the product of the newly defined F function and the SU(2) CG coefficients. In this way, the F function contains all the ρ dependencies and is independent of the z-component angular momenta m's and M's.

The most common application of the Wigner-Eckart theorem is to relate two matrix elements that belong to the same irreps. For example, suppose we have two matrix elements

$$\begin{aligned} M_1 &= \left\langle [r_1]\left[j_1^S,m_1^S\right]\left[j_1^T,m_1^T\right] \,\middle|\, \mathcal{T}^{[r_2][j_2^S,m_2^S][j_2^T,m_2^T]} \,\middle|\, [r_3]\left[J_3^S,M_3^S\right]\left[J_3^T,M_3^T\right]\right\rangle, \\ M_2 &= \left\langle [r_1]\left[j_4^S,m_4^S\right]\left[j_1^T,m_1^T\right] \,\middle|\, \mathcal{T}^{[r_2][j_5^S,m_5^S][j_5^T,m_5^T]} \,\middle|\, [r_3]\left[J_6^S,M_6^S\right]\left[J_6^T,M_6^T\right]\right\rangle \end{aligned} \tag{2.47}$$

If we assume that

$$F\left([r_1]\,[j_1^S,j_1^T];\mathcal{T}^{[r_2][j_2^S,j_2^T]};\,[r_3]\left[J_3^S,J_3^T\right]\right)=\alpha F\left([r_1]\,[j_4^S,j_4^T];\mathcal{T}^{[r_2][j_5^S,j_5^T]};\,[r_3]\left[J_6^S,J_6^T\right]\right) \tag{2.48}$$

for some constant factor α, then we can relate M_1 and M_2 by

$$\frac{M_1}{M_2}=\alpha\frac{\langle j_1^S,m_1^S;j_2^S,m_2^S|J_3^S,M_3^S\rangle\langle j_1^T,m_1^T;j_2^T,m_2^T|J_3^T,M_3^T\rangle}{\langle j_4^S,m_4^S;j_5^S,m_5^S|J_6^S,M_6^S\rangle\langle j_4^T,m_4^S;j_5^T,m_5^S|J_6^T,M_6^T\rangle} \tag{2.49}$$

Up to the extra α factor, (2.49) is the direct generalization of the SU(2) Wigner-Eckart theorem to SU(4).

There is a couple of different scenarios where (2.48) is valid. The first case is where there are no irreps appearing more than once in the tensor product decomposition so the ρ label is redundant. α is then simply the ratio

$$\alpha=\frac{\left\langle [r_1]\,[j_1^S,j_1^T];\,[r_2]\,[j_2^S,j_2^T] \,\middle\|\, [r_3]\left[J_3^S,J_3^T\right]\right\rangle}{\left\langle [r_1]\,[j_4^S,j_4^T];\,[r_2]\,[j_5^S,j_5^T] \,\middle\|\, [r_3]\left[J_6^S,J_6^T\right]\right\rangle} \tag{2.50}$$

that we could look up in [85]. Even in the case where ρ indices are necessary due to the multiplicities, the symmetries of SU(4) CG coefficients could enforce (2.48). For example, from Table A4.6 of [85] we know that for all ρ

$$\begin{aligned}\Big\langle [15]\,[j_1^S, j_1^T]; [15]\,[j_2^S, j_2^T] \;\Big|\Big|\; [15]\,[0,1] \Big\rangle_\rho \\ = \Big\langle [15]\,[j_1^T, j_1^S]; [15]\,[j_2^T, j_2^S] \;\Big|\Big|\; [15]\,[1,0] \Big\rangle_\rho\end{aligned} \tag{2.51}$$

Then again,

$$\alpha = \frac{F\left([15]\,[j_1^S, j_1^T]; \mathcal{T}^{[15][j_2^S, j_2^T]}; [15]\,[0,1]\right)}{F\left([15]\,[j_1^T, j_1^S]; \mathcal{T}^{[15][j_2^T, j_2^S]}; [15]\,[1,0]\right)} = 1 \tag{2.52}$$

The two SU(2) factors in the SU(4) → $\mathrm{SU}(2)_S \times \mathrm{SU}(2)_T$ decomposition are indistinguishable from one another. Hence, the CG coefficients have to be invariant under switching the S and T labels as in (2.51). We will use this relabeling symmetry extensively in the following sections.

Lastly, (2.48) holds trivially if we only perform rotations in its SU(2) subgroups. In other words, $\alpha = 1$ if $j_1^S = j_4^S$, $j_2^S = j_5^S$, and $J_3^S = J_6^S$ in (2.50).

In general, (2.48) does not hold because there are two unknown reduced matrix elements $\left\langle [r_1] \,\middle|\middle|\, \mathcal{T}^{[r_2]} \,\middle|\middle|\, [r_3] \right\rangle_\rho$, $\rho = 1, 2$. We then need to compute two independent matrix elements with the same irreps and solve a system of two-by-two linear equations and get their values. Nevertheless, (2.48) holds for all our applications in this work.

We would also need to establish a normalization convention for the quark bilinears (tensor operators). Throughout this work, we assume the quark bilinears with definite gamma tastes are normalized in such a way that when you expand their valence wavefunctions using (2.19), the factor in front of each term is ±1. For example, the $\overline{\psi}\xi_4\xi_5\psi$ quark bilinear is equal to

$$\overline{\psi}\xi_4\xi_5\psi = -\overline{\psi}_1\psi_3 - \overline{\psi}_2\psi_4 + \overline{\psi}_3\psi_1 + \overline{\psi}_4\psi_2 \tag{2.53}$$

One can simply multiply the taste gamma matrix using the representation defined in (2.22) to obtain the valence wavefunction. This is how the lattice operators in Chapter 3 are normalized. However, this creates some slight complications for applying the Wigner-Eckart theorem – the theorem assumes that the tensor operators, or quark bilinears, are normalized in the canonical fashion as defined in the second and fourth columns of Table I in [85]. Using that table, we can write $\overline{\psi}\xi_4\xi_5\psi$ in terms of canonically normalized tensor operators

$$\overline{\psi}\xi_4\xi_5\psi = \sqrt{2}\Big(\mathcal{T}^{[15][1,1][0,0]} + \mathcal{T}^{[15][1,-1][0,0]}\Big) \tag{2.54}$$

which then can be passed to the Wigner-Eckart theorem. Normalizing quark trilinears for baryon operators is irrelevant as their normalizations cancel when we take the ratio of three- and two-points correlators to extract matrix elements.

This concludes our short introduction to the SU(4) CG coefficients and Wigner-Eckart theorem. The interested readers could read more about them in [85]. In the following two sections, we will apply these results to staggered mesonic and baryonic observables.

2.3.2 Adding SU(2)$_F$ flavor quantum numbers

All simulations in this work are done the in SU(2)$_F$ isospin limit in which the up and down quarks have equal masses. This extra quantum number is crucial in relating staggered QCD matrix elements to the physical quantities. In the next few sections, we will consider operators with definite SU(2)$_F$ quantum numbers. The extra set of quantum numbers will be denoted with the extra $[j, m]_F$ label where j in the total isospin and m is the z-component isospin in the standard spin notation. We will also introduce vectors of up- and down-quark fields, U/D, in the taste space, with components of u_i/d_i, $i = 1, 2, 3, 4$.

It may seem that if we add the extra SU(2)$_F$ to the existing SU(4), we have to consider the full SU(8) Wigner-Eckart theorem with eight species of degenerate quarks in the continuum.

Fortunately, in all the problems we have encountered in this work, we can simply perform a series of SU(4) Wigner-Eckart rotations to achieve the same effects.

2.3.3 Staggered meson masses and matrix elements with $SU(2)_F$ quantum numbers

Mesonic operators and quark bilinears transform in either the trivial or 15 irreps. The mass of a meson m_g can be measured from the two-point correlator

$$C_{2\text{pt}}^{(g,g)}(t) = \langle O^{(g)}(t)\overline{O}^{(g)}(0)\rangle \sim \left(\langle\Omega|\overline{O}^{(g)}|\pi_g\rangle\right)^2 e^{-m_g t} \text{ (as } t \to \infty) \tag{2.55}$$

where g denotes the taste of quark bilinears and $\langle\Omega|\overline{O}^{(g)}|\pi_g\rangle$ is the real overlap factor between the ground state meson π_g and the vacuum $|\Omega\rangle$. g can be one of the fifteen gamma matrices plus the identity matrix. For a moment, we will assume the π_g is composed of valence quark and antiquark of different species, so no disconnected diagrams (quark and antiquark from the same meson annihilate to gluons) are contributing to the amplitude. By the trivial applications of the Wigner-Eckart theorem, we can conclude that meson in the adjoint irrep have degenerate masses in the continuum limit. We can also show that any mesons in the adjoint irrep are degenerate with the same physical mesons without taste quantum numbers in the continuum limit. Let's consider a correlator with $g = \xi_3\xi_5$ taste in the adjoint irrep. Using the quark fields defined in (2.19), we can write the correlator as

$$\begin{aligned} C^{(\xi_3\xi_5,\xi_3\xi_5)} &= \left\langle(\overline{q}_1 q'_1 - \overline{q}_2 q'_2 - \overline{q}_3 q'_3 + \overline{q}_4 q'_4)(\overline{q}'_1 q_1 - \overline{q}'_2 q_2 - \overline{q}'_3 q_3 + \overline{q}'_4 q_4)\right\rangle \\ &= \sum_{i=1}^{4}\left\langle \overline{q}_i q'_i \overline{q}'_i q_i \right\rangle \end{aligned} \tag{2.56}$$

where q_i and q'_i correspond to two different quarks with tastes $i = 1, 2, 3, 4$. In going from the first to second line, we use the fact that there are no taste-changing currents allowed in the continuum limit, so cross talks between different quark tastes are prohibited. Because each term in the second line of (2.56) involves only quarks with the same taste, it is equivalent to four times the result that one would get in the physical QCD when we remove the i indices. This multiplicative factor does not affect the meson mass, so the conclusion above follows.

In the absence of disconnected contributions, the same argument can be also applied to trivial taste mesons to show that mesons in both the trivial and adjoint irreps are degenerate, hence, physical. In general, if an observable is completely made of quarks of the same tastes, it is equal to that of the physical QCD. We will use these principles over and over again in the next few sections to derive staggered observables that are useful.

We can infer the physical overlap factor from (2.55) by

$$\left(\langle\Omega|O^{(g)}|\pi_g\rangle_{\mathrm{phy}}\right)^2 \equiv \frac{1}{4}\left(\langle\Omega|O^{(g)}|\pi_g\rangle\right)^2 \tag{2.57}$$

or

$$\langle\Omega|O^{(g)}|\pi_g\rangle_{\mathrm{phy}} \equiv \frac{1}{2}\langle\Omega|O^{(g)}|\pi_g\rangle \tag{2.58}$$

where 1/4 comes from our observation in (2.56). In the continuum limit, $\langle\Omega|O^{(g)}|\pi_g\rangle_{\mathrm{phy}}$ will become the overlap factor we want to compute in the physical QCD. The $1/\sqrt{N_t}$, $N_t = 4$ normalizing factor is known for a long time [78] and has been applied in many staggered calculations to correctly extract decay constants (see, for example, [77].) In addition to this group theoretical factor, our statement assumes that the quark bilinears are normalized in the way we defined at the end of Section 2.3.1. The overall normalizations of the two-point functions or the quark bilinears are not needed if we are only interested in masses.

If we now include isospin quantum numbers, there are two cases that we need to separately consider: isospin-1 and isoscalar targets. If we go back to our example in (2.56) and replace all the quark bilinears with isospin-1 operators $\overline{u}_i d$ or $u_i\overline{d}_i$, the conclusion remains unchanged

– all the states in the adjoint and trivial irreps have identical masses and are physical. Their overlap factors can be normalized with (2.58) to obtain the physical decay constants. Isospin-1, trivial taste mesons and isospin-1, adjoint taste mesons all live in the same irrep of SU(8) $\supset$ SU$(2)_F \times$ SU(4), so we can rotate an adjoint taste correlator to the trivial taste one.

However, the masses and decay constants of isoscalar mesons such as η or η' can be only obtained from operators with trivial tastes. To demonstrate this, let's consider replacing quark bilinears in (2.56) with isoscalar operators

$$C^{(\xi_3\xi_5,\xi_3\xi_5)}_{\text{isoscalar}} = \frac{1}{2}\big\langle(\overline{U}\xi_3\xi_5U + \overline{D}\xi_3\xi_5D)(\overline{U}\xi_3\xi_5U + \overline{D}\xi_3\xi_5D)\big\rangle \tag{2.59}$$

where

$$U \equiv \begin{pmatrix} u_1 \\ u_2 \\ u_3 \\ u_4 \end{pmatrix}, \quad D \equiv \begin{pmatrix} d_1 \\ d_2 \\ d_3 \\ d_4 \end{pmatrix}$$

are vectors of u_i and d_i respectively, and the 1/2 factor normalizes the isoscalar operators. Isoscalar mesons receive contributions from disconnected diagrams, but we realize that (2.59) does not have disconnected contributions as the traces of gamma matrices are zeros. However, if we only consider connected contributions, (2.59) similarly gives four times the physical QCD result. In general, operators with tastes will work equally well in estimating the connected contributions and we can write

$$C^{(g,g)}_{\text{isoscalar,conn.}} = 4C_{\text{conn.}} \tag{2.60}$$

The extra "conn." subscript for $C^{(g,g)}_{\text{isoscalar}}$ denotes the connected contribution to that correlator, and $C_{\text{conn.}}$ denotes the connected contributions to the physical QCD correlator. To incorporate disconnected contributions back to its amplitude, we can only calculate them with trivial taste operators

$$C^{(I,I)}_{\text{isoscalar,disconn.}} = \frac{1}{2}\big\langle(\overline{U}U + \overline{D}D)(\overline{U}U + \overline{D}D)\big\rangle_{\text{disconn.}} \tag{2.61}$$

The subscripts “disconn.” denote the disconnected contributions to the correlator. In the isospin symmetric limit,

$$\langle \overline{u}_i u_i \overline{d}_j d_j\rangle_{\text{disconn.}} = \langle \overline{u}_i u_i \overline{u}_j u_j\rangle_{\text{disconn.}} = \langle \overline{d}_i d_i \overline{d}_j d_j\rangle_{\text{disconn.}},\ (i,j = 1,2,3,4) \tag{2.62}$$

so (2.61) simplifies to

$$C^{(I,I)}_{\text{isoscalar,disconn.}} = 16 \times \frac{1}{2}\langle(\overline{u}_1 u_1 + \overline{d}_1 d_1)(\overline{u}_1 u_1 + \overline{d}_1 d_1)\rangle_{\text{disconn.}} = 16 C_{\text{disconn.}} \tag{2.63}$$

where $C_{\text{disconn.}}$ is the disconnected contributions to the physical QCD correlator. This relationship only holds if we use taste-singlet operators. Combining the results of (2.60) and (2.63), the isoscalar two-point correlators in the physical QCD can be calculated with staggered correlators by summing together the connected and disconnected contributions with different weights

$$C \equiv C_{\text{conn.}} + C_{\text{disconn.}} = \frac{1}{4} C^{(g,g)}_{\text{isoscalar,conn.}} + \frac{1}{16} C^{(I,I)}_{\text{isoscalar,disconn.}} \tag{2.64}$$

This linear combination between the taste-singlet and non-taste-singlet correlators have been studied and tested (see, for example, [74]), and it behaves as expected.

Why is it that only the isoscalar mesons require such special treatments? The answer is quite simple when we think in terms of SU(8) $\supset$ SU$(2)_F$ × SU(4) representation theory.

Isoscalar mesons with trivial tastes transform as the trivial irrep of SU(8). Correlators made of trivial irrep operators are special because they cannot be rotated to correlators made of other states, so their correct values can only be obtained from direct simulations with trivial-taste operators. The same principles apply whenever we encounter n-point correlators with isoscalar operators, and we must always use trivial-taste operators to correctly estimate their values.

We now shift our attention to matrix elements derived from three-point functions with isospin symmetries

$$M^{(g_1,g_2,g_3)}_{[j_1,m_1]_F[j_2,m_2]_F[j_3,m_3]_F} \equiv \big\langle [j_1,m_1]_F[g_1]\big| O^{(g_2)}_{[j_2,m_2]_F}\big|[j_3,m_3]_F[g_3]\big\rangle,\ g_1\times g_2\times g_3 = \pm I \tag{2.65}$$

where g_1, g_2, g_3 again denote the meson tastes, and $[j,m]_F$ denotes the isospin quantum numbers. To conserve tastes, the product of g's have to be the identity matrix up to a sign per our previous discussion. We will not consider isospin-singlet operator and states here - their physical matrix elements can only be estimated with taste-singlet operators. Suppose we are instead interested in calculating the matrix element

$$M^{(\xi_4\xi_5,\xi_4,\xi_5)}_{[1,0]_F[1,-1]_F[1,1]_F} \equiv \big\langle [1,0]_F[\xi_4\xi_5]\big|\overline{U}\xi_4 D\big|[1,1]_F[\xi_5]\big\rangle \tag{2.66}$$

where U/D is again a vector of up/down-quark field u_i/d_i, $i = 1,2,3,4$ in the taste space. We expand their valence wavefunctions using Table. 2.2 to obtain

$$M^{(\xi_4\xi_5,\xi_4,\xi_5)}_{[1,0]_F[1,-1]_F[1,1]_F} = \frac{1}{\sqrt{2}}\langle \overline{u}_1u_3 - \overline{d}_1d_3\big|\overline{u}_3d_3\big|\overline{d}_3u_1\rangle + \cdots \tag{2.67}$$

where "$\cdots$" denotes three other similar terms and $1/\sqrt{2}$ is a normalization factor for the bra wavefunction. We realize that the taste subscript on each quark is redundant – up-ness and down-ness of the quark fields have already set them apart. For instance, writing $\overline{d}_1u_3$ is equivalent to writing $\overline{d}u$ since up and down quarks are already different. Removing the taste indices will then have no effects in the values of the matrix element, so we can establish the relationship between physical and staggered matrix elements

$$M^{\text{phy}}_{[1,0]_F[1,-1]_F[1,1]_F} = \frac{1}{4} M^{(\xi_4\xi_5,\xi_4,\xi_5)}_{[1,0]_F[1,-1]_F[1,1]_F} \tag{2.68}$$

where $M^{\text{phy}}_{[1,0]_F[1,-1]_F[1,1]_F}$ is the physical matrix elements with the same isospin quantum numbers but without tastes. This argument holds as long as the product of three taste gamma matrices is the identity. Note that the same 1/4 factor is also necessary to normalize the two-point correlators in (2.57), so in practice, this normalization cancels out when we derive matrix elements from ratios of three-points to two-points functions.

We can also show with Wigner-Eckart theorem that as long as the taste is conserved, matrix elements with different tastes will all give the same continuum results in (2.68). First, we define the canonical matrix element $M^{(I)}$

$$M^{(I)} \equiv M^{(I,I,I)}_{[1,0]_F[1,-1]_F[1,1]_F} = \left\langle [1,0]_F[I] \middle| \overline{U}D \middle| [1,1]_F[I] \right\rangle \tag{2.69}$$

By the same argument above, we assume the canonical matrix element takes on the physical value if we normalize it by the 1/4 factor. We will then show that through two applications of the Wigner-Eckart theorem in both isospin and taste spaces, we can rotate matrix elements with any tastes to the canonical matrix element with normalization factors of ones. So they would all be equal to the physical matrix element once we normalize them by the 1/4 factors.

We will use $M^{(\xi_4\xi_5,\xi_4,\xi_5)}_{[1,0]_F[1,-1]_F[1,1]_F}$ as an example here, but it works equally well for all other tastes. It is impossible to apply the Wigner-Eckart in the taste space to rotate it to the canonical matrix element - the adjoint and trivial tastes do not mix under taste transformations. We can, however, perform rotations in both the isospin and taste quantum numbers to reach the trivial-taste states. We first matrix elements using Table 2.2 to write it as

$$
\begin{aligned}
M^{(\xi_4\xi_5,\xi_4,\xi_5)}_{[1,0]_F[1,-1]_F[1,1]_F} &\equiv \left\langle [1,0]_F[\xi_4\xi_5] \middle| \overline{U}\xi_4 D \middle| [1,1]_F[\xi_5] \right\rangle \\
&= \frac{1}{\sqrt{2}}\Big(\big\langle [1,0]_F[1,1]_S[0,0]_T \big| + \big\langle [1,0]_F[1,-1]_S[0,0]_T \big| \Big) \times \\
&\qquad\qquad \Big(2\mathcal{T}^{[1,0]_S[0,0]_T}_{[1,-1]_F} \Big) \times \\
&\quad \frac{1}{\sqrt{2}}\Big(\big| [1,1]_F[1,1]_S[0,0]_T \big\rangle - \big| [1,1]_F[1,-1]_S[0,0]_T \big\rangle \Big)
\end{aligned}
\tag{2.70}
$$

where $\mathcal{T}$ is the tensor operator that follows the normalization condition in Table I of [85]. States and operators are now labeled by their $[j,m]$ quantum number of the three SU(2) subgroups $\mathrm{SU}(2)_F \times \mathrm{SU}(2)_S \times \mathrm{SU}(2)_T \subset \mathrm{SU}(2)_F \times \mathrm{SU}(4) \supset \mathrm{SU}(8)$ identified by the subscripts. The irrep labels that distinguish between the adjoint and trivial tastes are unnecessary and omitted here – only $[0,0]_S[0,0]_T$ tastes can belong to the trivial irrep while other tastes must belong to the adjoint irrep. The factor of 2 normalizes the current operator to the tensor operator $\mathcal{T}$ so the Wigner-Eckart theorem can be applied, and the factors of $1/\sqrt{2}$ normalize the states to unit norms. We can simplify the expression by applying the SU(2) Wigner-Eckart theorem to get

$$
M^{(\xi_4\xi_5,\xi_4,\xi_5)}_{[1,0]_F[1,-1]_F[1,1]_F} = \left\langle [1,0]_F[1,1]_S[0,0]_T \middle| 2\mathcal{T}^{[1,0]_S[0,0]_T}_{[1,-1]_F} \middle| [1,1]_F[1,1]_S[0,0]_T \right\rangle \tag{2.71}
$$

This matrix element can be rotated to $M^{(I)}$ by applying the SU(4) Wigner-Eckart theorem in the flavor-taste space. What this means is that we can imagine embedding the product $\mathrm{SU}(2)_F \times \mathrm{SU}(2)_S$ from our group decomposition into a $\mathrm{SU}(4)_{FS}$ group that will simultaneously rotate flavor and taste quantum numbers. In other words, we can decompose the SU(8) symmetry group as

$$
\mathrm{SU}(8) \supset \mathrm{SU}(4)_{FS} \times \mathrm{SU}(2)_T \supset \mathrm{SU}(2)_F \times \mathrm{SU}(2)_S \times \mathrm{SU}(2)_T \tag{2.72}
$$

By doing so, we can transform a state with the adjoint taste to the taste-singlet one and reduce the problem to a rotation in SU(4) instead of SU(8). We can see from (2.71) that the states and operator transform in the adjoint irrep of $\mathrm{SU}(4)_{FS}$. To transform the matrix element to the taste-singlet one, we apply the Wigner-Eckart theorem using Table A4.6. of [85][3] to get

$$M^{(\xi_4\xi_5,\xi_4,\xi_5)}_{[1,0]_F[1,-1]_F[1,1]_F} = M^{(I)} \tag{2.73}$$

In general, we can rotate the matrix elements of arbitrary tastes to the singlet-taste one, thereby showing that they all give rise to physical matrix elements in the continuum limit. In practice, all we have to do is to write down a matrix element that "cancel out" all the taste gamma matrices to obtain the desired physical observable.

2.3.4 Staggered baryon masses and matrix elements with $SU(2)_F$ quantum numbers

Baryons are more complicated than mesons as there are simply more tastes or irreps available. There is not a simple set of rules, like the gamma matrix arithmetic for mesonic observables, to write down correlators that conserves the quantum numbers. In this section, we will focus only on the 20_S and 20_M irrep of staggered baryons because those are the ones that we use in Chapter 4 to deduce nucleon masses and charges. The same principle can be applied to the $\bar{4}$ irrep.

A baryon state will be denoted by its $\mathrm{SU}(2)_F$ flavor and SU(4) taste quantum numbers

$$\left|[j^F, m^F]_F [j^S, m^S]_S [j^T, m^T]_T\right\rangle \tag{2.74}$$

---

[3] There are typos in the table that needs to be considered.

where for baryons, all j's and m's are denoted with the spin notations. Note that it is in general ambiguous to denote the taste of a baryon only by their $\mathrm{SU}(2)_S$ and $\mathrm{SU}(2)_T$ quantum numbers – both 20_S and 20_M have states with $j^S = j^T = 1/2$ according to Table 2.1. For any other j^S and j^T, however, it is clear which irrep it belongs to. We will always be explicit which irrep the state belongs to when we have $j^S = j^T = 1/2$, then the notation should be unique.

For rooted, staggered fermions, the physical baryon masses can be obtained from the masses of single-taste baryons defined in Table 2.3 [82]. This does not preclude other states from having physical masses. Using flavor-taste rotations, there are in fact many states that all have the correct masses. Suppose we are interested in finding the mass of an isospin-1/2 baryon. We denote the highest-weight, single-taste baryon as

$$\left|\left[\frac{1}{2},\frac{1}{2}\right]_F;111_T\right\rangle \equiv \left|\left[\frac{1}{2},\frac{1}{2}\right]_F\left[\frac{3}{2},\frac{3}{2}\right]_S\left[\frac{3}{2},\frac{3}{2}\right]_T\right\rangle \tag{2.75}$$

We can show that states in

$$168_M \to \left(\frac{3}{2},20_M\right)\oplus\left(\frac{1}{2},20_S\right)\oplus\left(\frac{1}{2},\bar{4}\right)\oplus\left(\frac{1}{2},20_M\right) \tag{2.76}$$

where flavor and taste irreps are labeled in the parentheses, and 168_M is a baryon irrep of the SU(8) flavor-taste symmetry group that will be used in our nucleon simulations. Baryons within the 168_M are degenerated and have physical masses [82] because single-taste baryons are members of the irrep. It is interesting to note that that baryons with "wrong" isospin quantum numbers could still have the physical masses, considering that the isospin symmetry is only a subgroup of the full symmetry group SU(8). In our calculations later, we will find out that nucleons with isospins 3/2 are the most convenient to simulate. To distinguish them from the physical nucleons, we will oftentimes refer to them as nucleon-like states.

It is natural to extend the statements to say that those matrix elements consisting of single-taste baryons and single-taste quark bilinears are physical. However, single-taste quark bilinears are linear combinations of different operator tastes defined in Table 2.2, and it is much easier to work with current operators with are irreps of the lattice symmetry group. So for non-isospin-singlet operators, the physical matrix elements can be obtained with single-taste baryons and current operators with tastes I, ξ_4, $\xi_1\xi_2$ or $\xi_3\xi_5$, which we will sometimes be referred to as taste-diagonal operators. Again, we have to use the taste-singlet operator for isospin-singlet operators to obtain the correct disconnected diagram contributions. But for non-isospin-singlet cases, we are free to use any one of the four tastes given that we have normalized the current operators according to the discussion at the end of Section 2.3.1. This means that, for example,

$$\begin{aligned} M_{\text{phy}} =& \left|\left\langle \left[\frac{1}{2},\frac{1}{2}\right]_F ; 111_T \right| \frac{1}{\sqrt{2}}\big(\overline{U}U - \overline{D}D\big) \left| \left[\frac{1}{2},\frac{1}{2}\right]_F ; 111_T \right\rangle\right| = \\ & \left|\left\langle \left[\frac{1}{2},\frac{1}{2}\right]_F ; 111_T \right| \frac{1}{\sqrt{2}}\big(\overline{U}\xi_4 U - \overline{D}\xi_4 D\big) \left| \left[\frac{1}{2},\frac{1}{2}\right]_F ; 111_T \right\rangle\right| = \\ & \left|\left\langle \left[\frac{1}{2},\frac{1}{2}\right]_F ; 111_T \right| \frac{1}{\sqrt{2}}\big(\overline{U}\xi_1\xi_2 U - \overline{D}\xi_1\xi_2 D\big) \left| \left[\frac{1}{2},\frac{1}{2}\right]_F ; 111_T \right\rangle\right| = \\ & \left|\left\langle \left[\frac{1}{2},\frac{1}{2}\right]_F ; 111_T \right| \frac{1}{\sqrt{2}}\big(\overline{U}\xi_3\xi_5 U - \overline{D}\xi_3\xi_5 D\big) \left| \left[\frac{1}{2},\frac{1}{2}\right]_F ; 111_T \right\rangle\right| \end{aligned} \tag{2.77}$$

where M_{phy} is the physical matrix element without taste quantum numbers. We have taken absolute values of the matrix elements because of the potential ± 1 and $\pm i$ factors from the gamma matrices. These relations can also be proven by applying the Wigner-Eckart theorem using Table A4.2 of [85].

The extend SU(8) flavor-taste symmetry allows us to relate the matrix elements of baryons with 20_M to those with 20_S tastes just like how it works for meson matrix elements. Let's consider the matrix element

$$M_{20_M} \equiv \left\langle \left[\frac{3}{2},\frac{3}{2}\right]_F \left[\frac{3}{2},\frac{3}{2}\right]_S \left[\frac{1}{2},\frac{1}{2}\right]_T \middle| \frac{1}{\sqrt{2}}\left(\overline{U}\xi_3\xi_5 U - \overline{D}\xi_3\xi_5 D\right) \times \middle| \left[\frac{3}{2},\frac{3}{2}\right]_F \left[\frac{3}{2},\frac{3}{2}\right]_S \left[\frac{1}{2},\frac{1}{2}\right]_T \right\rangle \tag{2.78}$$

This shows up in the calculation of the nucleon axial charge in Chapter 4. Notice that the baryons transform in the isospin-3/2, 20_M representation. The goal is to relate M_{20_M} the one of the physical matrix elements defined in (2.77) with isospins 1/2. Note that the current is already taste diagonal in this example, so we know the physical matrix elements is equal to

$$M_{\text{phy}} = \left\langle \left[\frac{1}{2},\frac{1}{2}\right]_F ; 111_T \middle| \frac{1}{\sqrt{2}}\left(\overline{U}\xi_3\xi_5 U - \overline{D}\xi_3\xi_5 D\right) \middle| \left[\frac{1}{2},\frac{1}{2}\right]_F ; 111_T \right\rangle \tag{2.79}$$

The current operator transforms as the tensor operator

$$\frac{1}{\sqrt{2}}\left(\overline{U}\xi_3\xi_5 U - \overline{D}\xi_3\xi_5 D\right) = 2\mathcal{T}^{[1,0]_S[1,0]_T}_{[1,0]_F} \tag{2.80}$$

where the factor of 2 comes from the normalization condition, and various parentheses denote the quantum numbers of SU(2) subgroups. We apply the Wigner-Eckart theorem on the $\mathrm{SU}(4)_{FT} \supset \mathrm{SU}(2)_F \times \mathrm{SU}(2)_T$ subgroup with CG coefficients defined in Table A4.5. of [85] to obtain

$$M_{\text{phy}} = M_{20_M} \tag{2.81}$$

which relies on the symmetry property of these particular CG coefficients

$$\begin{aligned}\Big\langle [20_M]\,[j_1^F, j_1^T];\,[15]\,[j_2^F, j_2^T]\ \Big\|\ [20_M]\,[J-1, J]\Big\rangle_\rho &= \\ \Big\langle [20_M]\,[j_1^T, j_1^F];\,[15]\,[j_2^T, j_2^F]\ \Big\|\ [20_M]\,[J, J-1]\Big\rangle_\rho &\end{aligned} \tag{2.82}$$

In other words, we can use isospin-3/2 baryons in (2.78) to simulate a matrix element in (2.79) with isospin-1/2 baryons, which is what we will be doing in the following chapters.

Alternatively, we observe that when we decompose SU(8) to the products of three SU(2) subgroups, the decomposition is completely symmetrical, meaning that there is a symmetry of exchanging subscript labels of the irreps. We can simply exchange the F and T labels on (2.78) to obtain (2.79).

It should be emphasized that when we perform simulations with the rooted, staggered quark action, we are not simulating QCD because of the four extra tastes for each quark species. In order to extract physical observables, we have to think carefully about which observables are identical in those two theories. This is achieved in this work by realizing that observables consist of a single taste in staggered QCD must coincide with the one in the physical QCD. One can then apply symmetry transformations presented in this chapter to relate other staggered observables to the single-taste ones. In a way, this theoretical complexity becomes the strength of staggered simulations, as for a given QCD observable we want to calculate, there are many equivalent staggered observables that we can simulate which all give rise to the same continuum results. We have so far focused only on the calculations of masses and matrix elements of single-particle mesons and baryons, but the same underlying principles can be derived for other observables such as the spectrum of multi-particle states, four-point functions, etc.

Chapter 3

Spectrum of staggered baryons

3.1 Symmetries of the staggered action

This section will give an overview on how to construct staggered baryon interpolators and states based on the symmetry group of the staggered lattice action. The free staggered action for one quark flavor is given by

$$S_F = \overline{\chi}(\not{D} + m)\chi = \frac{1}{2}\sum_n \sum_{\mu=1}^{4} \eta_\mu(n)\overline{\chi}(n)\Big(\chi(n+\hat{\mu}) - \chi(n-\hat{\mu})\Big) + m\sum_n \overline{\chi}(n)\chi(n) \tag{3.1}$$

where $n \equiv (n_1, n_2, n_3, n_4)$; unless specified otherwise, we omit the color indices in this chapter as they play no roles in the following discussions.

There are four convention-dependent phase factors, η_μ, $\xi_\mu(n)$, $S_{R_{\mu\nu}}(n)$, and $\epsilon(n)$, that act as "gamma matrices" for one-component spinor fields. In the convention we are working with, they are defined as

$$\begin{aligned} \eta_\mu(n) &\equiv (-1)^{\sum_{\nu<\mu} n_\nu} \\ \xi_\mu(n) &\equiv (-1)^{\sum_{\nu>\mu} n_\nu} \\ \epsilon(n) &\equiv (-1)^{n_1+n_2+n_3+n_4} \\ S_{R_{\mu\nu}}(n) &\equiv \frac{1}{2}\big(1 \pm \eta_\mu(n)\eta_\nu(n) \mp \xi_\mu(n)\xi_\nu(n) + \eta_\mu(n)\eta_\nu(n)\xi_\mu(n)\xi_\nu(n)\big),\ \mu \lessgtr \nu \end{aligned} \tag{3.2}$$

which are the same as those in [78, 79, 81]. The symmetries of the action that are relevant to classifying baryon operators are [81]:

- shift S_μ: $\chi(n) \to \xi_\mu(n)\chi(n+\hat{\mu})$
- rotation $R_{\mu\nu}$: $\chi(n) \to S_{R_{\mu\nu}}(R^{-1}_{\mu\nu}n)\chi(R^{-1}_{\mu\nu}n)$
- spatial inversion I_s: $\chi(n) \to \eta_4(n)\chi(I_s n),\ I_s n = (-n_1, -n_2, -n_3, n_4)$

The antiquark fields $\overline{\chi}(n)$'s transform identically as the quark fields $\chi(n)$'s for these operations, so we restrict our discussions to $\chi(n)$ only. We note that each symmetry operation defined above contains a phase factor that depends on n. Intuitively, this is because the staggering procedures mix the spacetime symmetries with internal taste symmetries, so any spacetime symmetry operations on the staggered fields $\chi(n)$ will inadvertently transform both the locations of and tastes, which show up as n-dependent phase factors.

On the lattice, the taste and spacetime symmetries are deeply intertwined and cannot be separated exactly, as the spinor components of naive quarks are distributed across different lattice sites under the staggering procedure. One common strategy to *approximately* isolate each fermion taste is by blocking $\chi(x)$ within the hypercube to select out the appropriate spin and taste (see the section on staggered fermions in [49] for a detailed exposition. See also the appendices of [83] for examples), thereby effectively moding the lattice dimensions by two in each direction. To achieve this, we separate the shift symmetries into two sets [78, 81]

- translation $T_\mu \equiv S_\mu^2$: $\chi(n) \to \chi(n+2\hat{\mu})$
- taste transformation $\Xi_\mu \equiv S_\mu T_\mu^{-1/2}$

Without loss of generality, assume we always have even lattice sites in each direction. Then the translation defined this way is free of taste transformation, and states transforming in the irrep will have definite energy and momentum in the continuum limit; on the other hands, $[\Xi_\mu, T_\mu] = 0$ and $[\Xi_\mu, \Xi_\nu] = 2\delta_{\mu\nu}$, and Ξ_μ can be interpreted as the subgroup of the continuum taste transformation on the lattice. We only consider the action of Ξ_μ on eigenstates of T_μ, so the action of $T_\mu^{-1/2}$ is well defined.

The eigenstates of I_s do not have well defined parities since I_s contains taste transformations, as evidenced by the presence of $\eta_\mu(n)$ phases. The parity operators can be defined via [78, 81]

- parity $P \equiv I_s \Xi_4$

which commute with both Ξ_μ and $R_{\mu\nu}$. States with definite P quantum numbers will also have the same continuum parities. Now we can understand why staggered fermions stagger. We see from the definition of P that it contains the temporal taste transformation Ξ_4 which cancels out the taste transformation in I_s so that P is taste invariant. This means that if we are to construct states with definite parity, we have to use interpolators that span multiple time slices on the lattice which could be problematic on the lattice; see [52] for a discussion. Instead, states with both positive and negative parities will show up when interpolators are restricted to a single time slice, which gives rise to the characteristic oscillation of staggered correlators (see figures in [2, 3] for some correlator examples).

3.2 Staggered baryons at zero momenta on the lattice

Staggered baryons at zero momenta transform as irreps of the geometric rest-frame group (GRF) [81]

$$\mathrm{GRF} \equiv \left\{ \Xi_\mu, R_{\mu\nu}, P \right\} \tag{3.3}$$

Note that it is equivalent to replace the parity operator in the group definition as both I_s and P are in GRF.

As usual, we first find the maximal set of commuting operators within GRF to classify baryons, which can be chosen as R_{12}, Ξ_4, $\Xi_1\Xi_2$, and P. Following the same notations as in [81], the lattice baryons are labeled by kets

$$\left| m r \sigma; \sigma_t \right\rangle \tag{3.4}$$

where m is the mass, r denotes both Ξ_4 and R_{12} eigenvalues, $\sigma = \pm$ is the parity, and σ_t is the eigenvalue of Ξ_4.

Baryon interpolators are constructed from quark trilinears that are irreps of the symmetry group on a single time slice, or geometric time slice group (GTS)

$$\mathrm{GRF} \supset \mathrm{GTS} \equiv \{\Xi_i, R_{ij}, I_s\} \tag{3.5}$$

Note that GRF $=$ GTS $\times\, \mathbb{Z}_2(P)$, where $\mathbb{Z}_2(P)$ is the $\mathbb{Z}_2$ group generated by the parity operators, so σ, the parity quantum number, is the only missing one.

Let $O(t)$ be a baryon interpolator transform in an irrep of GTS at time slice t. The two-point correlator has spectral decomposition

$$\begin{aligned}
\langle O(t)\overline{O}(0)\rangle &= \langle\Omega|O(t)\overline{O}(0)|\Omega\rangle \\
&= \sum_n \langle\Omega|O(t)|m_n r\sigma_n;\sigma_{t,n}\rangle\langle m_n r\sigma_n;\sigma_{t,n}|\overline{O}(0)|\Omega\rangle \\
&= \sum_n \langle\Omega|S_4^t O(t) S_4^{-t} S_4^t|m_n r\sigma_n;\sigma_{t,n}\rangle\langle m_n r\sigma_n;\sigma_{t,n}|\overline{O}(0)|\Omega\rangle \\
&= \sum_n (\sigma_{t,n})^t e^{-m_n t}\langle\Omega|O(0)|m_n r\sigma_n;\sigma_{t,n}\rangle\langle m_n r\sigma_n;\sigma_{t,n}|\overline{O}(0)|\Omega\rangle
\end{aligned} \tag{3.6}$$

In the first line we assume the lattice has an infinite time extent L_T so thermal terms proportional to exponentials in L_T are ignored; in line 2, note that we are summing over eigenvalues m, σ, and σ_t, but not r since irreps of GTS always have definite r quantum numbers; in going from the third to the fourth line, we use the definition $S_4 = \Xi_4 T_4^{1/2}$ (T_4 is the transfer matrix) to write it as the product of Ξ_4 and T_4 eigenvalues. Let $\sigma_s = \pm 1$ be the eigenvalues of $O(t)$ under I_s, we can then rewrite (3.6) as

$$\langle O(t)\overline{O}(0)\rangle = \sum_n (\sigma_s\sigma_n)^t e^{-m_n t}\langle\Omega|O(0)|m_n r\sigma_n;\sigma_{t,n}\rangle\langle m_n r\sigma_n;\sigma_{t,n}|\overline{O}(0)|\Omega\rangle \tag{3.7}$$

In other words, if $\sigma_s = 1$, the positive parity states will have prefactors $(\sigma_s\sigma_n)^t = 1$ while the negative parity states will have $(\sigma_s\sigma_n)^t = (-1)^t$, which shows up as the staggering pattern in correlation functions.

We are now ready to construct operators from $\chi(n)$ fields that we can actually put into a numerical simulation. The irreps of GTS can be classified into baryonic (unfaithful) and fermionic (faithful) irreps. Operators constructed from products of even/odd numbers of $\chi(n)$ is always baryonic/fermionic. In this work, we will focus only on quark trilinears so we will only work with fermionic irreps – see [79] for explicit constructions of quark bilinears.

Fortunately, there are only three fermionic irreps – 8, 8′, and 16 where the number denotes the dimensions of an irrep. The fundamental quark fields at zero momentum transform in the 8 irrep

$$\sum_{\vec{n}\in\text{even}} \begin{pmatrix} \chi_0(\vec{n}) \\ \chi_1(\vec{n}) \\ \vdots \\ \chi_7(\vec{n}) \end{pmatrix} \tag{3.8}$$

We assume all fields reside on the time slice $n_4 = 0$ and omit n_4 in $\vec{n} = (n_1, n_2, n_3)$; $\vec{n} \in$ even is summing all lattice sites that are even in all three coordinates. $\chi_A(\vec{n}) \equiv \chi(\vec{n} + \vec{D}_A)$ where $\vec{D}_A$ is one of the eight corners of a spatial cube, with its coordinate given by the binary representation of i, namely,

$$\begin{aligned} \vec{D}_0 &= (0,0,0) = (n_x, n_y, n_z) \\ \vec{D}_1 &= (1,0,0) \\ \vec{D}_2 &= (0,1,0) \\ &\vdots \\ \vec{D}_6 &= (1,1,0) \\ \vec{D}_7 &= (1,1,1) \end{aligned} \tag{3.9}$$

When we define staggered baryon operators later, we will oftentimes denote a corner by its scalar subscript $A = 0, \cdots, 7$.

One can check easily that (3.8) transforms in the zero momentum irrep of GTS by explicitly applying group elements to the operators. The sum here is only on the even sites as the translational symmetry shift the field by two lattice units.

We take the tensor products of three fundamental 8 irreps to construct baryonic irreps

$$8 \otimes 8 \otimes 8 = 5 \cdot 8 \oplus 2 \cdot 8' \oplus 4 \cdot 16 \tag{3.10}$$

The multiplicities of all baryonic irreps are larger than one, meaning there is more than one way to arrange three quark fields on the cube to construct the same irrep. In staggered baryons literature, different constructions of the same irrep are referred to as "classes" [81, 82], and we will follow the nomenclature here. All operators in specific irrep will excite the same spectrum of states regardless of the operator classes.

Class 1 of the 8 irrep is the simplest to understand, which has the same construction as (3.8) besides replacing one quark field with three quark fields on the same site. However, while being the simplest to illustrate, its spectrum is one of the most complicated out of all three irreps. In Section 3.3, we will show that the isospin-3/2, 8 irrep operator creates three nucleon-like and two Δ-like ground states in the positive parity channels, while its isospin-1/2 counterpart creates five nucleon-like and one Δ-like ground states. Again, we refer to them as nucleon-like and Δ-like states instead of nucleons and Δ's to emphasize that they have the same continuum masses as physical nucleons and Δ's, but they could have the wrong isospin and taste quantum numbers.

Simulations with 8 irreps have proven to be difficult from our experiences. On the lattice, these nucleon-like states are nearly degenerate, with their mass gaps dictated by the size of taste-breaking effects in the lattice action. Disentangling different states thus requires precise determinations of the correlation functions that are difficult to attain. Instead, we focus on the isospin-3/2, 16 irrep operators in this thesis that has the simplest spectrum of all irreps with one nucleon-like and three Δ-like ground states.

To construct such operators, we introduce the symmetric shift operator [81, 82]

$$D_i \chi_A(\vec{n}) \equiv \frac{1}{2}\big(\chi_A(\vec{n}+\hat{i}) + \chi_A(\vec{n}-\hat{i})\big) \tag{3.11}$$

where $i = 1, 2, 3$. Then, as an example, a class-2, 16 irrep operator can be constructed as

$$\begin{aligned} O^{16+,0;\mathrm{cls2}} \equiv & \frac{1}{\sqrt{6}} \sum_{\vec{n}\in\mathrm{even}} \sum_{a,b,c} \epsilon_{abc} \Big\{ \chi^a(\vec{n}) D_1\big(\chi^b(\vec{n})\chi^c(\vec{n})\big) + \\ & \chi^a(\vec{n}) D_2\big(\chi^b(\vec{n})\chi^c(\vec{n})\big) - 2\chi^a(\vec{n}) D_3\big(\chi^b(\vec{n})\chi^c(\vec{n})\big) \Big\} \end{aligned} \tag{3.12a}$$

$$O^{16-,0;\mathrm{cls2}} \equiv \frac{1}{\sqrt{2}} \sum_{\vec{n}\in\mathrm{even}} \sum_{a,b,c} \epsilon_{abc} \Big\{ \chi^a(\vec{n}) D_1\big(\chi^b(\vec{n})\chi^c(\vec{n})\big) - \chi^a(\vec{n}) D_2\big(\chi^b(\vec{n})\chi^c(\vec{n})\big) \Big\} \tag{3.12b}$$

where the color indices a, b, and c are antisymmetrized. The 16 irrep is separated into two sets, 16+ and 16−, where the plus and minus signs denote the eigenvalues of $O^{16\pm,0;\mathrm{cls2}}$ under R_{12} rotations. Each set contains eight irrep components and each component resides on one of the eight corners of a spatial cube given by the sum of quark positions modulo two. In this example, we show the zeroth-corner operators denoted by the subscripts 0. We can obtain other components, $O^{16\pm,A;\mathrm{cls2}}$, $A = 0, \cdots, 7$, by applying the appropriate spatial shift operators. See [81] for definitions of other operators.

It is a straightforward exercise to add isospin quantum numbers to baryon operators. The simplest ones, also the ones that we will use in practice, are the isospin-3/2 operators with the highest weights. In this case, no extra work is needed – all we have to do is to replace χ's in (3.12) by the up-quark fields. See [82], which builds upon the results of [81], for the complete set of operators with isospin quantum numbers.

It is convenient to separate the 16 irrep components into 16± so they each occupy eight corners of the cube. This also has important group-theoretical consequences in the continuum limit which will be discussed in Section 4.2.4. The bottom line is that ratios of matrix elements constructed from 16± interpolators are given by the ratios of the appropriate CG coefficients that we will derive. We use this fact in Section 4.2.4 to perform consistent checks on our simulation data.

Non-local operators defined in (3.12) are not gauge invariant as the gauge links are not included. We can either i) include gauge links to make the operators gauge invariant, or ii) perform simulations on gauge-fixed configurations. Note that gauge fixings are completely optional in lattice simulations to obtain finite results unlike in continuum calculations. It is costly in our simulations to include gauge links for both source and sink interpolators, as doing so would require $8^2 = 64$ propagator solves to construct one set of correlators if we are to include all correlators that are equal on the ensemble average, compared to eight propagator solves for sources emanating from eight corners of a cube if gauge links are ignored. Instead, we gauge fix all configurations to the Coulomb gauge [49]. We observe that simulations on gauge-fixed configurations have added benefits of being less noisy because we restrict path integrals to a specific gauge choice thereby reducing the observable variance. So in practice, we always calculate correlators with Coulomb-gauge-fixed configurations, and since the nucleon masses and matrix elements we try to compute are gauge invariant, this choice does not affect our final results.

3.3 Spectrum of staggered baryon operators with SU(2) quantum numbers

Now that we have constructed baryon irreps on the lattice, we want to now know their ground state spectra. Specifically, we will focus on operators with either isospin-1/2 or 3/2 quantum numbers. To answer this question, we have to start with the continuum symmetry group and work our ways down following the symmetry breaking pattern until we reach the

GTS group.

Nucleon-like (N-like) and Δ-like states are the lowest-lying baryons which the operators can excite. They reside in the continuum irreps [82]

$$
\begin{aligned}
&\mathrm{SU}(2)_S \times \mathrm{SU}(8)_{FT} \supset \mathrm{SU}(2)_S \times \mathrm{SU}(2)_F \times \mathrm{SU}(4)_T \\
N\text{-like} &= \left(\frac{1}{2}, 168_M\right) \rightarrow \left(\frac{1}{2}, \frac{3}{2}, 20_M\right) \oplus \left(\frac{1}{2}, \frac{1}{2}, 20_S\right) \oplus \left(\frac{1}{2}, \frac{1}{2}, \bar{4}\right) \oplus \left(\frac{1}{2}, \frac{1}{2}, 20_M\right) \quad \text{(3.13a)} \\
\Delta\text{-like} &= \left(\frac{3}{2}, 120_S\right) \rightarrow \left(\frac{3}{2}, \frac{3}{2}, 20_S\right) \oplus \left(\frac{3}{2}, \frac{1}{2}, 20_M\right) \quad \text{(3.13b)}
\end{aligned}
$$

We use a different group labeling scheme here than the one that appears in chapter 2: $\mathrm{SU}(2)_S$ is the spin group, $\mathrm{SU}(2)_F$ is the isospin symmetry group, and $\mathrm{SU}(4)_T$ is the taste group. In section 2.3.4, we have discussed the spectrum of staggered nucleons in the continuum, and proven in (2.76) that, because (3.13a) contains the physical single-taste nucleons which transform in the spin-1/2, isospin-3/2, 20_S irrep, all N-like states in that equation will be degenerate with the physical nucleon, despite potentially having the wrong isospin or taste quantum numbers. Similarly, we extend the same arguments to Δ-like states to state that all Δ-like states in (3.13b) are degenerate with the physical Δ baryons.

We further decompose the taste group into the product of SU(2) subgroups [2]

$$
\mathrm{SU}(4)_T \supset \mathrm{SU}(2)_{\mathbb{Q}_8} \times [(\mathrm{SU}(2)_{D_4} \times \mathbb{Z}_4)/\mathbb{Z}_2] \tag{3.14}
$$

Eventually, we will subdue $[(\mathrm{SU}(2)_{D_4} \times \mathbb{Z}_4)/\mathbb{Z}_2]$ to the finite $D_4 \subset$ GTS group, the dihedral group of order 8, on the lattice, hence the D_4 label on SU(2). Since D_4 is not a subgroup of SU(2), we need a $\mathbb{Z}_4$ phase factor to correct for this. For the fermionic (faithful) irrep we need here, $\mathbb{Z}_4 = \{\pm 1, \pm i\}$; the $\mathbb{Z}_2$ quotient factor ensures we are not overcounting group elements by identifying $(-1, -1) = (1, 1)$ and $(-1, 1) = (1, -1)$. This combination is referred to as the central product of $\mathrm{SU}(2)_{D_4}$ and $\mathbb{Z}_4$. The $\mathbb{Z}_N$ factors[1] are there to ensure the group subduction is correct, however, they have few physical consequences and we will ignore their labels. On the other hand, we have another SU(2) group factor labeled with $\mathbb{Q}_8$, which can be decomposed to the quaternion group $\mathbb{Q}_8 \subset$ GTS [2]. Note that the SU(2) labeling scheme here is different from the one used in chapter 2.

Further decomposing the taste irreps in (3.13) according to (3.14) can be done by using results in the second column of Table 2.1. The relevant entries read

$$\begin{aligned}
\mathrm{SU}(4)_T \supset \mathrm{SU}(2)_{\mathbb{Q}_8} &\times [(\mathrm{SU}(2)_{D_4} \times \mathbb{Z}_4)/\mathbb{Z}_2] \\
20_S &\to \left(\frac{3}{2}, \frac{3}{2}\right) \oplus \left(\frac{1}{2}, \frac{1}{2}\right) \\
20_M &\to \left(\frac{3}{2}, \frac{1}{2}\right) \oplus \left(\frac{1}{2}, \frac{3}{2}\right) \\
\bar{4} &\to \left(\frac{1}{2}, \frac{1}{2}\right)
\end{aligned} \tag{3.15}$$

where the first number in each parenthesis denotes the quantum number of $\mathrm{SU}(2)_{\mathbb{Q}_8}$ and the second one denotes the quantum number of $\mathrm{SU}(2)_{D_4}$. On the lattice, D_4 is generated by operators Ξ_{123} and I_s. The irreps of $\mathrm{SU}(2)_{\mathbb{Q}_8}$ appearing in (3.15) can be subduced to D_4 irreps as

$$\begin{aligned}
[(\mathrm{SU}(2)_{D_4} \times \mathbb{Z}_4)/\mathbb{Z}_2] &\supset D_4 \\
\frac{1}{2} &\to B \\
\frac{3}{2} &\to B \oplus B
\end{aligned} \tag{3.16}$$

where B is the only two-dimensional, fermionic (faithful) irrep of D_4. We adopt the same irrep label as [2]. In the basis where the irreps have definite I_s eigenvalues, the two states transforming in the B irrep will have ±1 eigenvalues. We will show this explicitly later when

---

[1] We have neglected some other $\mathbb{Z}_N$ factors in the decomposition as they are not important to our discussions.

we deduce the continuum quantum numbers of nucleon-like states excited by GTS operators.

After this decomposition step, the remaining subgroup becomes

$$\mathrm{SU}(2)_{\mathbb{Q}_8} \times \mathrm{SU}(2)_S \times [(\mathrm{SU}(2)_{D_4} \times \mathbb{Z}_4)/\mathbb{Z}_2] \tag{3.17}$$

We have ignored the flavor $\mathrm{SU}(2)_F$ group as it is not broken by the lattice. The last decomposition step before matching the irreps of GTS is

$$\mathrm{SU}(2)_{\mathbb{Q}_8} \times \mathrm{SU}(2)_S \supset \mathrm{SU}(2)_{\mathrm{SW}_3} \tag{3.18}$$

where $\mathrm{SU}(2)_{\mathrm{SW}_3}$ is the diagonal subgroup. Subducing tensor products of SU(2) irreps is a simple angular momentum addition problem, so we obtain

$$\begin{gathered}\mathrm{SU}(2)_{\mathbb{Q}_8} \times \mathrm{SU}(2)_S \supset \mathrm{SU}(2)_{\mathrm{SW}_3} \\ \left(\frac{1}{2}, \frac{1}{2}\right) \to 1 \oplus 0 \\ \left(\frac{3}{2}, \frac{1}{2}\right) \to 2 \oplus 1 \\ \left(\frac{1}{2}, \frac{3}{2}\right) \to 2 \oplus 1 \\ \left(\frac{3}{2}, \frac{3}{2}\right) \to 3 \oplus 2 \oplus 1 \oplus 0\end{gathered} \tag{3.19}$$

Furthermore, for SU(2) groups, not only do we know about how the tensor products decompose to irreps of the diagonal subgroup, but we also know how to write down the exact linear combinations of those tensor-product states with CG coefficients that transform in the irreps on the right-hand side. This is what enables us to figure out the continuum quantum numbers of baryons excited by our lattice operators that we will discuss in the next section. But for now, we don't need that information to deduce the spectrum.

To see why (3.19) is useful for decomposing the continuum group irreps, let's revisit the

GTS irreps and decompose them further to its discrete rotation subgroup

$$\begin{aligned} \mathrm{GTS} \supset \mathrm{W}_3 \equiv \{R_{ij}, I_s\} &= \mathrm{SW}_3 \times \mathbb{Z}_2 \\ 8 \to \boxed{A_1^+} &\oplus A_1^- \oplus T_1^+ \oplus T_1^- \\ 8' \to \boxed{A_2^+} &\oplus A_2^- \oplus T_2^+ \oplus T_2^- \\ 16 \to \boxed{E^+} &\oplus E^- \oplus T_1^+ \oplus T_1^- \oplus T_2^+ \oplus T_2^- \end{aligned} \tag{3.20}$$

W_3 is the discrete symmetry group of a cubic lattice as defined in [78], and irreps on the right are defined in [81].[2] Noticeably, A_1^+ is the trivial irrep. The superscripts denote the eigenvalues of I_s.

In each line, we have boxed an irrep of W_3 that uniquely appears in that specific irrep decomposition, which allows us to decompose the irreps of $\mathrm{SU}(3)_{\mathrm{SW}_3}$ to SW_3, and hence, GTS. Mapping continuum rotations to the discrete ones is a common task for all lattice formulation, and has been worked out before (for example, see [89, 90]). Furthermore, we will add back the D_4 decomposition results in (3.15) and (3.16). The relevant decompositions

---

[2] We switch the irrep labels of F's to T's, which are more commonly used in lattice literatures.

read

$$
\begin{aligned}
\mathrm{SU}(2)_{\mathrm{SW}_3} \times [(\mathrm{SU}(2)_{D_4} \times \mathbb{Z}_4)/\mathbb{Z}_2] \supset \mathrm{W}_3 & \\
\left(3, \frac{1}{2}\right) &\to A_2^+ \oplus A_2^- \oplus T_1^+ \oplus T_1^- \oplus T_2^+ \oplus T_2 \\
\left(3, \frac{3}{2}\right) &\to 2 \cdot \left(A_2^+ \oplus A_2^- \oplus T_1^+ \oplus T_1^- \oplus T_2^+ \oplus T_2\right) \\
\left(2, \frac{1}{2}\right) &\to E^+ \oplus E^- \oplus T_2^+ \oplus T_2^- \\
\left(2, \frac{3}{2}\right) &\to 2 \cdot \left(E^+ \oplus E^- \oplus T_2^+ \oplus T_2^-\right) \qquad (3.21) \\
\left(1, \frac{1}{2}\right) &\to T_1^+ \oplus T_1^- \\
\left(1, \frac{3}{2}\right) &\to 2 \cdot \left(T_1^+ \oplus T_1^-\right) \\
\left(0, \frac{1}{2}\right) &\to A_1^+ \oplus A_1^- \\
\left(0, \frac{3}{2}\right) &\to 2 \cdot \left(A_1^+ \oplus A_1^-\right)
\end{aligned}
$$

The pattern here is clear: 1/2 irrep of $\mathrm{SU}(2)_{D_4}$ will always subdue into lattice irreps with $\pm\ I_s$ eigenvalues, while 3/2 irrep will subdue into two identical copies of that same lattice irreps. By matching now the results of (3.21) and (3.19) to (3.20), we can easily work out the decomposition of the continuum irreps to 8, $8'$, and 16 irreps of GTS. The complete irrep decompositions starting from (3.13) now read

$$\mathrm{SU}(2)_F \times \mathrm{SU}(2)_S \times \mathrm{SU}(4)_T \supset$$

$$\mathrm{SU}(2)_F \times \mathrm{SU}(2)_S \times \mathrm{SU}(2)_{\mathbb{Q}_8} \times [(\mathrm{SU}(2)_{D_4} \times \mathbb{Z}_4)/\mathbb{Z}_2] \supset \mathrm{SU}(2)_F \times \mathrm{GTS}$$

N-like state:

$$\begin{aligned}
&\left(\frac{3}{2}, \frac{1}{2}, 20_M\right) \rightarrow \\
&\qquad \left(\frac{3}{2}, \frac{1}{2}, \frac{1}{2}, \frac{3}{2}\right) \oplus \left(\frac{3}{2}, \frac{1}{2}, \frac{3}{2}, \frac{1}{2}\right) \oplus \left(\frac{3}{2}, \frac{1}{2}, \frac{1}{2}, \frac{1}{2}\right) \rightarrow 3 \cdot \left(\frac{3}{2}, 8\right) \oplus \left(\frac{3}{2}, 16\right) \\
&\left(\frac{1}{2}, \frac{1}{2}, 20_S\right) \rightarrow \\
&\qquad \left(\frac{1}{2}, \frac{1}{2}, \frac{3}{2}, \frac{3}{2}\right) \oplus \left(\frac{1}{2}, \frac{1}{2}, \frac{1}{2}, \frac{1}{2}\right) \rightarrow 2 \cdot \left(\frac{1}{2}, 16\right) \oplus \left(\frac{1}{2}, 8\right) \\
&\left(\frac{1}{2}, \frac{1}{2}, \bar{4}\right) \rightarrow \\
&\qquad \left(\frac{1}{2}, \frac{1}{2}, \frac{1}{2}, \frac{1}{2}\right) \rightarrow \left(\frac{1}{2}, 8\right) \\
&\left(\frac{1}{2}, \frac{1}{2}, 20_M\right) \rightarrow \\
&\qquad \left(\frac{1}{2}, \frac{1}{2}, \frac{1}{2}, \frac{3}{2}\right) \oplus \left(\frac{1}{2}, \frac{1}{2}, \frac{3}{2}, \frac{1}{2}\right) \oplus \left(\frac{1}{2}, \frac{1}{2}, \frac{1}{2}, \frac{1}{2}\right) \rightarrow 2 \cdot \left(\frac{1}{2}, 8\right) \oplus \left(\frac{1}{2}, 16\right) \oplus \left(\frac{1}{2}, 8\right)
\end{aligned} \tag{3.22a}$$

Δ-like state:

$$\begin{aligned}
&\left(\frac{3}{2}, \frac{3}{2}, 20_S\right) \rightarrow \\
&\qquad \left(\frac{3}{2}, \frac{3}{2}, \frac{3}{2}, \frac{3}{2}\right) \oplus \left(\frac{3}{2}, \frac{3}{2}, \frac{1}{2}, \frac{1}{2}\right) \rightarrow 2 \cdot \left\{\left(\frac{3}{2}, 8\right) \oplus \left(\frac{3}{2}, 8'\right) \oplus \left(\frac{3}{2}, 16\right)\right\} \oplus \left(\frac{3}{2}, 16\right) \\
&\left(\frac{1}{2}, \frac{3}{2}, 20_M\right) \rightarrow \\
&\qquad \left(\frac{1}{2}, \frac{3}{2}, \frac{1}{2}, \frac{3}{2}\right) \oplus \left(\frac{1}{2}, \frac{3}{2}, \frac{3}{2}, \frac{1}{2}\right) \oplus \left(\frac{1}{2}, \frac{3}{2}, \frac{1}{2}, \frac{1}{2}\right) \rightarrow 4 \cdot \left(\frac{1}{2}, 16\right) \oplus \left(\frac{1}{2}, 8\right) \oplus \left(\frac{1}{2}, 8'\right)
\end{aligned} \tag{3.22b}$$

Table 3.1: Spectra of staggered baryon operators transforming as irreps of $\mathrm{SU}(2)_F \times$GTS.

$\mathrm{SU}(2)_F$ irrep	GTS irrep	# N-like states	# Δ-like states
$\frac{1}{2}$	8	5	1
$\frac{3}{2}$	8	3	2
$\frac{1}{2}$	$8'$	0	1
$\frac{3}{2}$	$8'$	0	2
$\frac{1}{2}$	16	3	4
$\frac{3}{2}$	16	1	3

We can work out the spectra of lattice operators based on the results of (3.22). For example, we can figure out the ground state spectrum of the isospin-3/2, 16 irrep by realizing that there is only one continuum irrep of the nucleon-like states which subduces to this lattice irrep, while there are three continuum irreps of the Δ-like states which subdues into it. This means that the operators transforming in this irrep can excite one nucleon-like and three Δ-like states. Lattice discretization destroys the full continuum symmetry group, so operators transforming as irreps of the lattice symmetry group will mix all continuum states that subduce to the same lattice irreps. The mass degeneracy of the continuum spectrum in (3.13) will be lifted on the lattice, with small mass gaps that depend on the lattice spacing, and can only be restored by taking the continuum limit.

In Table 3.1, we list all the staggered baryon operators that we consider in this work and their corresponding spectra. As promised, the isospin-3/2, 16 irrep only excites a single nucleon-like state. Note that the isospin-1/2, $8'$ irrep only excites one Δ-like state. If we replace light quarks in the baryons with strange quarks and impose a new "isospin" symmetry for two species of valence strange quarks, we can use this operator to excite a single omega baryon and study its properties [82, 91, 92]. The mass of the omega baryon is particularly useful in determining the lattice spacings with small systematic errors (well measured in experiments, small QED corrections compared to f_π, insensitive to light quark masses, and so on), and we are starting to see more lattice simulations based on the omega baryon mass scale-setting (for example, see [92, 93]) in the pursuit of higher precision.

3.4 Continuum quantum numbers of lattice baryons

It is sufficient to construct two-point correlators with staggered baryon operators defined in [81, 82] and use Table 3.1 to derive the masses of nucleons and Δ baryons. Going beyond spectrum calculations to matrix elements, we need to additionally know the continuum quantum number of nucleon-like and Δ-like states so that we can apply the generalized Wigner-Eckart theorem to relate the staggered QCD observables to QCD observables as discussed in section 2.3.4. A continuum state breaks into a linear combination of lattice states, or equivalently, a lattice state can be written as linear combinations of continuum states. The goal is then to find the exact coefficients of these linear combinations, or subduction coefficients as they are usually referred to. In this section, we will focus on deriving the subduction coefficients of the nucleon-like state excited by the isospin-3/2, 16 irrep that we will use in subsequent analyses. Subduction coefficients of other lattice irreps can also be derived similarly.

Let $O^{16\pm,A}_{[3/2,3/2]_F}$, $A = 0, \cdots, 7$ be the sixteen zero-momentum lattice operators transforming in the isospin-3/2, 16 irrep. $\pm$ denotes the eigenvalue of I_s, A denotes one of the eight corners, and the subscripts denote the quantum numbers of $\mathrm{SU}(2)_F$. (3.12) is a concrete realization of this operator if all $\chi(\vec{n})$ transform as up-quark fields. The operator class is not important in the following discussion so its label is omitted.

These operators create sixteen different nucleon-like states

$$\left| \left[\frac{3}{2}, \frac{3}{2}\right]_F \left[16\pm, A\right]_{\mathrm{GTS}} \right\rangle \tag{3.23}$$

which are degenerate even on the lattice. The subduction coefficients of $\mathrm{SU}(2)_{\mathrm{SW}_3} \supset \mathrm{W}_3$ is well-known in the literature, so the first thing we do is classifying sixteen components with irreps of W_3 based on the decomposition in (3.21). We get

$$\begin{aligned}
E^+ &= \begin{pmatrix} |[\frac{3}{2},\frac{3}{2}]_F[16+,0]_{\mathrm{GTS}}\rangle \\ |[\frac{3}{2},\frac{3}{2}]_F[16-,0]_{\mathrm{GTS}}\rangle \end{pmatrix}, \quad E^- = \begin{pmatrix} |[\frac{3}{2},\frac{3}{2}]_F[16+,7]_{\mathrm{GTS}}\rangle \\ |[\frac{3}{2},\frac{3}{2}]_F[16-,7]_{\mathrm{GTS}}\rangle \end{pmatrix}, \\
T_1^+ &= \begin{pmatrix} |[\frac{3}{2},\frac{3}{2}]_F[16+,5]_{\mathrm{GTS}}\rangle \\ |[\frac{3}{2},\frac{3}{2}]_F[16+,6]_{\mathrm{GTS}}\rangle \\ |[\frac{3}{2},\frac{3}{2}]_F[16+,3]_{\mathrm{GTS}}\rangle \end{pmatrix}, \quad T_1^- = \begin{pmatrix} |[\frac{3}{2},\frac{3}{2}]_F[16+,1]_{\mathrm{GTS}}\rangle \\ |[\frac{3}{2},\frac{3}{2}]_F[16+,2]_{\mathrm{GTS}}\rangle \\ |[\frac{3}{2},\frac{3}{2}]_F[16+,4]_{\mathrm{GTS}}\rangle \end{pmatrix}, \\
T_2^+ &= \begin{pmatrix} |[\frac{3}{2},\frac{3}{2}]_F[16-,5]_{\mathrm{GTS}}\rangle \\ |[\frac{3}{2},\frac{3}{2}]_F[16-,6]_{\mathrm{GTS}}\rangle \\ |[\frac{3}{2},\frac{3}{2}]_F[16-,3]_{\mathrm{GTS}}\rangle \end{pmatrix}, \quad T_2^- = \begin{pmatrix} |[\frac{3}{2},\frac{3}{2}]_F[16-,1]_{\mathrm{GTS}}\rangle \\ |[\frac{3}{2},\frac{3}{2}]_F[16-,2]_{\mathrm{GTS}}\rangle \\ |[\frac{3}{2},\frac{3}{2}]_F[16-,4]_{\mathrm{GTS}}\rangle \end{pmatrix}
\end{aligned} \tag{3.24}$$

Two things to note here: components with $+1$ eigenvalues in I_s always reside on even corners ($A = 0, 3, 5, 6$) while components with -1 eigenvalues reside on odd corners ($A = 1, 2, 4, 7$); the operators are constructed in such a way that under R_{12} rotations, two components of E irreps have $\pm$ eigenvalues, z-components (third components) of T_1 have $+1$ eigenvalue, z-components of T_2 has -1 eigenvalues. These properties can be checked explicitly by going back to the definitions of baryon operators in [81, 82] and applying the corresponding symmetry transformations. Using this classification and subduction coefficients of $\mathrm{SU}(2)_{\mathrm{SW}_3} \supset \mathrm{SW}_3$ in [90], we can work out the continuum quantum numbers of SW_3 irreps on the lattice.

The last thing we need are the subduction coefficients of $[(\mathrm{SU}(2)_{D_4} \times \mathbb{Z}_4)/\mathbb{Z}_2] \supset D_4 = \{I_s, \Xi_{123}\}$ in (3.16), where ±1 eigenvalues of I_s are used to label the basis vectors of the two-dimensional B irrep. The answer is actually a bit subtle because as we restrict our attention to the nucleon-like state, we implicitly mix the parity operator back into the discussion. So the actual decomposition we should consider really is

$$\mathrm{U}(2)_{D_4} \times \mathbb{Z}_2(P) \supset \mathrm{SU}(2)_{D_4} \times \mathrm{U}(1) \times \mathbb{Z}_2(P) \supset \mathrm{SU}(2)_{D_4} \times \mathbb{Z}_4 \times \mathbb{Z}_2(P) \supset D_4 \times \mathbb{Z}_2(P) \tag{3.25}$$

where $\mathbb{Z}_2$ quotient factors are omitted for simplicity, $\mathbb{Z}_2(P)$ is the $\mathbb{Z}_2$ group generated by the parity operator P, and the extra U(1) phase factor of the taste symmetry explains the origin of $\mathbb{Z}_4$. It might seem redundant to explicitly include $\mathbb{Z}_2(P)$ in the decomposition as it always commutes with any other group elements. However, I_s must contain the parity transformation because $I_s = \Xi_4 P$ by definition, so it is important to keep $\mathbb{Z}_2(P)$ in the decomposition.

We can identify the two-dimensional matrix representation of I_s in the B irrep by the tensor product

$$I_s = e^{-i\sigma_3\pi/2} \otimes e^{-i\pi/2} \otimes 1 = \sigma_3 \tag{3.26}$$

where σ_3 is the Pauli matrix. The first factor in the tensor product comes from the spin-1/2 representation of $R_{12}(\pi) \in \mathrm{SU}(2)_{D_4}$, the second factor comes from the U(1) (or $\mathbb{Z}_4$) phase, and the third factor is the parity of a nucleon. This means the states with $+1/2$ z-component spin in $\mathrm{SU}(2)_{D_4}$ have $+1$ eigenvalues of I_s, while states with $-1/2$ z-component spin have -1 eigenvalues. In other words, the subduction coefficients is trivial for $1/2 \to B$. Although it will not be used here, we can apply the similar technique to $3/2 \to B \oplus B$ by identifying I_s as

$$I_s = e^{i\pi\times\mathrm{diag}(3,1,-1,3)/2} \otimes e^{-i\pi/2} \otimes 1 = \mathrm{diag}(-1,1,-1,1) \tag{3.27}$$

The only difference is that we change the spin-1/2 representation of $R_{12}(\pi)$ to the spin-3/2 one. As we can see, the components naturally split into two B irreps with ±1 eigenvalues in

I_s. The subduction coefficients here are again trivial.

We are now ready to write down the continuum quantum number of the nucleon-like state in the isospin-3/2, 16 irrep in a two-step process. The continuum quantum numbers that we will need are kets of

$$\mathrm{SU}(2)_S \times \mathrm{SU}(2)_F \times \mathrm{SU}(4)_T \supset \mathrm{SU}(2)_S \times \mathrm{SU}(2)_F \times \mathrm{SU}(2)_{\mathbb{Q}_8} \times (\mathrm{SU}(2)_{D_4} \times \mathbb{Z}_4)/\mathbb{Z}_2 \quad (3.28)$$

and the kets are

$$\left| \left[\frac{1}{2}, m^S\right]_S \left[\frac{3}{2}, \frac{3}{2}\right]_F \left[j^{\mathbb{Q}_8}, m^{\mathbb{Q}_8}\right]_{\mathbb{Q}_8} \left[j^{D_4}, m^{D_4}\right]_{D_4} \right\rangle \quad (3.29)$$

where each bracket again denotes the quantum numbers of the corresponding group in the direct product. We will for now ignore the isospin $\mathrm{SU}(2)_F$ label as it is not broken on the lattice. The first step is subducing irreps of $\mathrm{SU}(2)_S \times \mathrm{SU}(2)_{\mathbb{Q}_8}$ to its diagonal subgroup $\mathrm{SU}(2)_{\mathrm{SW}_3}$ as in (3.19), with the subduction coefficients being the standard CG coefficients of SU(2). As an example, we will focus on the spin-2 irrep of $\mathrm{SU}(2)_{\mathrm{SW}_3}$ appearing in the $(3/2, 1/2) \to 2 \oplus 1$ decomposition and let $\mathrm{SU}(2)_{D_4}$ be in the spin-1/2 irrep. They correspond to nucleon-like states in the 20_M irrep of $\mathrm{SU}(4)_T$. The ket can be written as

$$
\begin{gathered}
\mathrm{SU}(2)_S \times \mathrm{SU}(2)_{\mathbb{Q}_8} \times (\mathrm{SU}(2)_{D_4} \times \mathbb{Z}_4)/\mathbb{Z}_2 \supset \mathrm{SU}(2)_{\mathrm{SW}_3} \times (\mathrm{SU}(2)_{D_4} \times \mathbb{Z}_4)/\mathbb{Z}_2 \\
\left|\left[\frac{1}{2}, \pm\frac{1}{2}\right]_S \left[\frac{3}{2}, \pm\frac{3}{2}\right]_{\mathbb{Q}_8} \left[\frac{1}{2}, \pm\frac{1}{2}\right]_{D_4}\right\rangle \rightarrow \left|\left[2, \pm 2\right]_{\mathrm{SW}_3} \left[\frac{1}{2}, \pm\frac{1}{2}\right]_{D_4}\right\rangle \\
\frac{1}{2}\left|\left[\frac{1}{2}, \pm\frac{1}{2}\right]_S \left[\frac{3}{2}, \mp\frac{3}{2}\right]_{\mathbb{Q}_8} \left[\frac{1}{2}, \pm\frac{1}{2}\right]_{D_4}\right\rangle + \sqrt{\frac{3}{4}}\left|\left[\frac{1}{2}, \pm\frac{1}{2}\right]_S \left[\frac{3}{2}, \pm\frac{1}{2}\right]_{\mathbb{Q}_8} \left[\frac{1}{2}, \pm\frac{1}{2}\right]_{D_4}\right\rangle \rightarrow \\
\left|\left[2, \pm 1\right]_{\mathrm{SW}_3} \left[\frac{1}{2}, \pm\frac{1}{2}\right]_{D_4}\right\rangle \\
\sqrt{\frac{1}{2}}\left|\left[\frac{1}{2}, \frac{1}{2}\right]_S \left[\frac{3}{2}, -\frac{1}{2}\right]_{\mathbb{Q}_8} \left[\frac{1}{2}, \pm\frac{1}{2}\right]_{D_4}\right\rangle + \sqrt{\frac{1}{2}}\left|\left[\frac{1}{2}, -\frac{1}{2}\right]_S \left[\frac{3}{2}, \frac{1}{2}\right]_{\mathbb{Q}_8} \left[\frac{1}{2}, \pm\frac{1}{2}\right]_{D_4}\right\rangle \rightarrow \\
\left|\left[2, 0\right]_{\mathrm{SW}_3} \left[\frac{1}{2}, \pm\frac{1}{2}\right]_{D_4}\right\rangle
\end{gathered}
\tag{3.30}
$$

The second and the final step is to subduce these states into irreps of $\mathrm{W}_3 = \mathrm{SW}_3 \times \mathbb{Z}_2$. We have shown in (3.26) that subducing $(\mathrm{SU}(2)_{D_4} \times \mathbb{Z}_4)/\mathbb{Z}_2$ to D_4 gives trivial subduction coefficients. The only non-trivial coefficients come from $\mathrm{SU}(2)_{\mathrm{SW}_3} \supset \mathrm{SW}_3$, which are standard results that can be looked up in many other work. We will use the coefficients in [90] to get

$$
\begin{gathered}
\begin{pmatrix}
\left|\left[\frac{3}{2}, \frac{3}{2}\right]_F \left[2, 0\right]_{\mathrm{SW}_3} \left[\frac{1}{2}, \pm\frac{1}{2}\right]_{D_4}\right\rangle \\
\sqrt{\frac{1}{2}}\left|\left[\frac{3}{2}, \frac{3}{2}\right]_F \left[2, 2\right]_{\mathrm{SW}_3} \left[\frac{1}{2}, \pm\frac{1}{2}\right]_{D_4}\right\rangle + \sqrt{\frac{1}{2}}\left|\left[\frac{3}{2}, \frac{3}{2}\right]_F \left[2, -2\right]_{\mathrm{SW}_3} \left[\frac{1}{2}, \pm\frac{1}{2}\right]_{D_4}\right\rangle
\end{pmatrix} \rightarrow E^{\pm} \\
\begin{pmatrix}
\left|\left[\frac{3}{2}, \frac{3}{2}\right]_F \left[2, 1\right]_{\mathrm{SW}_3} \left[\frac{1}{2}, \pm\frac{1}{2}\right]_{D_4}\right\rangle \\
\sqrt{\frac{1}{2}}\left|\left[\frac{3}{2}, \frac{3}{2}\right]_F \left[2, 2\right]_{\mathrm{SW}_3} \left[\frac{1}{2}, \pm\frac{1}{2}\right]_{D_4}\right\rangle - \sqrt{\frac{1}{2}}\left|\left[\frac{3}{2}, \frac{3}{2}\right]_F \left[2, -2\right]_{\mathrm{SW}_3} \left[\frac{1}{2}, \pm\frac{1}{2}\right]_{D_4}\right\rangle \\
\left|\left[\frac{3}{2}, \frac{3}{2}\right]_F \left[2, -1\right]_{\mathrm{SW}_3} \left[\frac{1}{2}, \pm\frac{1}{2}\right]_{D_4}\right\rangle
\end{pmatrix} \rightarrow T_2^{\pm}
\end{gathered}
\tag{3.31}
$$

where $T_2^{\pm}$ components are in the spherical basis. Combining these results with (3.30) and (3.24), we obtain the continuum quantum numbers of nucleon-like states in the isospin-3/2, 16 irrep. T_1 components can be obtained by subducing the spin-1 irrep of $\mathrm{SU}(2)_{\mathrm{SW}_3}$. We have listed the continuum quantum numbers of all 16 components in Table 3.2.

Table 3.2: Continuum quantum numbers of the sixteen nucleon-like states in the isospin-3/2, 16 irrep.

$\mathrm{SU}(2)_F \times \mathrm{GTS}$	$\mathrm{SU}(2)_S \times \mathrm{SU}(2)_F \times \mathrm{SU}(4)_T \supset$ $\mathrm{SU}(2)_S \times \mathrm{SU}(2)_F \times \mathrm{SU}(2)_{\mathbb{Q}_8} \times \mathrm{SU}(2)_{D_4}$
$\big\|[\frac{3}{2},\frac{3}{2}]_F[16+,0]_{\mathrm{GTS}}\big\rangle$	$\sqrt{\frac{1}{2}}\Big\|[\frac{1}{2},\frac{1}{2}]_S[\frac{3}{2},\frac{3}{2}]_F[\frac{3}{2},-\frac{1}{2}]_{\mathbb{Q}_8}[\frac{1}{2},\frac{1}{2}]_{D_4}\Big\rangle+$ $\sqrt{\frac{1}{2}}\big\|[\frac{1}{2},-\frac{1}{2}]_S[\frac{3}{2},\frac{3}{2}]_F[\frac{3}{2},\frac{1}{2}]_{\mathbb{Q}_8}[\frac{1}{2},\frac{1}{2}]_{D_4}\big\rangle$
$\big\|[\frac{3}{2},\frac{3}{2}]_F[16-,0]_{\mathrm{GTS}}\big\rangle$	$\sqrt{\frac{1}{2}}\Big\|[\frac{1}{2},\frac{1}{2}]_S[\frac{3}{2},\frac{3}{2}]_F[\frac{3}{2},\frac{3}{2}]_{\mathbb{Q}_8}[\frac{1}{2},\frac{1}{2}]_{D_4}\Big\rangle+$ $\sqrt{\frac{1}{2}}\big\|[\frac{1}{2},-\frac{1}{2}]_S[\frac{3}{2},\frac{3}{2}]_F[\frac{3}{2},-\frac{3}{2}]_{\mathbb{Q}_8}[\frac{1}{2},\frac{1}{2}]_{D_4}\big\rangle$
$\mp\sqrt{\frac{1}{2}}\big\|[\frac{3}{2},\frac{3}{2}]_F[16+,1]_{\mathrm{GTS}}\big\rangle-$ $i\sqrt{\frac{1}{2}}\big\|[\frac{3}{2},\frac{3}{2}]_F[16+,2]_{\mathrm{GTS}}\big\rangle$	$\pm\sqrt{\frac{3}{4}}\Big\|[\frac{1}{2},\mp\frac{1}{2}]_S[\frac{3}{2},\frac{3}{2}]_F[\frac{3}{2},\pm\frac{3}{2}]_{\mathbb{Q}_8}[\frac{1}{2},-\frac{1}{2}]_{D_4}\Big\rangle\pm$ $-\frac{1}{2}\big\|[\frac{1}{2},\pm\frac{1}{2}]_S[\frac{3}{2},\frac{3}{2}]_F[\frac{3}{2},\pm\frac{1}{2}]_{\mathbb{Q}_8}[\frac{1}{2},-\frac{1}{2}]_{D_4}\Big\rangle$
$\mp\sqrt{\frac{1}{2}}\big\|[\frac{3}{2},\frac{3}{2}]_F[16-,1]_{\mathrm{GTS}}\big\rangle-$ $i\sqrt{\frac{1}{2}}\big\|[\frac{3}{2},\frac{3}{2}]_F[16-,2]_{\mathrm{GTS}}\big\rangle$	$\frac{1}{2}\Big\|[\frac{1}{2},\mp\frac{1}{2}]_S[\frac{3}{2},\frac{3}{2}]_F[\frac{3}{2},\pm\frac{3}{2}]_{\mathbb{Q}_8}[\frac{1}{2},-\frac{1}{2}]_{D_4}\Big\rangle+$ $\sqrt{\frac{3}{4}}\big\|[\frac{1}{2},\pm\frac{1}{2}]_S[\frac{3}{2},\frac{3}{2}]_F[\frac{3}{2},\pm\frac{1}{2}]_{\mathbb{Q}_8}[\frac{1}{2},-\frac{1}{2}]_{D_4}\Big\rangle$
$\big\|[\frac{3}{2},\frac{3}{2}]_F[16+,3]_{\mathrm{GTS}}\big\rangle$	$\sqrt{\frac{1}{2}}\Big\|[\frac{1}{2},-\frac{1}{2}]_S[\frac{3}{2},\frac{3}{2}]_F[\frac{3}{2},\frac{1}{2}]_{\mathbb{Q}_8}[\frac{1}{2},\frac{1}{2}]_{D_4}\Big\rangle-$ $\sqrt{\frac{1}{2}}\big\|[\frac{1}{2},\frac{1}{2}]_S[\frac{3}{2},\frac{3}{2}]_F[\frac{3}{2},-\frac{1}{2}]_{\mathbb{Q}_8}[\frac{1}{2},\frac{1}{2}]_{D_4}\big\rangle$
$\big\|[\frac{3}{2},\frac{3}{2}]_F[16-,3]_{\mathrm{GTS}}\big\rangle$	$\sqrt{\frac{1}{2}}\Big\|[\frac{1}{2},\frac{1}{2}]_S[\frac{3}{2},\frac{3}{2}]_F[\frac{3}{2},\frac{3}{2}]_{\mathbb{Q}_8}[\frac{1}{2},\frac{1}{2}]_{D_4}\Big\rangle-$ $\sqrt{\frac{1}{2}}\big\|[\frac{1}{2},-\frac{1}{2}]_S[\frac{3}{2},\frac{3}{2}]_F[\frac{3}{2},-\frac{3}{2}]_{\mathbb{Q}_8}[\frac{1}{2},\frac{1}{2}]_{D_4}\big\rangle$
$\big\|[\frac{3}{2},\frac{3}{2}]_F[16+,4]_{\mathrm{GTS}}\big\rangle$	$\sqrt{\frac{1}{2}}\Big\|[\frac{1}{2},-\frac{1}{2}]_S[\frac{3}{2},\frac{3}{2}]_F[\frac{3}{2},\frac{1}{2}]_{\mathbb{Q}_8}[\frac{1}{2},-\frac{1}{2}]_{D_4}\Big\rangle-$ $\sqrt{\frac{1}{2}}\big\|[\frac{1}{2},\frac{1}{2}]_S[\frac{3}{2},\frac{3}{2}]_F[\frac{3}{2},-\frac{1}{2}]_{\mathbb{Q}_8}[\frac{1}{2},-\frac{1}{2}]_{D_4}\big\rangle$
$\big\|[\frac{3}{2},\frac{3}{2}]_F[16-,4]_{\mathrm{GTS}}\big\rangle$	$\sqrt{\frac{1}{2}}\Big\|[\frac{1}{2},\frac{1}{2}]_S[\frac{3}{2},\frac{3}{2}]_F[\frac{3}{2},\frac{3}{2}]_{\mathbb{Q}_8}[\frac{1}{2},-\frac{1}{2}]_{D_4}\Big\rangle-$ $\sqrt{\frac{1}{2}}\big\|[\frac{1}{2},-\frac{1}{2}]_S[\frac{3}{2},\frac{3}{2}]_F[\frac{3}{2},-\frac{3}{2}]_{\mathbb{Q}_8}[\frac{1}{2},-\frac{1}{2}]_{D_4}\big\rangle$

(continue on the next page)

(Table 3.2, continued)

$\mp\sqrt{\frac{1}{2}}\lvert[\frac{3}{2},\frac{3}{2}]_F[16+,5]_{\mathrm{GTS}}\rangle - i\sqrt{\frac{1}{2}}\lvert[\frac{3}{2},\frac{3}{2}]_F[16+,6]_{\mathrm{GTS}}\rangle$	$\pm\sqrt{\frac{3}{4}}\Big\lvert[\frac{1}{2},\mp\frac{1}{2}]_S[\frac{3}{2},\frac{3}{2}]_F[\frac{3}{2},\pm\frac{3}{2}]_{\mathbb{Q}_8}[\frac{1}{2},\frac{1}{2}]_{D_4}\Big\rangle \pm -\frac{1}{2}\lvert[\frac{1}{2},\pm\frac{1}{2}]_S[\frac{3}{2},\frac{3}{2}]_F[\frac{3}{2},\pm\frac{1}{2}]_{\mathbb{Q}_8}[\frac{1}{2},\frac{1}{2}]_{D_4}\Big\rangle$
$\mp\sqrt{\frac{1}{2}}\lvert[\frac{3}{2},\frac{3}{2}]_F[16-,5]_{\mathrm{GTS}}\rangle - i\sqrt{\frac{1}{2}}\lvert[\frac{3}{2},\frac{3}{2}]_F[16-,6]_{\mathrm{GTS}}\rangle$	$\frac{1}{2}\Big\lvert[\frac{1}{2},\mp\frac{1}{2}]_S[\frac{3}{2},\frac{3}{2}]_F[\frac{3}{2},\pm\frac{3}{2}]_{\mathbb{Q}_8}[\frac{1}{2},\frac{1}{2}]_{D_4}\Big\rangle + \sqrt{\frac{3}{4}}\lvert[\frac{1}{2},\pm\frac{1}{2}]_S[\frac{3}{2},\frac{3}{2}]_F[\frac{3}{2},\pm\frac{1}{2}]_{\mathbb{Q}_8}[\frac{1}{2},\frac{1}{2}]_{D_4}\Big\rangle$
$\lvert[\frac{3}{2},\frac{3}{2}]_F[16+,7]_{\mathrm{GTS}}\rangle$	$\sqrt{\frac{1}{2}}\Big\lvert[\frac{1}{2},\frac{1}{2}]_S[\frac{3}{2},\frac{3}{2}]_F[\frac{3}{2},-\frac{1}{2}]_{\mathbb{Q}_8}[\frac{1}{2},-\frac{1}{2}]_{D_4}\Big\rangle + \sqrt{\frac{1}{2}}\lvert[\frac{1}{2},-\frac{1}{2}]_S[\frac{3}{2},\frac{3}{2}]_F[\frac{3}{2},\frac{1}{2}]_{\mathbb{Q}_8}[\frac{1}{2},-\frac{1}{2}]_{D_4}\Big\rangle$
$\lvert[\frac{3}{2},\frac{3}{2}]_F[16-,7]_{\mathrm{GTS}}\rangle$	$\sqrt{\frac{1}{2}}\Big\lvert[\frac{1}{2},\frac{1}{2}]_S[\frac{3}{2},\frac{3}{2}]_F[\frac{3}{2},\frac{3}{2}]_{\mathbb{Q}_8}[\frac{1}{2},\frac{1}{2}]_{D_4}\Big\rangle + \sqrt{\frac{1}{2}}\lvert[\frac{1}{2},-\frac{1}{2}]_S[\frac{3}{2},\frac{3}{2}]_F[\frac{3}{2},-\frac{3}{2}]_{\mathbb{Q}_8}[\frac{1}{2},-\frac{1}{2}]_{D_4}\Big\rangle$

In this section, we have successfully subduced continuum states of $\mathrm{SU}(2)_S \times \mathrm{SU}(2)_F \times \mathrm{SU}(4)_T$ onto lattice baryons and derived the corresponding subduction coefficients. Table 3.2 presents the results for nucleon-like states, which are needed to extract physical matrix elements in Chapter 4.

Chapter 4

Nucleon mass and matrix elements with highly-improved staggered quarks

In Chapters 2 and 3, we have demonstrated the theoretical details of how to extract physical baryon observables with staggered valence quarks. In this Chapter, we will show explicitly how the formalism can be applied in practice to actual lattice simulations, and what analysis techniques have been proven to be the most useful in analyzing staggered baryon correlators.

Our focus is on the three simplest baryonic observables – the nucleon mass and axial-vector and vector charges – which are well known experimentally and serve as benchmarks to our calculations. As we mentioned in the introduction, despite being "easy" observables to simulate, extracting unambiguous lattice results free of systematic errors is still computationally difficult. The main culprit is the exponential dampening of signal-to-noise ratios in baryon correlators as we pull operators apart in time, which is crucial in eliminating excited state contaminations. The only method to circumvent the problem at the moment is to increase the number of Monte-Carlo samples which are costly to compute. Nevertheless, thanks to both algorithmic developments and Moore's law growth in computational power, we have seen some impressive lattice results in the last few years with fully controlled systematic errors – see [80] for a review of the current status of lattice calculations.

We contribute to the effort by providing the first calculations of nucleon observables using both staggered valence and sea quarks. Especially, we are using the set of gauge ensembles with Highly improved Staggered Quarks (HISQ) action [83] generated by the MILC collaboration [4, 55]. The HISQ action is a variant of the improved staggered action with all the symmetries mentioned in Section 3.1 and designed to reduce various taste-symmetry breaking effects introduced by the lattice discretization. The MILC collaboration was able to generate the largest set of gauge ensembles in existence and made them publicly available due to the speed of staggered simulations. Because of the prohibitive costs of generating gauge ensembles for each project, the two most precise lattice results of nucleon matrix elements to date shown in [80] are based on simulations with MILC HISQ ensembles [94, 95]. However, both results are simulated with different valence quark actions – the Callat collaboration used Mobiüs domain wall fermions [94] whereas the PNDME collaboration used the Wilson-clover fermions [95] – and those simulations have the additional complication of tuning the quark masses to ensure a unitary theory in the continuum limit. It is therefore desirable to also use the HISQ action for valence quarks so that this complication can be avoided[1]. One can also be benefited from the speed of staggered simulations to produce more precise predictions.

4.1 Nucleon mass with highly improved staggered quarks

We need to construct two-point correlators with staggered baryon interpolators to extract the nucleon mass. As mentioned in Chapter 4, we use isospin-3/2, 16 irrep operators in this work which creates one nucleon-like and three Δ-like states in its positive parity ground states; the spectrum of the negative parity channel is unknown and will be deduced tentatively from fit results. The zero momentum operators will be denoted by

$$O^{16\pm,D;\mathrm{cls}R}_{[3/2,3/2]_F}(t),\ \ (D \in \{0,\cdots,7\},\ \ R \in \{2,3,4,6\}) \tag{4.1}$$

$16\pm$ denotes two sets of eight components within the 16 irrep with ±1 eigenvalues of R_{12}, D denotes one of the eight corners of a spatial cube as defined in (3.9), R denotes the class of the operator, and the subscript denotes the isospin quantum numbers. To simplify the problem, we let all operators transform as the highest weight states in the isospin-3/2 irrep, namely, all quarks fields transform as up-quark fields. See operators definitions in [2, 82].

---

[1] Because of the fourth root in quark determinants, all simulations with rooted staggered quarks are partially quenched and unitarity is always violated at non-zero lattice spacing [2].

The only non-vanishing two-point correlators that we can construct are

$$C_{2\text{pt}}^{16\pm D;(R_1,R_2)}(t) \equiv \left\langle O_{[3/2,3/2]_F}^{16\pm,D;\text{cls}R_1}(t)\ \overline{O}_{[3/2,3/2]_F}^{16\pm,D;\text{cls}R_2}(0) \right\rangle \tag{4.2}$$

Note that because different operator classes excite the same states, we can get a matrix of correlators by using different operator classes at the source and sink. Other correlators, such as using different D components at the source and sink, must vanish according to the lattice symmetries. Using the Hermiticity property of the staggered Dirac operator [49] and the charge conjugation symmetry of the staggered action [78, 81], we can show that these two-point correlators are always real.

There is a total of $256 = 16 \times 4^2$ non-vanishing correlators. We can reduce this number to $16 = 4^2$ by noticing that

$$\begin{aligned} C_{2\text{pt}}^{16\pm,D;(R_1,R_2)}(t) &= C_{2\text{pt}}^{16\pm,B;(R_1,R_2)}(t), \\ C_{2\text{pt}}^{16\mp,D;(R_1,R_2)}(t) &= C_{2\text{pt}}^{16\pm,B;(R_1,R_2)}(t) \end{aligned} \tag{4.3}$$

for arbitrary $D, B \in \{0, \cdots, 7\}$, which can be derived by applying shift and rotation symmetries. In other words, correlators constructed from any one of the 16 components within the 16 irrep are identical in the ensemble average, so we will only consider the +0 component $C_{2\text{pt}}^{16+,0;(R_1,R_2)}(t)$. In practice, all 16 components are averaged together to reduce the uncertainties of correlators.

To illustrate how correlators defined in (4.2) can be implemented on computers, we will use the zeroth component class-1, isospin-3/2, 8 irrep operator, where all three quark fields reside at the origin of the spatial cube. Following the notations in (4.1), this particular operator is written as

$$O_{[3/2,3/2]_F}^{8,0;\text{cls}1}(t) = \sum_{\vec{n}\in\text{even}} \sum_{a,b,c} \epsilon_{abc} \chi^a(\vec{n},t) \chi^b(\vec{n},t) \chi^c(\vec{n},t) \tag{4.4}$$

where we sum over all spatial sites modulo two to excite only zero momentum states and antisymmetrize over color indices. The correlator becomes

$$
\begin{aligned}
C_{\mathrm{2pt}}^{8,0;(1,1)}(t) &= \left\langle O_{[3/2,3/2]_F}^{8,0;\mathrm{cls1}}(t)\ \overline{O}_{[3/2,3/2]_F}^{8,0;\mathrm{cls1}}(0)\right\rangle \\
&= \sum_{\vec{n},\vec{m}\in\mathrm{even}}\ \sum_{a,b,c}\sum_{u,v,w}\epsilon_{abc}\epsilon_{uvw}\times \\
&\qquad\qquad \left\langle \chi^a(\vec{n},t)\chi^b(\vec{n},t)\chi^c(\vec{n},t)\overline{\chi}^u(\vec{m},0)\overline{\chi}^v(\vec{m},0)\overline{\chi}^w(\vec{m},0)\right\rangle \\
&= 6\sum_{\vec{n},\vec{m}\in\mathrm{even}}\ \sum_{a,b,c}\sum_{u,v,w}\epsilon_{abc}\epsilon_{uvw}\wick{\c1{\chi}^a(\vec{n},t)\c2{\chi}^b(\vec{n},t)\c3{\chi}^c(\vec{n},t)\c1{\overline{\chi}}^u(\vec{m},0)\c2{\overline{\chi}}^v(\vec{m},0)\c3{\overline{\chi}}^w(\vec{m},0)} \\
&= -6\sum_{\vec{n},\vec{m}\in\mathrm{even}}\ \sum_{a,b,c}\sum_{u,v,w}\epsilon_{abc}\epsilon_{uvw}G^{a;u}(\vec{n},t;\vec{m},0)G^{b;v}(\vec{n},t;\vec{m},0)G^{c;w}(\vec{n},t;\vec{m},0)
\end{aligned}
\tag{4.5}
$$

The factor of 6 in the third line accounts for all other identical Wick contractions, and the negative sign in the fourth line comes from anticommuting fermionic fields. $G^{a;u}(\vec{n},t_1;\vec{m},t_2)$ are propagators that satisfy

$$
\sum_{b,\vec{n},t_2} D_{\mathrm{sg}}^{a;b}(\vec{n}_1,t_1;\vec{n}_2,t_2)G^{b;c}(\vec{n}_2,t_2;\vec{n}_3,t_3) = \delta_{a,c}\delta_{\vec{n}_1,\vec{n}_3}\delta_{t_1,t_3} \tag{4.6}
$$

where $D_{\mathrm{sg}}^{a;b}(\vec{n}_1,t_1;\vec{n}_2,t_2)$ is the HISQ Dirac operator [83]. So to construct the correlator in (4.5), we have to solve for the Dirac equation in (4.6) which boils down to finding the inverse matrix of $D_{\mathrm{sg}}^{a;b}(\vec{n}_1,t_1;\vec{n}_2,t_2)$ on each gauge configuration. Inverting such a large matrix is impossible with our current technology: a typical lattice simulation involves say $50^4 \approx 10$ million lattice sites which leads to the dimension of the Dirac matrix to be 30-million-by-30-million when the color degrees of freedom are included. Fortunately, the Dirac matrix is sparse with only non-zero entries on diagonal blocks, so we can imagine one day this will become feasible. $G^{b;c}(\vec{n}_2,t_2;\vec{n}_3,t_3)$ is usually called an all-to-all propagator in the lattice jargon as it connects any lattice sites to any other sites.

This issue can be circumvented by partially solving for the matrix inverse. The most common example is the use of so-called the point-to-all propagator for which only a single column of the matrix inverse is solved. If we think of the right-hand side of (4.6) as column vectors that we call sources, by fixing them to non-zero values at a single point on the lattice (point source) say $(\vec{n}_3, t_3) = (\vec{n}_0, t_0)$, the problem is reduced to finding the solution to a system of linear equations. Many efficient algorithms can achieve this task; see [96–98] for some recent advances in algorithmic developments. In other words, we are solving for

$$\sum_{b,\vec{n},t_2} D^{a;b}_{\mathrm{sg}}(\vec{n}_1, t_1; \vec{n}_2, t_2)\widetilde{G}^{b;c}_{\mathrm{pt}}(\vec{n}_2, t_2) = \delta_{a,c}\delta_{\vec{n}_1,\vec{n}_0}\delta_{t_1,t_0} \tag{4.7}$$

where

$$\widetilde{G}^{b;c}_{\mathrm{pt}}(\vec{n}_2, t_2) \equiv G^{b;c}(\vec{n}_2, t_2; \vec{n}_0, t_0) \tag{4.8}$$

We can employ more complicated sources other than a point source to fit our needs. The one that we will be using in this work is the so-called corner-wall propagators, which are solutions to the equations [2]

$$\sum_{b,\vec{n},t_2} D^{a;b}_{\mathrm{sg}}(\vec{n}_1, t_1; \vec{n}_2, t_2)\widetilde{G}^{b;c}_{\mathrm{cw}}(\vec{n}_2, t_2) = \sum_{\vec{n}_3\in\mathrm{even}} \delta_{a,c}\delta_{\vec{n}_1,\vec{n}_3}\delta_{t_1,t_0} \tag{4.9}$$

where

$$\widetilde{G}^{b;c}_{\mathrm{cw}}(\vec{n}_2, t_2) \equiv \sum_{\vec{n}_3\in\mathrm{even}} G^{b;c}(\vec{n}_2, t_2; \vec{n}_3, t_0) \tag{4.10}$$

In other words, instead of fixing the sources to be non-zeros at a single spatial coordinate $\vec{n}_0$, the corner-wall sources are non-vanishing on all even spatial lattice sites. The time coordinate is still fixed at t_0. We can accommodate the use of corner-wall propagators by modifying the creation operator in (4.5) to

$$\begin{aligned}
C^{8,0;(1,1)}_{\text{2pt,cw}}(t) &\equiv \left\langle O^{8,0;\text{cls1}}_{[3/2,3/2]_F}(t)\ \overline{\mathcal{O}}^{8,0;\text{cls1}}_{[3/2,3/2]_F}(0)\right\rangle \\
&\equiv \sum_{\vec{n}\in\text{even}}\ \sum_{\vec{m}_1\in\text{even}}\ \sum_{\vec{m}_2\in\text{even}}\ \sum_{\vec{m}_3\in\text{even}}\ \sum_{a,b,c}\ \sum_{u,v,w} \epsilon_{abc}\epsilon_{uvw}\times \\
&\qquad \left\langle \chi^a(\vec{n},t)\chi^b(\vec{n},t)\chi^c(\vec{n},t)\overline{\chi}^u(\vec{m}_1,0)\overline{\chi}^v(\vec{m}_2,0)\overline{\chi}^w(\vec{m}_3,0)\right\rangle \\
&= -6\sum_{\vec{n}\in\text{even}}\ \sum_{a,b,c}\ \sum_{u,v,w} \epsilon_{abc}\epsilon_{uvw}\widetilde{G}^{a;u}_{\text{cw}}(\vec{n},t)\widetilde{G}^{b;v}_{\text{cw}}(\vec{n},t)\widetilde{G}^{c;w}_{\text{cw}}(\vec{n},t)
\end{aligned} \tag{4.11}$$

where we have chosen $t_0 = 0$. Compared to (4.5), (4.11) sums over spatial coordinates separately for each source quark field so that we can write the correlator as a sum of corner-wall propagators. For non-local operators such as those transform in the isospin-3/2, 16 irrep, the simulations are done on Coulomb-gauge-fixed configurations so the correlators will be non-vanishing. We could instead perform non-gauge-fixed simulations by adding gauge links for both source and sink operators, but adding gauge links at the source requires extra propagator solves that are extremely costly; on the other hand, adding gauge links at the sink can be done with little to no extra costs, so we are free to include them or not in gauge-fixed simulations as we have observed in our tests that they make little difference to correlators. We have found empirically that operators constructed with corner-wall sources give better overlaps to the nucleon-like state. For simplicity, we will ignore the "cw" subscripts on correlators and assume we always use corner-wall propagators.

4.1.1 Spectral decomposition of staggered baryon two-point correlators

$C_{\text{2pt}}^{16+,0;(R_1,R_2)}(t)$, $R_1,\ R_2 \in \{2,3,4,6\}$ has a spectral decomposition of [2]

$$\begin{aligned} C_{\text{2pt}}^{16+,0;(R_1,R_2)}(t) = &\sum_{i=0} a_{+i}^{(R_1)} b_{+i}^{(R_2)} \left(e^{-m_{+i}t} - (-1)^t e^{-m_{+i}(L_T-t)}\right) + \\ &\sum_{j=0} a_{-j}^{(R_1)} b_{-j}^{(R_2)} \left(-(-1)^t e^{-m_{-j}t} + e^{-m_{-j}(L_T-t)}\right) \end{aligned} \tag{4.12}$$

States of ± parities that can be excited by staggered baryon operators are denotes by $\pm k$, $k = 0, 1, \cdots$ subscripts with masses $m_{\pm 0} < m_{\pm 1} < \cdots$, $a_{\pm k}^{(R_1)}$ and $b_{\pm k}^{(R_2)}$ are source and sink overlap factors, and L_T is the time extent of the lattice so $t \in [0, L_T - 1]$. For two-point functions, we can neglect terms involving $e^{-m_{\pm k}L_T}$ by redefining the correlators to be

$$\begin{aligned} &C_{\text{2pt}}^{16+,0;(R_1,R_2)}(t) \to \\ &\qquad \widetilde{C}_{\text{2pt}}^{16+,0;(R_1,R_2)}(t) \equiv \frac{C_{\text{2pt}}^{16+,0;(R_1,R_2)}(t) - (-1)^{L_T-t} C_{\text{2pt}}^{16+,0;(R_1,R_2)}(L_T - t)}{2} \end{aligned} \tag{4.13}$$

where t is now restricted to $t \in [0, L_T/2-1]$ (L_T is always even). As long as $e^{-m_{\pm k}L_T}/e^{-m_{\pm k}t} \ll$ correlator errors within this time domain, the newly defined correlator has a simplified spectral decomposition that reads

$$\widetilde{C}_{\text{2pt}}^{16+,0;(R_1,R_2)}(t) = \sum_{i=0} a_{+i}^{(R_1)} b_{+i}^{(R_2)} e^{-m_{+i}t} - \sum_{j=0} a_{-j}^{(R_1)} b_{-j}^{(R_2)} (-1)^t e^{-m_{-j}t} \tag{4.14}$$

Since L_T is large and the data are noisy, the condition is always satisfied so we will use (4.14) in two-point correlators analyses make no distinctions between $\widetilde{C}_{\text{2pt}}^{16+,0;(R_1,R_2)}(t)$ and $C_{\text{2pt}}^{16+,0;(R_1,R_2)}(t)$.

We know the first four states in the positive parity channel: $m_N \equiv m_{+0}$ is the nucleon-like state, and $m_{\Delta_i} \equiv m_i$, $i = 1, 2, 3$ are the three Δ-like states. Note that in principle, the sums in (4.14) can be extended to an arbitrarily large number of states as long as those excited states have the same quantum numbers as the operators. For the staggered nucleon operator we use here, the lowest positive parity excited states, other than the three Δ-like states, could include nucleon-pion states with various tastes, the Roper resonance $N(1440)$, and other radial excitations. For the negative parity channel, the excited states could include nucleon-pion states with negative parities, the nucleon resonance $N(1520)$, and other higher excitations.

On finite lattices, extracting masses and overlap factors by fitting correlators to sums of exponentials in (4.14) is an ill-posed problem that admits many solutions. The issue is exacerbated in practice as the Monte-Carlo data for baryon correlators are noisy, so in practice, it is extremely difficult to extract precise parameters of states beyond the first few. A regularization scheme has to be applied in order to properly define a solution. Fortunately, we are only interested in the mass of the nucleon-like state in the ground state. We observe that in the large t limit

$$C_{2\text{pt}}^{16+,0;(R_1,R_2)}(t) \sim a_{+0}^{(R_1)} b_0^{(R_2)} e^{-m_N t} \tag{4.15}$$

so the correlators are dominated by the ground state exponential only. We can define the effective mass of a correlator $C(t)$

$$M_{\text{eff}}(t) \equiv \frac{1}{\tau} \ln\left(\frac{C(t)}{C(t+\tau)}\right) \tag{4.16}$$

where $\tau = 2$ in this work. Again, in the large t limit M_{eff} for all our correlators becomes

$$M_{\text{eff}}(t) \sim m_N \tag{4.17}$$

which is simply the mass of the nucleon-like state we would like to extract. If we plot

$M_{\text{eff}}(t)$, we will see that as t increases, the curve plateaus to a value that gives the mass of the hadron. The effective mass plot, and hence, the plateau method, is a useful tool in visualizing two-point correlators to see how much excited state contaminations there are, however, it is not a reliable method to extract masses because it relies on the fact that t has to be large enough so other excited state contribution to the correlator can be completely ignored. For baryon correlators, it is almost always the case that as we reach a large enough t that excited state contributions can be neglected, the correlators are already overwhelmed with noises. The nucleon mass extracted from the plateau method could then be biased depending on the data fluctuation.

A better method that is used in almost all lattice analyses is to truncate the number of states appearing in (4.14) and fit the correlator data within a portion of the time domain $t_{\text{fit}} \in [t_{\text{min}}, t_{\text{max}}]$ where the truncated spectral decomposition is a valid model because the omitted states are either too heavy and/or have small overlap factors to the operator. The fit could be just a simple maximum likelihood estimation in which we find the best parameters by minimizing the χ^2 difference between our model and the data, or we can further regularize it by including Bayesian priors for known parameters and minimize the augmented χ^2 instead [99, 100]. Regardless of the fit method one adopts in his or her analyses, there are assumptions built into those models such as the choices of t_{min} and t_{max}, the number of states to keep in the correlators, and priors in the Bayesian framework. Physical parameters should be consistent with each other under reasonable perturbations of these model assumptions around their nominal values. For example, parameters extracted from overfitted results will vary wildly as we perturb the values of t_{min}. It is therefore important to make sure the extracted nucleon mass is stable under variations which we will check explicitly.

The covariance matrix of the best-fit parameters from minimizing either χ^2 or augmented χ^2 can be calculated from the inverse of the Hessian matrix, which is the second derivative of the negative log-likelihood function with respect to those parameters. The Hessian matrix for our correlator models can be calculated easily with pen and paper so it requires no extra computations. However, the covariance matrix obtained in this way is only valid if the data have small errors, which is not always the case. Resampling methods such as bootstrap and jackknife [101] provide more reliable estimates of the covariance matrix by relying on fewer assumptions on our data. The price we have to pay is that they require more computation time in addition to the χ^2 minimization, but it is a price that most lattice calculations are willing to pay nowadays as the additional computational requirement is still minimal compared to the actual Monte-Carlo simulations.

In the bootstrap resampling method, suppose we try to estimate the variance of an estimator from a dataset of size N. We first resample the original dataset, meaning to randomly sample a new dataset of the same size N from the original dataset, and allow for the possibility that the same data entry can appear more than once in the new dataset. The estimator can then be computed on this new dataset. This procedure is performed N_b times in total to obtain a distribution of the estimator from which the variance can be inferred. An important assumption of the bootstrap method is that the original dataset must be statistically independent, and the dataset is large enough such that it mimics the underlying population distribution. We have found that for lattice data in practice, the bootstrap method works well as long as we perform large enough bootstrap iterations, say, $N_b \sim 1000$, and have ~ 1000 statistically independent samples of correlator data; in the jackknife resampling method, we resample the original dataset N times where the i-th resampled dataset ($i \in [0, N-1]$) of size $N-1$ is obtained by removing the i-th data entry. The variance can be inferred again from the distribution of the estimator from resampled datasets. Both bootstrap and jackknife methods are popular among lattice practitioners and work equally well in most cases. In this work, all errors on posterior parameters are estimated from $N_b = 1000$ bootstrap samples.

4.1.2 Variational Method for staggered baryon two-point correlators

We are only interested in the value of the nucleon-like state mass $m_{+0} \equiv m_N$ in (4.14) and treat excited state contributions as nuisance parameters. A direct fit to a correlator can yield an estimate of the nucleon-like mass, but if the operators have large overlaps to the excited states, then it could be hard to cleanly disentangle the excited state contaminations from the posterior estimate unless the data have small errors, which are hard to come by for nucleon correlators. This will show up as instabilities in the nucleon-like mass estimates when we slightly perturb the fit parameters such as t_{min} and priors.

It is much preferable if we can preprocess the correlators before fitting in such a way that the procedure dampens the contributions from nuisance parameters. The variational method [102–105] is a way to construct an improved correlator with better overlap to the state. We start off with a matrix of correlators constructed from sets of source and sink operators. In our applications, we have a four-by-four correlator matrix constructed from different operator classes

$$\mathbf{C}_{\mathrm{2pt}}^{16+,0;(R_1,R_2)}(t) \equiv \begin{pmatrix} C_{\mathrm{2pt}}^{16+,0;(2,2)}(t) & C_{\mathrm{2pt}}^{16+,0;(2,3)}(t) & C_{\mathrm{2pt}}^{16+,0;(2,4)}(t) & C_{\mathrm{2pt}}^{16+,0;(2,6)}(t) \\ C_{\mathrm{2pt}}^{16+,0;(3,2)}(t) & C_{\mathrm{2pt}}^{16+,0;(3,3)}(t) & C_{\mathrm{2pt}}^{16+,0;(3,4)}(t) & C_{\mathrm{2pt}}^{16+,0;(3,6)}(t) \\ C_{\mathrm{2pt}}^{16+,0;(4,2)}(t) & C_{\mathrm{2pt}}^{16+,0;(4,3)}(t) & C_{\mathrm{2pt}}^{16+,0;(4,4)}(t) & C_{\mathrm{2pt}}^{16+,0;(4,6)}(t) \\ C_{\mathrm{2pt}}^{16+,0;(6,2)}(t) & C_{\mathrm{2pt}}^{16+,0;(6,3)}(t) & C_{\mathrm{2pt}}^{16+,0;(6,4)}(t) & C_{\mathrm{2pt}}^{16+,0;(6,6)}(t) \end{pmatrix} \tag{4.18}$$

Note that because we are using corner-wall sources for solving propagators, the matrix is not symmetric, namely,

$$C_{\mathrm{2pt}}^{16+,0;(R_1,R_2)}(t) \neq C_{\mathrm{2pt}}^{16+,0;(R_2,R_1)}(t) \tag{4.19}$$

We can solve for the generalized eigenvalue problems (GEVPs) to obtain left/right eigenvectors and eigenvalues

$$\begin{aligned}
\mathbf{C}_{\text{2pt}}^{16+,0;(R_1,R_2)}(t)v_R^{(i)} &= \lambda^{(i)}\mathbf{C}_{\text{2pt}}^{16+,0;(R_1,R_2)}(t_0)v_R^{(i)}, \\
\left(v_L^{(i)}\right)^T\mathbf{C}_{\text{2pt}}^{16+,0;(R_1,R_2)}(t) &= \lambda^{(i)}\left(v_L^{(i)}\right)^T\mathbf{C}_{\text{2pt}}^{16+,0;(R_1,R_2)}(t_0) \qquad (i=0,1,2,3)
\end{aligned} \tag{4.20}$$

where $v_R^{(i)}$ and $v_L^{(i)}$ are column vectors and $|\lambda^{(0)}| \geq |\lambda^{(1)}| \geq \cdots$. For applications involving ground states only, we choose another timeslice $t_0 < t$ to first suppress the excited contribution, so eigenvalues and eigenvectors are functions of t and t_0.

In the large t limit, the eigenvalues converge to [104]

$$\lambda^{(i)}(t,t_0) \sim e^{-E_i t} \tag{4.21}$$

where E_i is the energy of the i-th excited state in the spectrum and $E_0 \leq E_1 \leq \cdots$ conforming to the ordering of eigenvalues. Going beyond the large time limit, it has been shown with the second order perturbation theory that the eigenvalues, similar to the spectral decomposition of two-point correlation functions, can be written as sums of exponentials with higher energies. Standard fit methods for correlation functions then can be applied to extract the nucleon mass from eigenvalues.

On the other hand, we can think of eigenvectors as the optimal linear combination coefficients for the operators to project onto that particular state. An improved correlator can be constructed by taking the scalar product

$$C_{\text{2pt}}^{16+,0}(t) \equiv \left(v_L^{(0)}\right)^T\mathbf{C}_{\text{2pt}}^{16+,0;(R_1,R_2)}(t)v_R^{(0)} \tag{4.22}$$

Because the improved two-point correlator is simply the linear combination of original correlators, it retains the form of the spectral decomposition defined in (4.14), albeit with different overlap factors that are enhanced for the ground state nucleon. In practice, the nucleon mass can be extracted via either eigenvalues or the improved two-point correlator. We have found that in our data those two methods give almost identical estimates of the nucleon mass. However, fits to eigenvalues are only useful for extracting energies whereas the same set of eigenvectors can be applied to improve higher-point functions. We will come back to the improved correlator method in the next section when we work with three-point correlator functions and restrict our attention to eigenvalues here.

The presence of negative parity, oscillating states in the spectral decomposition (4.14) makes the variational method slightly more complicated for staggered correlators. The eigenvalues will still be the sum of exponentials, however, states with negative parity will again have extra $-(-1)^t$ factors in front [106]. Because now the eigenvalues contain oscillatory terms, it may be impossible to label them consistently in such a way that $|\lambda^{(0)}| \geq |\lambda^{(1)}| \geq \cdots$ for all t. In the intermediate t region, eigenvalues for the first excited state might be smaller than eigenvalues for the ground state so the labels on eigenvalues are ambiguous. The labeling issue goes away as t grows since only one exponential can contribute in the large t limit. We have found that in our simulations that although the eigenvalues for the excited state did cross below the eigenvalues for the ground states, it is easy to identity which sets of eigenvalues belong to which states by observing the overall oscillatory patterns.

Even though the presence of negative parity states poses no significant hindrance to the variational method, they still are nuisance parameters that we would like to completely eliminate in our analyses. We use the fact that negative parity contributions to either the eigenvalues or correlation functions always come with oscillatory terms proportional to $(-1)^t$ and propose to solve for the eigenvalue equations

$$\mathbf{D}_{\text{2pt}}^{16+,0;(R_1,R_2)}(t,t_0)\widetilde{v}_R^{(i)} = \widetilde{\lambda}^{(i)}\widetilde{v}_R^{(i)} \qquad (i = 0, 1, 2, 3) \tag{4.23}$$

where

$$\begin{aligned}\mathbf{D}_{\text{2pt}}^{16+,0;(R_1,R_2)}(t,t_0) \equiv \frac{1}{4}\Big\{ &\Big(\mathbf{C}_{\text{2pt}}^{16+,0;(R_1,R_2)}(t_0+1)\Big)^{-1}\mathbf{C}_{\text{2pt}}^{16+,0;(R_1,R_2)}(t+1)+\\ &2\Big(\mathbf{C}_{\text{2pt}}^{16+,0;(R_1,R_2)}(t_0)\Big)^{-1}\mathbf{C}_{\text{2pt}}^{16+,0;(R_1,R_2)}(t)+\\ &\Big(\mathbf{C}_{\text{2pt}}^{16+,0;(R_1,R_2)}(t_0-1)\Big)^{-1}\mathbf{C}_{\text{2pt}}^{16+,0;(R_1,R_2)}(t-1)\Big\}\end{aligned} \tag{4.24}$$

Expressions for left eigenvectors follow naturally from these two definitions. For large t and t_0, we expect

$$\widetilde{\lambda}^{(i)}(t,t_0) \sim \lambda^{(i)}(t,t_0) \tag{4.25}$$

but for intermediate t and t_0 where the fittings take place, the weighted average cancels out the oscillatory terms and we are only left with positive parity excited states. The small price we have to pay for this enhanced signal in the positive parity channel is a slight reduction in the signal-to-noise ratio due to the averaging in time. In Section 4.2.4, we will introduce an alternative method to reduce the negative parity channel via weighted averaging by operating directly on the correlators instead of eigenvalues.

4.1.3 Simulation details

For the nucleon mass work, we are using three ensembles at three lattice spacings of the HISQ gauge-link ensembles generated by the MILC collaborations [4, 55]. Each ensemble includes two degenerate light sea quarks, one strange sea quark, and one charm sea quark ("2+1+1") via the fourth-root determinants of the HISQ action, and uses the improved Lüscher-Weisz action [107] for discretizing the gauge action. The same staggered action is used for solving the propagators. To avoid complications involving chiral extrapolations (extrapolating the nucleon mass from higher pion masses to the physical value) where the effective theories are poorly convergent at even moderately large pion masses (see [108–110] for reviews), we only

Table 4.1: Ensembles used in the nucleon mass calculations. The lattice spacings are determined with the mass-independent f_{p4s} scheme [4]; m_l, m_s, and m_c are the masses of up/down, strange, and charm quarks, respectively, in lattice units; N_{cfg} is the number of configurations for each ensemble, and on each configuration, we measure on N_{src} different time sources to increase statistics. All ensembles are tuned to the physical pion mass barring for small mistuning errors which will be corrected in the analysis.

a (fm)	β	$L^3 \times L_T$	m_π (MeV)	m_l	m_s	m_c	N_{cfg}	N_{src}
0.1529(4)	5.8	$32^3 \times 48$	135	0.002425	0.06730	0.8447	3500	2
0.1222(3)	6.0	$48^3 \times 64$	135	0.001907	0.05252	0.6382	1000	2
0.0879(3)	6.3	$64^3 \times 96$	128	0.001200	0.03630	0.4320	1047	1

perform simulations on physical ensembles, namely the quark masses and respective hadron masses appearing in the action are tuned to match experimental values. Table 4.1 gives a summary of the ensembles used in this work.

As mentioned in the previous sections, we are using the isospin-3/2, 16 irrep operators to construct two-point correlators. There are four operator classes available, however, we observed in our correlator data that the class-3 operator overlaps weakly with the nucleon-like state of interest. Because all three quarks in the class-3 operators reside on the even corners of a spatial cube, the operator has vanishing couplings to the nucleon-like state in the continuum. In addition, we have not found an appreciable difference in analyses by not including them, so we only use class-2, 4, and 6 operators in this work.

We construct the two-point correlators according to (4.2). To accommodate for the presence of non-local lattice operators and the use of corner-wall sources, the ensembles are fixed to the Coulomb gauge to obtain non-vanishing results. In doing so, the overlap factors become gauge variant but the masses are still physical gauge-invariant quantities. We average over all 16 irrep components to obtain a three-by-three correlator matrix with three different classes. Each correlator is folded according to (4.13) so the finite time extent in the spectral decomposition can be ignored.

4.1.4 Analysis details

We use the `corrfitter` package [111] for analyses in this work, and all posterior errors are estimated with 1000 bootstrap samples. Since this work was the first in calculating the nucleon mass with a full set of staggered baryon operators, we employ three different analysis strategies to investigate the best approach.

The first strategy is the simultaneous fit to all $3 \times 3 = 9$ correlators within the Bayesian framework using the spectral decomposition in (4.14). One problem with this approach is the presence of near degenerate three Δ-like states in the excited state. For non-staggered simulations, the Δ baryons cannot be created by a nucleon operator because of the difference in isospins. Because the data are noisy, we have found that we are unable to resolve all three states, and instead, only two "Δ-like" states are confidently observed. Even though we call those two excited states Δ-like states, they can well be some linear combinations of three Δ-like states and/or nucleon-pion states that are incidentally well resolved by our operator basis as all those states have similar masses. But since they are all nuisance parameters in this analysis that we can marginalize over, we will refer to them as Δ-like states for simplicity.

We impose a Gaussian prior for the nucleon mass $m_N \equiv m_{+0}$ centered around the physical value of 940 MeV with a large variance of 50 MeV to account for the mass shift introduced by the lattice discretization. We similarly introduce a Gaussian prior for the mass of the first excited state in the negative parity channel m_{-0}, with a mean of 1400 MeV and a variance of 200 MeV. The identity of this state is unknown. The first negative parity nucleon resonance is $N(1520)$, however, the presence of multi-particle states cannot be excluded. The priors are large enough to accommodate a multitude of possibilities.

We impose log-normal priors on $m_{\pm i} - m_{\pm(i-1)}$ to other excited state masses to ensure $m_i \leq m_{+(i+1)}$. Because there is no evidence in the presence of three Δ-like states in the positive parity spectrum from our data, we only include two Δ-like states in this fit. We choose the prior such that the Gaussian distribution $\ln(m_{+1} - m_{+0})$ is centered at 290 MeV with a variance of 100 MeV to overlap with the 1230 MeV Δ mass observed in experiments. For the second Δ-like state, we choose a central value of 150 MeV and variance of 50 MeV for $\ln(m_{+2}-m_{+1})$ on the $a \approx 0.15$ fm ensemble. As the lattice spacing decreases, taste-breaking effects are expected to be smaller so we choose priors of 100 ± 50 and 50 ± 50 MeV priors for $a \approx 0.12$ and 0.09 fm ensembles, respectively. The identities of other excited states are even more difficult to pin down and priors of 400 ± 200 MeV are chosen for logarithmic differences in masses. For our nominal fits, we include a total of four positive parity (one nucleon-like state, two Δ-like states, and one leftover excitation) and four negative parity states. We have no knowledge of signs and magnitudes of overlap factors so we are not constraining those parameters with priors. See Tables V and XI in [2] for the exact parameters we use in Bayesian fits.

To further cross check our results from the Bayesian fits, we also apply variation methods to the correlator matrix and obtain the nucleon mass from eigenvalue fits. In this work, we are experimenting with both types of GEVPs in (4.20) and (4.23):

$$\begin{aligned} \mathbf{C}_{2\text{pt}}^{16+,0;(R_1,R_2)}(t)v_R^{(i)} &= \lambda^{(i)}\mathbf{C}_{2\text{pt}}^{16+,0;(R_1,R_2)}(t_0)v_R^{(i)}, \\ \mathbf{D}_{2\text{pt}}^{16+,0;(R_1,R_2)}(t,t_0)\widetilde{v}_R^{(i)} &= \widetilde{\lambda}^{(i)}\widetilde{v}_R^{(i)} \quad (i=0,1,2,3) \end{aligned} \tag{4.26}$$

where $\mathbf{D}_{2\text{pt}}^{16+,0;(R_1,R_2)}(t,t_0)$ is defined in (4.24), and fit $\lambda^{(0)}$ and $\widetilde{\lambda}^{(0)}$ to functions

$$\lambda^{(0)}(t, t_0 = \text{fixed}) = Ae^{-m_N t} - (-1)^t Be^{-m_- t} \tag{4.27a}$$

$$-\frac{1}{2}\ln\widetilde{\lambda}^{(0)}(t = t_0+2, t_0) = m_N + Ce^{-\widetilde{\delta M}t_0} \tag{4.27b}$$

Note that these two are separate fits. For the $\lambda^{(0)}$ fit, we are fixing the value of t_0 to be 3, 5, and 5 for $a \approx 0.15$, 0.12, and 0.09 fm, respectively, to keep t_0 approximately constants in physical units. A and B are unknown coefficients, and we expect $A+B \approx 1$ if the eigenvalues can be well described by this two-state model [105, 106]. m_N is the nucleon mass and m_-

is the negative parity excited state mass; for the $\widetilde{\lambda}^{(0)}$ fit, we instead fix $t - t_0 = 2$ and vary t_0 in the fit function. Because we expect $\widetilde{\lambda}^{(0)}(t, t_0)$ to scale as $e^{-m_N(t-t_0)}$ in the large time limit, by fixing $t - t_0 = 2$ eigenvalues should be approximately constants modulo excited state contaminations, which can be fitted away by the second term in (4.27b) with unknown parameters C and $\widetilde{\delta M}$. We observe no evidence of oscillatory contributions to $\widetilde{\lambda}^{(0)}(t, t_0)$ so only the positive parity excitation is considered here. Because of the reduced number of unknown parameters in (4.27a) and (4.27b), we are able to perform unconstrained, frequentist fits (or, equivalently, "constrained" fits with large priors) to obtain stable results without explicitly imposing priors. See Tables VI in [2] for other parameters we use in variational method analyses.

Compared to the full Bayesian fit, the variation method analyses are much easier to handle as we are not working with a three-by-three matrix of correlators. Instead, we preprocess the correlator matrix to first marginalize some excited contaminations before fitting to enhance the ground state signal. For the nucleon mass work, we are able to apply both the full Bayesian fits and variational methods and obtain consistent results. However, as fit functions become even more complicated for three-point correlators, we expect the direct fit to the correlator matrix to be even more difficult to implement as we do not have sensible priors for most parameters in the fit functions there. In that case, reducing the complexity of correlators via solving GEVPs is crucial in extracting sensible results.

4.1.5 Fit results

We present here some fit results for both the Bayesian and variational method analyses. As an example, we only show results of $a \approx 0.12$ fm ensemble – results from other ensembles are similar and can be found in [2]. Figure 4.1 shows the effective mass plots, as defined in (4.16), of the Bayesian analysis. The blue data points are raw correlator values, and we obtain the orange data points by central values of excited state exponentials from the blue data points.

In the ideal fit where excited states contaminations are completely eliminated, we expect the orange points to be constants. As we can see from figure 4.1 that the orange points are consistent with this expectation within the fit regions (data points in white regions). Deviations of orange points from constant values are obvious for small t outside the fit regions, which signal the presence of unaccounted excited states. But because of the exponential dampening, those states do not affect our nucleon estimate at larger t. The posterior estimate of the nucleon mass is 0.5952(31) on this ensemble; see Table XI in [2] for results of other nuisance parameters.

In figure 4.2, we show effective masses of $\lambda^{(0)}(t, t_0 = 5)$ as functions of $t - t_0$. Note that t_0 is fixed to five. Three sets of points are shown: the blue data points are the effective masses of the raw eigenvalues $\lambda^{(0)}(t, t_0 = 5)$ as defined in (4.16) (if we treat $\lambda^{(0)}(t, t_0 = 5)$ as correlators C); the orange data points are the effective masses of $\lambda^{(0)}(t, t_0 = 5)$ after subtracting the central value of the excited state term posterior in (4.27a); and the black data points are the smoothed effective masses of $\lambda^{(0)}(t, t_0 = 5)$, which are weighted averages of M_{eff} at adjacent timeslices

$$M_{\text{smooth}}(t) \equiv \frac{1}{4}\Big(M_{\text{eff}}(t-1) + 2M_{\text{eff}}(t) + M_{\text{eff}}(t+1)\Big) \tag{4.28}$$

Smoothing the effective mass is useful in mitigating the excited state contaminations from oscillatory contributions of negative parity states. As we can see from figure 4.2 that once effective masses are smoothed, black data points agree well with the orange data points which show the expected ground state contribution to eigenvalues. We can conclude from this that most excited state contaminations for $\lambda^{(0)}(t, t_0 = 5)$ come from the negative parity state. The posterior estimate of the nucleon mass is 0.5945(29).

In figure 4.3, we show $\widetilde{\lambda}^{(0)}(t, t_0)$ (labeled as $\widetilde{\lambda}_1$ in the figure) as a function of t_0. $t - t_0 = 2$ is fixed. The orange band is the one-sigma posterior fit to blue points. We can similarly interpret the y-axis as another type of effective masses since it approaches the nucleon mass

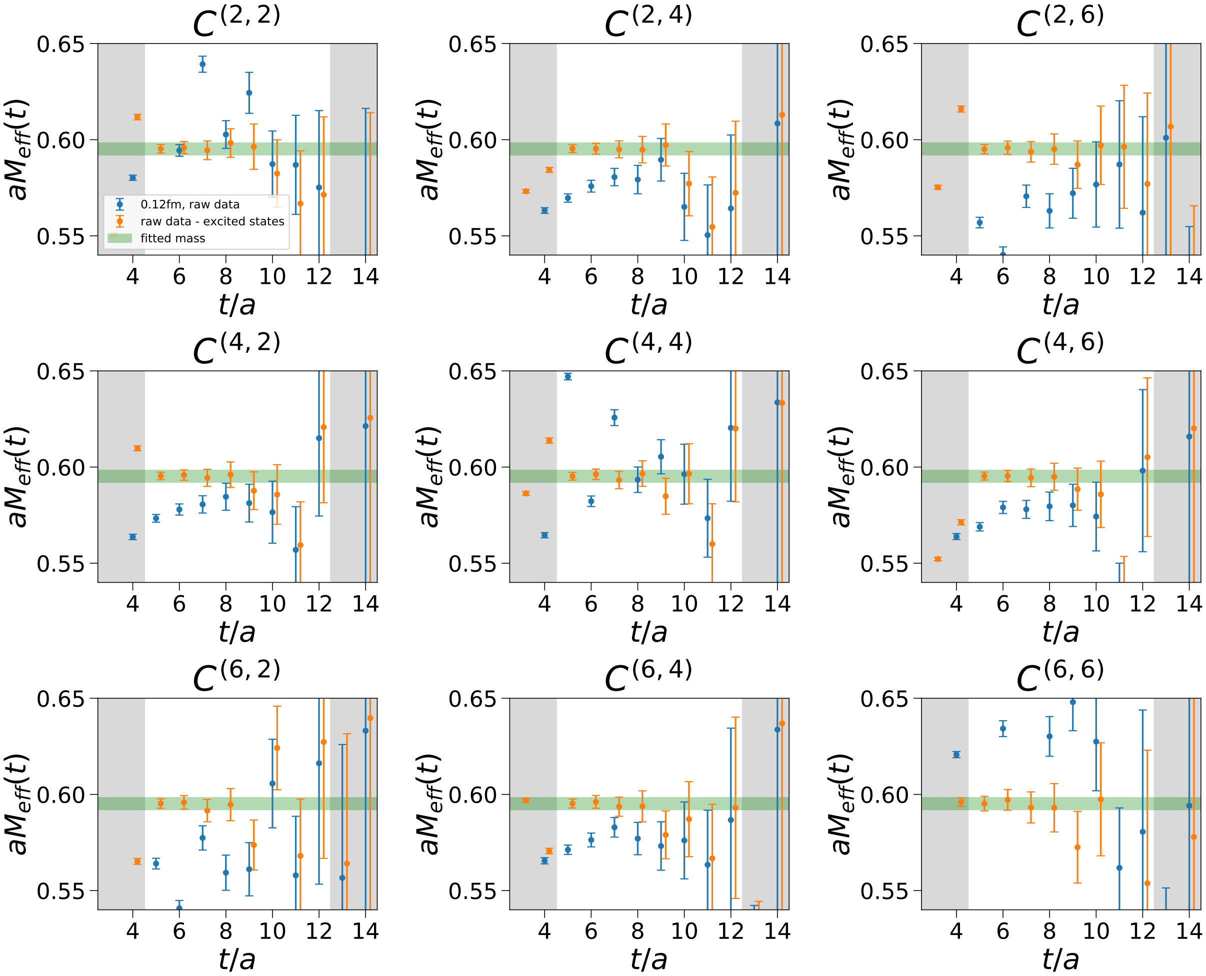

Figure 4.1: Effective mass plots of the correlator matrix constructed with isospin-3/2, 16 irrep operators for the $a \approx 0.12$ fm ensemble. $R_1, R_2 \in \{2, 4, 6\}$ appearing in $C^{(R_1,R_2)}$ denote the source/sink operator classes; the blue data points are the raw correlator data and the orange data points are results of subtracting central values of excited state exponentials from the raw correlator data; the green bands are the one-sigma estimate of the nucleon mass from the simultaneously Bayesian fit to all nine correlators using the fit model in (4.14) with four positive and four negative parity states. Data points in grey regions are excluded from the fit. This figure is reproduced from our work in [2].

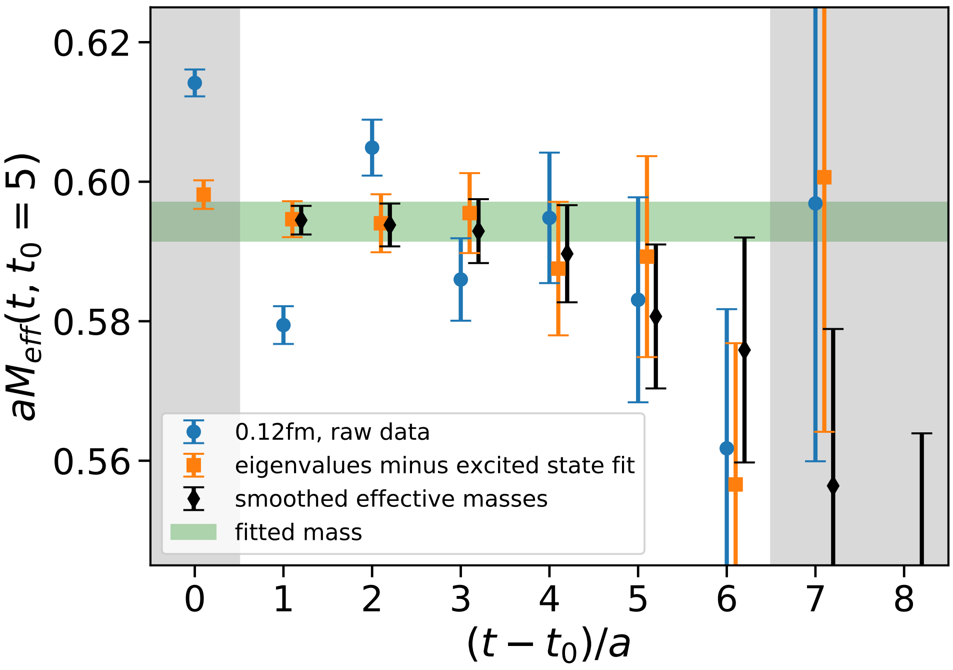

Figure 4.2: Effective masses of $\lambda^{(0)}(t, t_0 = 5)$ as functions of $t - t_0$ where $t_0 = 5$ for the $a \approx 0.12$ fm ensemble. The orange data points are the traditional effect masses of $\lambda^{(0)}(t, t_0 = 5)$, the orange data points are effective masses of $\lambda^{(0)}(t, t_0 = 5)$ after subtracting the excited state posterior contribution, and the black data points are the smoothed effective masses as defined in 4.28. Only data points in the white region are included in the fit, and the green band is the one-sigma posterior estimate of the nucleon mass using the fit model in (4.27a). This figure is reproduced from our work in [2].

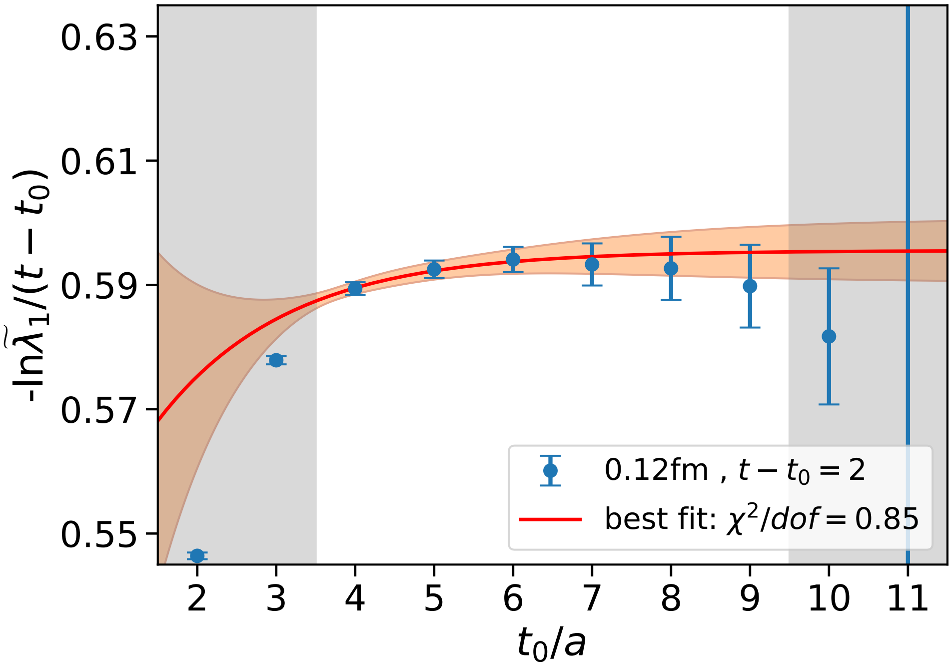

Figure 4.3: $\widetilde{\lambda}^{(0)}(t,t_0)$ (labeled as $\widetilde{\lambda}_1$ in the figure) as a function of t_0. $t-t_0$ is fixed to 2. The orange band shows the one-sigma posterior estimate to the blue points using the fit model in (4.27b). In the large t_0 limit, data points should converge to a constant value equal to the nucleon mass m_N. This figure is reproduced from our work in [2].

in the large t_0 limit. As we can see from the plot that there are no oscillating contribution to eigenvalues, so a two-state model of (4.27b) is sufficient in parameterizing data points within the white region in which data points are included in the fit. The final nucleon posterior estimate is 0.5945(48).

Regardless of the types of fits, there are three major sources of systematic errors that we consider here: fit errors, light-quark mistuning errors, and finite volume corrections. Fit errors come from the variations of the nucleon mass posteriors as we vary parameters in fits. The most important parameter of all is t_{min}, the minimum t (or t_0 for $\widetilde{\lambda}^{(0)}$, we will make no distinctions here) in which we include data points in fits, as the data become more precise at lower t but excited state contaminations become more severe; on the other hand, the data become noisier at higher t but excited states are exponentially suppressed. Any leftover

Table 4.2: Nucleon mass estimates from three types of fits for all ensembles. The first errors are statistical and the second systematic from residual excited state contaminations (see text for details). For estimates on the $a \approx 0.15$ fm ensemble, there is an additional 0(5) MeV systematic error that needs to be added on top of those two errors to account for the finite volume correction; and for estimates on the $a \approx 0.09$ fm, there is an addition 7(7) MeV error that needs to be added on top of those two to account for the light-quark mistuning; see [2] for more details on origins of those numbers.

$a \approx$ (fm)	$\widetilde{\lambda}^{(0)}$ fit	$\lambda^{(0)}$ fit	Bayesian fit
0.15	0.7555(22)(59)	0.7562(25)(9)	0.7579(36)(48)
0.12	0.5946(48)(22)	0.5945(29)(13)	0.5952(31)(1)
0.09	0.4295(26)(8)	0.4307(34)(2)	0.4308(31)(14)

excited state contaminations manifest as variations in nucleon mass estimates as we vary t_{min} while holding other parameters constant. To access the size of this systematic error, let t_{nom} be the t_{min} of the nominal fit. We perform another fit at $t_{\text{min}} = t_{\text{exct.}} < t_{\text{nom}}$ and evaluate the difference in central values of nucleon mass estimates from those two fits. The result is an estimate of residual excited state contaminations in the nucleon mass posterior and it is added in quadrature to the statistical error. Typically, we choose $t_{\text{exct.}}$ to be one or two lattice units smaller than t_{min} depending on ensembles and types of fits. Alternatively, one can combine results from various t_{min} in either the frequentist or Bayesian framework; see, for examples, [94, 112]. We summarize the nucleon posterior results, including both statistical and systematic errors, in Table 4.2. Despite differences in marginalizing excited state contributions, we have found that results from three types of fits are consistent with one another in all ensembles. This means they are all successful in eliminating excited state contaminations from our nucleon mass estimates.

4.1.6 Continuum extrapolation

Lattice discretization systematics can be eliminated by extrapolating our results to the continuum using the functional form

$$m_N(a) = m_{N,\text{phy}}\Big(1 + o_2(\Lambda a)^2 + o_4(\Lambda a)^4\Big) \tag{4.29}$$

where $m_{N,\text{phy}}$ is the continuum nucleon mass. We choose the characteristic energy scale to be $\Lambda = 500$ MeV, which is roughly consistent with Λ_{QCD}. o_2 and o_4 are two dimensionless parameters of order one. Because there is a remnant chiral symmetry for the staggered action, discretization errors in odd powers of a^2 cannot appear in the action [113], so the leading errors in the nucleon mass is $\mathcal{O}(a^2)$ and $\mathcal{O}(a^4)$. We are using three data points of nucleon masses to infer three unknown parameter o_2, o_4, and $m_{N,\text{phy}}$, so the system of equations can be solved exactly, but the solution will be unphysical (o_4 can be unphysically large when we expect it to be of order one for example) due to overfitting of data. To avoid this issue, we impose Gaussian priors of 940(50) MeV on $m_{N,\text{phy}}$ based on its PDG value and 0(1) on o_4; we do not constrain o_2. Figure 4.4 shows the continuum extrapolation of nucleon masses using results from $\widetilde{\lambda}^{(0)}$ fits that include all sources of systematic errors in Table 4.2. The final estimate is

$$m_{N,\text{phy}} = 964(16)\text{ MeV} = 964(8)_{\text{stat}}(5)_{\text{fit}}(4)_a(3)_{\text{FV}}(8)_{\text{mis}}\text{ MeV} \tag{4.30}$$

where stats., fit, a, FV, and mis are statistical errors, fit errors from residual excited state contaminations, lattice spacing errors, finite volume corrections, and light-quark mistuning errors, respectively. Our nucleon estimate is 1.6 sigma higher than the experimental value of 940 MeV, which seems to be driven mostly by the upward fluctuations of our $a \approx 0.09$ fm results. Note that this is also the ensemble in which the light-quark masses are poorly tuned. We are currently adding one more measurement with $a \approx 0.06$ fm at physical quark masses

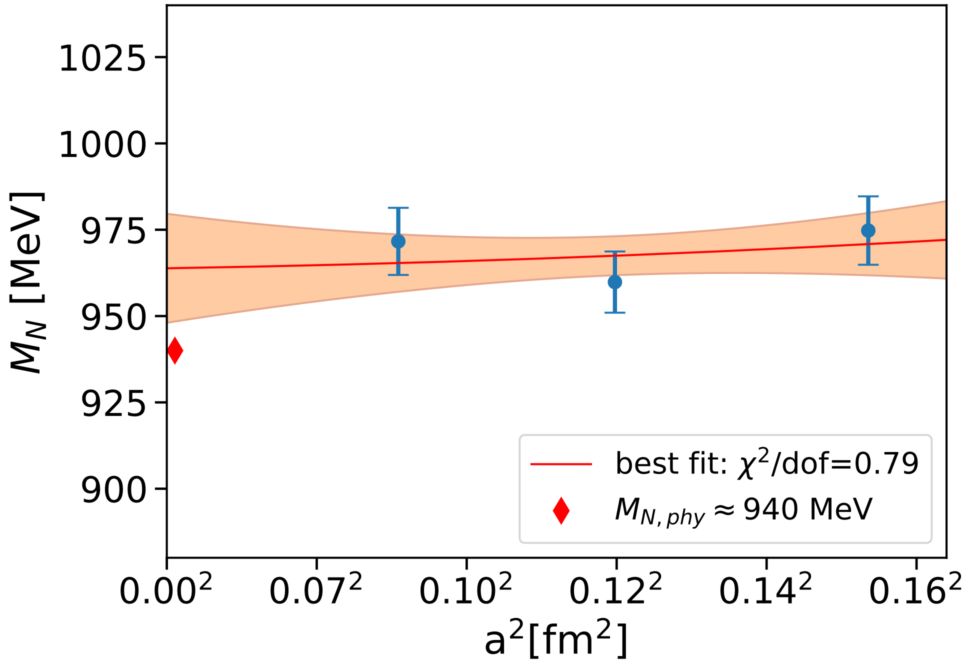

Figure 4.4: Continuum extrapolation of nucleon masses using results from $\widetilde{\lambda}^{(0)}$ fits that include all sources of systematic errors in Table 4.2. The orange band shows the one-sigma estimate with (4.29). This figure is reproduced from our work in [2].

to hopefully better control the continuum extrapolation.

Now that we have demonstrated how to use staggered fermions for both valence and sea quarks to compute two-point functions. In the next section, we will turn our attention to three-point functions and show how to extract nucleon vector and axial-vector charge with the same simulation setup.

4.2 Nucleon matrix elements with highly improved staggered quarks

In the continuum QCD language with Dirac spinors, the nucleon matrix element we are going to compute is:

$$\langle N\big|\big(\overline{u}\Gamma_J u - \overline{d}\Gamma d\big)\big|N\rangle = g_J \overline{u}_N \Gamma_J u \tag{4.31}$$

where $|N\rangle$ is the nucleon state, u/d ($\overline{u}/\overline{d}$) is the up/down-quark spinor, and u_N ($\overline{u}_N$) is the nucleon spinor. Only isovector current operators are used which correspond to charged current interactions; simulating isoscalar current operators, which correspond to neutral current interactions, are costly due to the presence of disconnected diagrams so we will not consider them in this work.

In this work, we compute both the temporal component of the vector charge, $\Gamma_V \equiv \gamma_4$, and the z-component of the axial-vector current, $\Gamma_A \equiv \gamma_3\gamma_5$. Because the vector current is conserved, $g_V = 1$. On the other hand, the nucleon axial charge g_A can be measured precisely from neutron beta decays and the latest experimental value is $g_A = 1.2756(13)$ [46]. Since this is the first attempt to compute nucleon matrix elements with staggered valence quarks, recovering the conserved vector charge is an important check to the lattice methodology we have developed in previous chapters, ensuring there are no surprising features that we missed. We also compute the nucleon axial charge, or the nucleon axial form factor at zero momentum transfer, to serve as a stepping stone towards a full form factor simulation.

4.2.1 Staggered baryon three-point correlator constructions

Two- and three-point correlators are both needed to extract matrix elements. We use the same set of creation and annihilation operators – isospin-3/2, 16 irrep operators with classes 2, 3, 4, and 6 – as the nucleon mass study in the previous section (we include class-3 operator in this study). We follow the same two-point correlators constructs present in Section 4.1.1 to obtain $C_{2\text{pt}}^{16+,0;(R_1,R_2)}(t)$, $R_1, R_2 \in \{2,3,4,6\}$ which have a spectral decomposition of (4.14) after the folding procedure in (4.13). One only component of the 16 irrep is considered here because they are all identical in the ensemble average according to (4.3).

For three-point correlators, we have to decide on the tastes of quark bilinears to use as current operators; the complete set is listed in Table 2.2. To maximize signal-to-noise ratios of correlators, we use zero-momentum local current operators [79]

$$\begin{aligned} J_V(\tau) &\equiv \overline{U}(\gamma_4 \otimes \xi_4)U - \overline{D}(\gamma_4 \otimes \xi_4)D \\ &\equiv \sum_{\vec{x}} S_V(\vec{x})\big(\overline{\chi}_u(\vec{x},\tau)\chi_u(\vec{x},\tau) - \overline{\chi}_d(\vec{x},\tau)\chi_d(\vec{x},\tau)\big) \end{aligned} \tag{4.32a}$$

$$\begin{aligned} J_A(\tau) &\equiv \overline{U}(\gamma_3\gamma_5 \otimes \xi_3\xi_5)U - \overline{D}(\gamma_3\gamma_5 \otimes \xi_3\xi_5)D \\ &\equiv \sum_{\vec{x}} S_A(\vec{x})\big(\overline{\chi}_u(\vec{x},\tau)\chi_u(\vec{x},\tau) - \overline{\chi}_d(\vec{x},\tau)\chi_d(\vec{x},\tau)\big) \end{aligned} \tag{4.32b}$$

where

$$\begin{aligned} S_V(\vec{x}) &= (-1)^{x_1+x_2+x_3} \\ S_A(\vec{x}) &= (-1)^{x_3} \end{aligned} \tag{4.33}$$

Here we use a similar notations as Sections 2.3.3 and 2.3.4 to denote our lattice operators V and A: $U/\overline{U}$ and $D/\overline{D}$ are vectors of continuum Dirac spinors in the taste space for up and down quarks; γ_i is a gamma matrix acting in the spinor space and ξ_i is a gamma matrix acting in the taste space; $\chi_u/\overline{\chi}_u$ and $\chi_d/\overline{\chi}_d$ are one-component staggered fermion field of up and down quarks. We are using the continuum notation to denote our lattice operators as the mapping is unique for quark bilinears. All operators are in the isovector combinations. Note that if the spin and taste gamma matrices are identical ($\gamma_4 \otimes \xi_4$ and $\gamma_3\gamma_5 \otimes \xi_3\xi_5$ in this case), the quark and antiquark fields reside on the same lattice sites which make them local operators. Operators of other tastes are always non-local operators in which gauge links are needed to connect quark and antiquark fields, which make them more susceptible to gauge link fluctuations from Monte-Carlo samplings. This translates into noisier estimators of nucleon matrix elements that we avoid here.

For each current operator, we can construct 16 three-point correlators to get

$$\begin{aligned} C_{\text{3pt,V}}^{16\pm,D;(R_1,R_2)}(t,\tau) &\equiv \left\langle O_{[3/2,3/2]_F}^{16\pm,D;\text{cls}R_1}(t)\ J_V(\tau)\ \overline{O}_{[3/2,3/2]_F}^{16\pm,D;\text{cls}R_2}(0)\right\rangle, \\ C_{\text{3pt,A}}^{16\pm,D;(R_1,R_2)}(t,\tau) &\equiv \left\langle O_{[3/2,3/2]_F}^{16\pm,D;\text{cls}R_1}(t)\ J_A(\tau)\ \overline{O}_{[3/2,3/2]_F}^{16\pm,D;\text{cls}R_2}(0)\right\rangle \end{aligned} \tag{4.34}$$

where we use the same notations as (4.1) and (4.2). Note the only way to construct non-vanishing zero momentum, three-point correlator given local current operators is by imposing both the source and sink operators reside on the same spatial cube sites, which in this case is D. This can be proven easily by considering transformation properties of correlators. A general correlator is a reducible representation of the lattice symmetry group GTS which can be written as a direct sum of many irreps. By the Great orthogonality theorem, we can show that the only non-vanishing component within the direct sum is the trivial irrep, therefore, a correlator is zero if it does not contain the trivial irrep as one of its irreducible components.

It is a two-step process to find irreducible components of a three-point correlator:

1. Tensor product source and sink operators and find its irreducible components.[2]

2. Tensor product irrep components from the previous step with the current operators and find its irreducible components.

If the results of the second step contain the trivial irrep, we are certain the correlator we construct does not violate the lattice symmetry and can be non-zero. When we tensor product two irrep components in the second step, the trivial irrep appears if i) two irreps

---

[2] We can perform this step first because current operators commute with source/sink operators.

are identical and ii) we are taking the trace of two irreps, namely, multiplying the same irrep components from two irreps. The condition i) is certainly satisfied in our case as the tensor product of 16 irreps in which source/sink operators transform contain all irreps of current operators that we work with, so we can always tensor product the current operator with the same irrep in which it transforms; on the other hand, the condition ii) implies that the three-point correlator is non-vanishing if the relative displacement in spatial cube sites between source and sink operator is the same as the relative displacement between the quark and antiquark field for the current operator. For example, consider the correlator

$$\left\langle O^{16\pm,D+\hat{x};\mathrm{cls}R_1}_{[3/2,3/2]_F}(t)\; J_V(\tau)\; \overline{O}^{16\pm,D;\mathrm{cls}R_2}_{[3/2,3/2]_F}(0)\right\rangle \tag{4.35}$$

In this case, the current operator is local so the relative displacement between the quark and antiquark is zero. However, the source operator resides on the D spatial cube site, whereas the sink operator resides on the $D+\hat{x}$ (modulo two) site. This means that by condition ii) that the correlator is zero in the ensemble average. This can be proven easily by applying the spatial inversion operator I_s and show that the correlator is equal to the negative of itself. Correlators in (4.34), barring non-group-theoretical reasons, is non-vanishing since the source and sink operators reside on the same spatial cube sites and the current operators are local. Intuitively, we can think of the product of the source and sink operators forms a quark bilinear with a certain taste, and the three-point correlator is reduced to a mesonic two-point correlator. In this case, it is obvious that to ensure the two-point correlator is non-vanishing we need to have the same mesonic operator at both source and sink, which translates into conditions i) and ii) that we mentioned. This procedure can be generalized to n-point correlators constructed from operators at zero momenta.

To simulate (4.34) on a computer, we can again expand expressions using the Wick theorem and write them as products of propagators, which can be computed from solving lattice Dirac equations. In this work, we used the sequential source method to compute propagators for three-point functions; see [51] for a pedagogical introduction to the method. The basic idea is that we use propagators from two-point correlators as sources for the Dirac equation to obtain the so-called sequential propagators. Products of sequential and non-sequential propagators then form three-point correlators in (4.35).

4.2.2 A numerical check to the continuum relation

For two-point functions, we can reduce the number of independent correlators from 16 to one according to (4.3) which can be derived by applying lattice symmetries. Such relations for three-point correlators are

$$\begin{aligned} C_{\rm 3pt,V}^{16\pm,0;(R_1,R_2)}(t,\tau) &= S_V(D) C_{\rm 3pt,V}^{16\pm,D;(R_1,R_2)}(t,\tau), \\ C_{\rm 3pt,A}^{16\pm,D;(R_1,R_2)}(t,\tau) &= S_A(D) C_{\rm 3pt,A}^{16\pm,D;(R_1,R_2)}(t,\tau), \\ C_{\rm 3pt,V}^{16\mp,D;(R_1,R_2)}(t,\tau) &= S_V(D) C_{\rm 3pt,V}^{16\pm,D;(R_1,R_2)}(t,\tau) \end{aligned} \tag{4.36}$$

where $S_V(D)$ and $S_A(D)$ phases are defined in (4.33) (if we convert use the vector representation of B as defined in (3.9)). Relations for vector correlators are almost identical to that of two-point correlators – all 16 correlators are identical in the ensemble average up to some phases. For axial-vector correlators, two sets of eight components are identical, up to phases, in the ensemble average but there are no constant factors that relate eight components of $16-$ to eight components of $16+$. This is verified in our simulations.

In general, we cannot find an exact relation that relates $16-$ to $16+$ components and the vector correlator is one of the few exceptions. However, we can find such relations in the continuum and large time limits and derive factors of proportionality using the Wigner-Eckart theorem in Chapter 2. In the large t and τ limit where excited states can be ignored, the axial-vector correlators have spectral decompositions of

$$C_{\rm 3pt,A}^{16\pm,D;(R_1,R_2)}(t,\tau) \sim K \times M_{\rm A,latt} \times e^{-m_N t} \tag{4.37}$$

where

$$M^{16\pm,D}_{\text{A,latt}} \equiv \left\langle \left[\frac{3}{2},\frac{3}{2}\right]_F \left[16\pm,D\right]_{\text{GTS}} \right| J_A \left| \left[\frac{3}{2},\frac{3}{2}\right]_F \left[16\pm,D\right]_{\text{GTS}} \right\rangle \tag{4.38}$$

is the lattice matrix element with notations defined in (3.23). K is the product of overlap factors that depend on R_1, R_2, and the irrep but not on specific components. Since all eight components are identical given a choice of 16±, we focus only on the $D = 0$ case. The ratio of 16± three-point correlators in large time limits is simply equal to the ratio of matrix elements

$$\frac{C^{16-,0;(R_1,R_2)}_{\text{3pt,A}}}{C^{16+,0;(R_1,R_2)}_{\text{3pt,A}}} \sim \frac{M^{16-,0}_{\text{A,latt}}}{M^{16+,0}_{\text{A,latt}}} \tag{4.39}$$

that is independent of t and τ.

In the continuum limit, we can use Table 3.2 to look up the quantum numbers of nucleon-like states, and the current operator simply transforms as a quark bilinear with spin-taste of $\gamma_3\gamma_5 \otimes \xi_3\xi_5$. Matrix elements then become

$$M^{16\pm,0}_{\text{A,latt}} \to M^{16\pm,0}_{\text{A,cont}} = \left\langle 16\pm,0 \middle| \overline{U}(\gamma_3\gamma_5 \otimes \xi_3\xi_5)U - \overline{D}(\gamma_3\gamma_5 \otimes \xi_3\xi_5)D \middle| 16\pm,0 \right\rangle \tag{4.40}$$

where $M^{16\pm,0}_{\mathrm{A,cont}}$ are corresponding continuum matrix elements and

$$\left|\left[\frac{3}{2},\frac{3}{2}\right]_F\left[16-,0\right]_{\mathrm{GTS}}\right\rangle \to \left|16-,0\right\rangle \equiv \sqrt{\frac{1}{2}}\left|\left[\frac{1}{2},\frac{1}{2}\right]_S\left[\frac{3}{2},\frac{3}{2}\right]_F\left[\frac{3}{2},-\frac{1}{2}\right]_{\mathbb{Q}_8}\left[\frac{1}{2},\frac{1}{2}\right]_{D_4}\right\rangle + \sqrt{\frac{1}{2}}\left|\left[\frac{1}{2},-\frac{1}{2}\right]_S\left[\frac{3}{2},\frac{3}{2}\right]_F\left[\frac{3}{2},\frac{1}{2}\right]_{\mathbb{Q}_8}\left[\frac{1}{2},\frac{1}{2}\right]_{D_4}\right\rangle, \tag{4.41a}$$

$$\left|\left[\frac{3}{2},\frac{3}{2}\right]_F\left[16+,0\right]_{\mathrm{GTS}}\right\rangle \to \left|16+,0\right\rangle \equiv \sqrt{\frac{1}{2}}\left|\left[\frac{1}{2},\frac{1}{2}\right]_S\left[\frac{3}{2},\frac{3}{2}\right]_F\left[\frac{3}{2},\frac{3}{2}\right]_{\mathbb{Q}_8}\left[\frac{1}{2},\frac{1}{2}\right]_{D_4}\right\rangle + \sqrt{\frac{1}{2}}\left|\left[\frac{1}{2},-\frac{1}{2}\right]_S\left[\frac{3}{2},\frac{3}{2}\right]_F\left[\frac{3}{2},-\frac{3}{2}\right]_{\mathbb{Q}_8}\left[\frac{1}{2},\frac{1}{2}\right]_{D_4}\right\rangle \tag{4.41b}$$

are continuum nucleon-like states. Arrow indicate going from lattice to the continuum limit. The continuum quark bilinear transforms as a tensor operator

$$\overline{U}\xi_3\xi_5 U - \overline{D}\xi_3\xi_5 D = 2\sqrt{2}\mathcal{T}^{[1,0]_{\mathbb{Q}_8}[1,0]_{D_4}}_{[1,0]_S[1,0]_F} \tag{4.42}$$

This is almost the same expression as (2.80), except we replace the notation of taste quantum numbers from $[\cdot,\cdot]_S$ and $[\cdot,\cdot]_T$ to $[\cdot,\cdot]_{\mathbb{Q}_8}$ and $[\cdot,\cdot]_{D_4}$, and use the $[\cdot,\cdot]_S$ subscript to specify the additional spin quantum number. We see that (4.41) and (4.41b) have different quantum numbers in the spin and $\mathbb{Q}_8$ groups, so we can apply the Wigner-Eckart theorem of SU(2) separately to both groups and get

$$M^{16-,0}_{\mathrm{A,cont}} = -3M^{16+,0}_{\mathrm{A,cont}} \tag{4.43}$$

We have concluded in (2.81) the relationship between physical and staggered matrix elements.

Putting these together and we have

$$g_A = M^{16-,0}_{\mathrm{A,cont}} = -3M^{16+,0}_{\mathrm{A,cont}} \tag{4.44}$$

where g_A is the nucleon axial charge. We can carry out similar analyses for vector correlators and conclude that

$$g_V = -M^{16-,0}_{\mathrm{V,cont}} = -M^{16+,0}_{\mathrm{V,cont}} \tag{4.45}$$

(4.43) are continuum relations that are broken by the lattice discretization. Nevertheless, the symmetry breaking effect is small with an improved action, and we expect to see at large t and τ that

$$\frac{C^{16-,0;(R_1,R_2)}_{\mathrm{3pt,A}}}{C^{16+,0;(R_1,R_2)}_{\mathrm{3pt,A}}} \sim \frac{M^{16-,0}_{\mathrm{A,latt}}}{M^{16+,0}_{\mathrm{A,latt}}} \approx \frac{M^{16-,0}_{\mathrm{A,cont}}}{M^{16+,0}_{\mathrm{A,cont}}} = -3 \tag{4.46}$$

We show this ratio as a function of t and τ in figure. 4.5. Three-point correlators are optimized via the variational method, weighted averaging, and quark smearing to reduce both positive and negative parity excited state contaminations, so the large time behavior can be reached earlier – they will be described in details in the next section. As the result, correlators from different classes are linearly combined to give a single correlator we see here. Optimizing operations do not affect the group theory discussion we had, and we can see from the figure that at large t and τ, the ratio converges to -3 despite being an approximate relation on the lattice. A similar figure can be made for vector correlators and we observe that the ratio converges to one at all t and τ to much higher precision. This is because the relation for vector correlators is an exact one as we pointed out in (4.36).

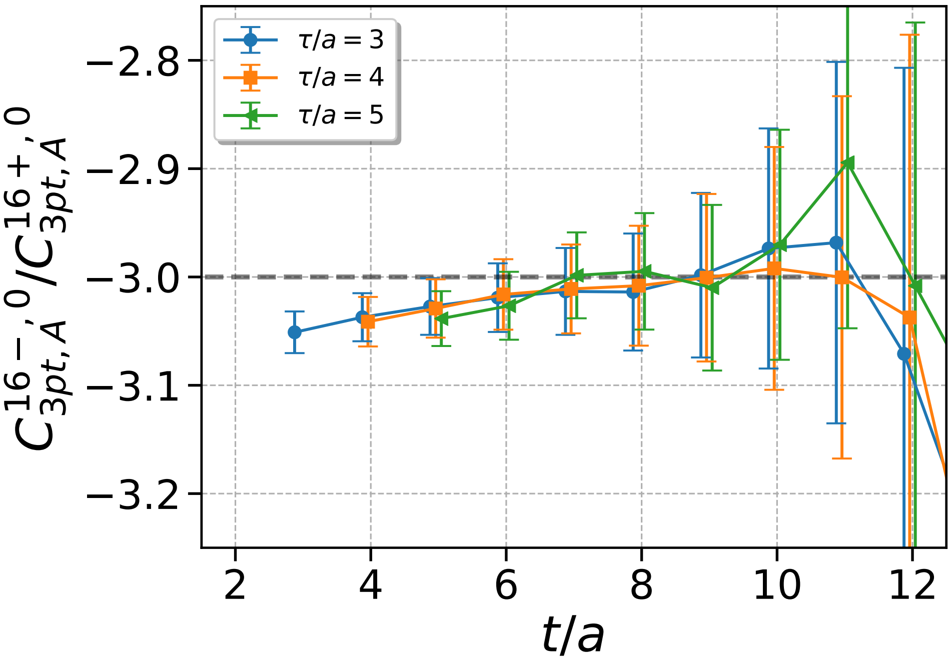

Figure 4.5: The Ratio of optimized axial-vector correlators, defined in (4.46), as a function of the source-sink separation t and current insertion time τ. In large t, τ, and continuum limits, the ratio converges to the group-theoretical factor of -3, which is shown as the grey, dashed line. Data correspond to Gr6.0N70 correlators as defined in Section 4.2.4. This figure is reproduced from our work in [3].

Based on relations in (4.44) and (4.45), we construct correlators

$$\begin{aligned} C^{16,0;(R_1,R_2)}_{\text{3pt,V}}(t,\tau) &\equiv -C^{16+,0;(R_1,R_2)}_{\text{3pt,V}}(t,\tau) - C^{16-,0;(R_1,R_2)}_{\text{3pt,V}}(t,\tau) \\ C^{16,0;(R_1,R_2)}_{\text{3pt,A}}(t,\tau) &\equiv -3C^{16+,0;(R_1,R_2)}_{\text{3pt,A}}(t,\tau) + C^{16-,0;(R_1,R_2)}_{\text{3pt,A}}(t,\tau) \end{aligned} \tag{4.47}$$

that will be used in subsequent analyses. In the large t and τ limits,

$$\begin{aligned} \frac{C^{16,0;(R_1,R_2)}_{\text{3pt,V}}(t,\tau)}{C^{16+,0;(R_1,R_2)}_{\text{2pt}}(t)} &\sim \widetilde{g}_V \\ \frac{C^{16,0;(R_1,R_2)}_{\text{3pt,A}}(t,\tau)}{C^{16+,0;(R_1,R_2)}_{\text{2pt}}(t)} &\sim \widetilde{g}_A \end{aligned} \tag{4.48}$$

$\widetilde{g}_V$ and $\widetilde{g}_A$ are lattice bare vector and axial charges. Once renormalized – local current operators are not conserved – they will converge to the continuum g_V and g_A. We will discuss renormalizations in the next section. We also compute other correlator components and average them together using (4.36) to increase statistics.

4.2.3 Renormalizing nucleon matrix elements

In QCD, vector and axial-vector matrix elements do not need renormalizations because the currents are (partially) conserved. In the staggered action, the remnant chiral symmetry allows for the existence of (partially) conserved lattice currents, which again, do not need to be renormalized. However, those currents are multi-link operators that are noisy to simulate. In practice, therefore, we usually use non-conserved local currents that are less prone to gauge noises but require calculating renormalization constants Z_V and Z_A.

Fortunately, the local vector and axial-vector currents we use in this work are easy to renormalize *non-perturbatively* for the staggered action. For the vector current, we can simply impose that $Z_V\widetilde{g}_V = 1$. Z_V can be interpreted as the ratio between the conserved vector matrix element, which is equal to identity if bra and ket states consist of identical hadrons at zero momenta, and the local vector matrix element [114]. This simply gives $Z_V = 1/\widetilde{g}_V$. We can of course obtain $\widetilde{g}_V$ from nucleon matrix elements in (4.48), but doing so would defeat our original purpose of cross checking the validity of vector matrix elements since we are imposing them to be equal to one. Instead, we can calculate $\widetilde{g}_V$ from a matrix element of two identical mesons to calculate Z_V, and verify that $Z_V\widetilde{g}_V = 1$ when we calculate $\widetilde{g}_V$ from nucleon matrix elements. This has the additional benefit of being a simpler calculation to perform because meson matrix elements are less noisy. Using this method we obtain $Z_V = 0.991(1)$ [3]. Also, see [114] for alternative methods to renormalize vector currents in the staggered action.

Usually one has to calculate renormalization factors of Z_V and Z_A separately on the lattice because chiral symmetry is broken (see, for example, [45]). But if one uses an action that preserves parts of the chiral symmetry, such as domain-wall (see, for example, [94]) and staggered actions, $Z_V \approx Z_A$ up to small discretization and non-zero light-quark masses errors [114], which can be ignored given our current statistics. So we simply impose $Z_V = Z_A = 0.991(1)$ in this work to renormalize both vector and axial-vector matrix elements.

4.2.4 Spectral decomposition of staggered baryon three-point correlators

(4.47) have spectral decompositions of

$$\begin{aligned} C^{16,0;(R_1,R_2)}_{\mathrm{3pt,V}}(t,\tau) = &\sum_{i,j=0}^{n_+} a^{(R_1)}_{+j} V_{+j,+i} b^{(R_2)}_{+i} e^{-m_{+i}\tau} e^{-m_{+j}(t-\tau)} + \\ &(-1)^t \sum_{i,j=0}^{n_-} a^{(R_1)}_{-j} V_{-j,-i} b^{(R_2)}_{-i} e^{-m_{-i}\tau} e^{-m_{-j}(t-\tau)} + \\ &(-1)^\tau \sum_{i=0}^{n_+}\sum_{j=0}^{n_-} a^{(R_1)}_{+i} V_{+i,-j} b^{(R_2)}_{-j} e^{-m_{-j}\tau} e^{-m_{+i}(t-\tau)} + \\ &(-1)^{t-\tau} \sum_{i=0}^{n_+}\sum_{j=0}^{n_-} a^{(R_1)}_{-j} V_{-j,+i} b^{(R_2)}_{+i} e^{-m_{+i}\tau} e^{-m_{-j}(t-\tau)} \end{aligned} \tag{4.49}$$

The expression for axial-vector three-point correlators can be obtained by simply replacing V's with A's. The notation here is identical to that of (4.12): $m_{+i} \leq m_{+(i+1)}$ and $m_{+j} \leq m_{-(j+1)}$ are masses of positive and negative parity states; $b_{\pm k}^{(R_2)}$ and $a_{\pm k}^{(R_1)}$ are source and sink overlap factors for the k-th state in the $\pm$ parity channel; n_+ and n_- are the total number of positive and negative parity states in the spectrum; $V_{\pm k, \pm l}$ (or $A_{\pm k, \pm l}$ for axial-vector matrix elements) are transitional matrix elements from the $\pm l$-th state to the $\pm k$-th state.

$V_{+0,+0} = \widetilde{g}_V$ and $A_{+0,+0} = \widetilde{g}_A$ are the bare charges we wish to extract, which can be achieved by simultaneously fitting two- and three-point correlators using (4.14) and (4.49). A direct fit to matrices of two- and three-point correlators however is difficult in practice because (4.49) allows cross talking between different excited states in both channels, which results in many more fit terms and nuisance parameters compared to two-point correlators. Unless we have good prior knowledge on those parameters, which we don't for most cases, posterior estimates on nucleon masses and charges will either have large error bars or be heavily contaminated by residual excited state contributions. Suppressing excited state terms from (4.49) before fitting is therefore of paramount importance here. In this work, we sequentially apply three different techniques in the preprocessing pipeline to achieve this: quark smearings, weighted time averaging, and the variational method. Quark smearings and the variational methods are standard lattice QCD techniques that are designed to suppress excited state contaminations from both parity states, whereas the weighted time averaging is unique to staggered baryon correlators designed to suppress overlap factors from negative parity states. The end results of those three procedures will be two three-point correlators, $C_{\text{3pt,V}}^{16,0;\sigma}(t,\tau)$ and $C_{\text{3pt,A}}^{16,0;\sigma}(t,\tau)$, and one two-point correlator, $C_{\text{2pt}}^{16+,0;\sigma}(t)$, which will be referred to as optimized correlators. $\sigma \in \{0.2, 0.6\}$ subscripts denote specific quark smearing parameters we use. Here we introduce those three techniques that are applied in succession to our raw data:

Quark smearings

This step differs from the rest in that quark smearings are applied to individual quarks in the simulation time, whereas the other two methods act directly onto correlators. The idea behind smearing is simple (see [51] for a pedagogical introduction). Instead of constructing a hadron interpolating operator at either the source or sink from local quark fields, we construct it from non-local quark fields averaged (smeared) over a large number of field sites within a characteristic radius of say r. We then expect overlap factors of a state with mass $m \gtrsim 1/r$ to be strongly reduced. As long as the smearing procedure commutes with the lattice symmetry group, such operation does not affect the spectra of interpolator operators.

The particular type of the quark smearing we are using is called the Wüppertal smearing [115, 116] which is defined via an iterative procedure operating on a staggered quark field $\chi(\vec{n},t)$ as

$$\chi^{(i)}(\vec{n},t) = \Big(1 + \frac{3\sigma^2}{32a^2N}\Delta\Big)\chi^{(i-1)}(\vec{n},t) \tag{4.50}$$

where

$$\begin{aligned} &\chi^{(0)}(\vec{x},t) = \chi(\vec{n},t), \\ &\Delta\chi(\vec{n},t) = -6\chi(\vec{n},t) + \sum_{i=1}^{3}\big\{\chi(n_i+2,t) + \chi(n_i-2,t)\big\} \end{aligned} \tag{4.51}$$

Δ is the discretized Laplacian, i counts the iteration number out of N total iterations. For large N, the wavefunction of $\chi^{(N)}$ converges to a Gaussian with the root-mean-squared (rms) of σ. In this work, we only smear quarks at the sink[3] with rms radii of 0.2 and 0.6 fm and total iteration numbers of 30 and 70, respectively. Correlators with those smeared quarks at the sink are labeled as Gr2.0N30 and Gr6.0N70. Smearing at the sink incurs

---

[3] Quarks at the source are already smeared by the use of corner-wall sources.

almost no costs compared to solving quark propagators so it is almost always beneficial to include it, however, excessive smearing can cause degrading signal-to-noise ratios. By applying two different smearings with small and large rms radii then fitting those correlators simultaneously, we aim to take advantage of suppressed excited state contaminations while retaining reasonable data statistics.

Weighted time averaging

The second step in the preprocessing pipeline is to suppress negative parity contributions by taking weighted averages of correlators in the time direction. Let $C_{\text{2pt}}(t)$ and $C_{\text{3pt}}(t,\tau)$ be some generic two- and three-point staggered baryon correlators with spectral decompositions of

$$\begin{aligned} C_{\text{2pt}}(t) &= a_{+0}b_{+0} + (-1)^t a_{-0}b_{-0}e^{-m_0 t} + \cdots , \\ C_{\text{3pt}}(t,\tau) &= a_{+0}M_{+0,+0}b_{+0}e^{-m_{+0}t} + \\ &\quad (-1)^t a_{-0}M_{-0,-0}b_{-0}e^{-m_{-0}t} + \\ &\quad (-1)^\tau a_{+0}M_{+0,-0}b_{-0}e^{-m_{-0}\tau}e^{-m_{+0}(t-\tau)} + \\ &\quad (-1)^{t-\tau} a_{-0}M_{-0,+0}e^{-m_{-0}\tau}e^{-m_{-0}(t-\tau)} + \cdots \end{aligned} \tag{4.52}$$

where $m_{\pm 0}$ are the ground state masses in positive and negative parity channels, a's and b's are overlap factors, M's are transitional matrix elements, and "$\cdots$" denotes higher excited state contributions. We observe that if we define a new set of correlators by taking weighted averages between adjacent timeslices in t as

$$\begin{aligned} C'_{\text{2pt}}(t) &\equiv e^{-m_{\text{snk}}}C_{\text{2pt}}(t) + C_{\text{2pt}}(t+1), \\ C'_{\text{3pt}}(t,\tau) &\equiv e^{-m_{\text{snk}}}C_{\text{3pt}}(t,\tau) + C_{\text{2pt}}(t+1,\tau) \end{aligned} \tag{4.53}$$

the spectral decomposition of $C'_{2\text{pt}}$ and $C'_{3\text{pt}}$ stays the same, except sink overlap factors for all states (including excited state) become

$$\begin{aligned} a_{+i} &\to a_{+i}\big(e^{-m_{\text{snk}}} + e^{-m_{+i}}\big) \\ a_{-i} &\to a_{-i}\big(e^{-m_{\text{snk}}} - e^{-m_{-i}}\big),\ \forall i \in \{0, 1, \cdots\} \end{aligned} \tag{4.54}$$

So if we choose the tunable parameters m_{snk} to be roughly equal one of the negative parity mass m_{-i}, the contribution of that particular state will be strongly suppressed. We call this procedure (weighted) time averaging at the sink since it suppresses sink overlap factors. Furthermore, we can apply this procedure iteratively to suppress any number of negative parity states.

We can similarly define a new set of operators by taking weighted time averages between adjacent τ's (for three-point correlators) to get

$$\begin{aligned} C'_{2\text{pt}}(t) &\equiv e^{-m_{\text{src}}} C_{2\text{pt}}(t) + C_{2\text{pt}}(t+1), \\ C'_{3\text{pt}}(t,\tau) &\equiv e^{-m_{\text{src}}} C_{3\text{pt}}(t,\tau) + C_{2\text{pt}}(t,\tau+1) \end{aligned} \tag{4.55}$$

In this case, spectral decomposition again remain intact except source overlap factors become

$$\begin{aligned} b_{+i} &\to b_{+i}\big(e^{-m_{\text{src}}} + e^{-m_{+i}}\big) \\ b_{-i} &\to b_{-i}\big(e^{-m_{\text{src}}} - e^{-m_{-i}}\big),\ \forall i \in \{0, 1, \cdots\} \end{aligned} \tag{4.56}$$

We can again suppress source overlap factors from negative parity states by choosing appropriate m_{src}, and we call this time averaging at the source.

Time averages at the source and sink commute with each other so we can apply them in arbitrary ordering. They are analogous to quark smearing but in the time direction, so excessive time averaging will again reduce the data quality. Based on effective mass plot we time average twice both at the source and sink with $m_{\text{src}}/m_{\text{snk}}$ parameters of 0.9 and 1.1.

This then significantly reduces excited state contribution from negative parity channels; see Fig. 2 and 3 of [3]. We apply the same operation to all correlators with different classes.

Variational method

The last step in the preprocessing pipeline is to reduce the number of correlators by marginalizing over class indices. This is achieved by applying the variational method [117]. As alluded to earlier in Section. 4.1.2, we start by solving for the left and right eigenvectors of two-point correlators in GEVPs

$$\begin{aligned} \mathbf{C}_{\mathrm{2pt}}^{16+,0;(R_1,R_2)}(t)v_R^{(0)} &= \lambda^{(0)}\mathbf{C}_{\mathrm{2pt}}^{16+,0;(R_1,R_2)}(t_0)v_R^{(0)}, \\ \left(v_L^{(0)}\right)^T\mathbf{C}_{\mathrm{2pt}}^{16+,0;(R_1,R_2)}(t) &= \lambda^{(0)}\left(v_L^{(0)}\right)^T\mathbf{C}_{\mathrm{2pt}}^{16+,0;(R_1,R_2)}(t_0) \end{aligned} \tag{4.57}$$

where we have reproduced equations from (4.20) for the ground state nucleon. We only make use of the eigenvalue $\lambda^{(0)}$ in our nucleon mass work. In this work, we aim to reduce the complexity of fitting by decreasing the number of correlators. We achieve this by sandwiching correlators matrices between left and right eigenvectors to obtain a single correlator for each matrix

$$\begin{aligned} C_{\mathrm{2pt}}^{16+,0}(t) &\equiv \left(v_L^{(0)}\right)^T\mathbf{C}_{\mathrm{2pt}}^{16+,0;(R_1,R_2)}(t)v_R^{(0)} \\ C_{\mathrm{3pt,V}}^{16+,0}(t,\tau) &\equiv \left(v_L^{(0)}\right)^T\mathbf{C}_{\mathrm{3pt,V}}^{16+,0;(R_1,R_2)}(t,\tau)v_R^{(0)} \\ C_{\mathrm{3pt,A}}^{16+,0}(t,\tau) &\equiv \left(v_L^{(0)}\right)^T\mathbf{C}_{\mathrm{3pt,A}}^{16+,0;(R_1,R_2)}(t,\tau)v_R^{(0)} \end{aligned} \tag{4.58}$$

Correlators on the left-hand sides of (4.58) are simpler to fit not only because there are fewer of them, but also because they have less severe excited state contaminations because we are essentially designing improved source and sink interpolators with better overlaps to nucleon-like states by taking linear combinations of existing operators. Coefficients needed for those linear combinations are given by the eigenvectors. We need to determine which t

and t_0 to be used for finding eigenvectors. We have found empirically that correlators are almost identical for any large t and t_0 (see Fig. 1 of [3] for differences in correlators from using different t and t_0), so we choose $t_0 = 6$ and $t - t_0 = 2$ in this analysis.

After passing correlator matrices through the three-step preprocessing pipeline, we obtain three correlators $C^{16,0;\sigma}_{\text{3pt,V}}(t,\tau)$, $C^{16,0;\sigma}_{\text{3pt,A}}(t,\tau)$, and $C^{16+,0;\sigma}_{\text{2pt}}(t)$ where the additional $\sigma = 0.2, 0.6$ fm denote different levels of quark smearings at the sink. We fit them to functional forms of

$$
\begin{aligned}
C^{16+,0;\sigma}_{\text{2pt}}(t) ={}& \sum_{i=0}^{1} a^{(\sigma)}_{+i} b_{+i} e^{-m_{+i}t} + a^{(\sigma)}_{-0} b_{-0} (-1)^t e^{-m_{-0}t} \\
C^{16,0;\sigma}_{\text{3pt,V}}(t,\tau) ={}& \sum_{i=0}^{1} a^{(\sigma)}_{+i} V_{+i,+i} b_{+i} e^{-m_{+i}t} + \\
& (-1)^t a^{(\sigma)}_{-0} V_{-0,-0} b_{-0} e^{-m_{-0}t} + \\
& (-1)^\tau \sum_{i=0}^{1} a^{(\sigma)}_{+i} V_{+i,-0} b_{-0} e^{-m_{-0}\tau} e^{-m_{+i}(t-\tau)} + \\
& (-1)^{t-\tau} \sum_{i=0}^{1} a^{(\sigma)}_{-0} V_{-0,+i} b_{+i} e^{-m_{+i}\tau} e^{-m_{-0}(t-\tau)} \\
C^{16,0;\sigma}_{\text{3pt,A}}(t,\tau) ={}& \sum_{i,j=0}^{1} a^{(\sigma)}_{+j} A_{+j,+i} b_{+i} e^{-m_{+i}\tau} e^{-m_j(t-\tau)} + \\
& (-1)^t a^{(\sigma)}_{-0} A_{-0,-0} b_{-0} e^{-m_{-0}t} + \\
& (-1)^\tau \sum_{i=0}^{1} a^{(\sigma)}_{+i} A_{+i,-0} b_{-0} e^{-m_{-0}\tau} e^{-m_{+i}(t-\tau)} + \\
& (-1)^{t-\tau} \sum_{i=0}^{1} a^{(\sigma)}_{-0} A_{-0,+i} b_{+i} e^{-m_{+i}\tau} e^{-m_{-0}(t-\tau)}
\end{aligned}
\tag{4.59}
$$

The notation here is almost identical to that of (4.49) and (4.14) except that the class superscripts (R_1) and (R_2) are removed as we are no longer dealing with matrices of correlators. Instead, we place $\sigma = 0.2, 0.6$ fm superscripts on sink overlap factors a to label the two sets of correlators Gr2.0N30 and Gr6.0N70. We only include two positive parity states (one nucleon-like state and one excited state) and a single negative parity state. Note that $C^{16,0;\sigma}_{\mathrm{3pt,V}}(t,\tau)$ has a slightly different spectral decomposition than $C^{16,0;\sigma}_{\mathrm{3pt,V}}(t,\tau)$ as $V_{+i,+j} = 0$ for $i \neq j$. This is because the vector current is conserved in the continuum limit so we expect $V_{+i,+j}$ to be small due to discretization effects. In practice, the data are too noisy to resolve such small values so we just set them to zeros and omit those terms.

4.2.5 Simulation and analysis details

As the first proof-of-principle work on calculating nucleon matrix elements with valence staggered quarks, we use a single 2+1+1 HISQ ensemble produced by the MILC collaboration [4, 55] with the lattice spacing of $a = 0.1222(3)$ fm determined from the f_{p4s} scheme [4], pion mass of $m_\pi \approx 305$ MeV, $m_s/m_l = 5$ where m_s and m_l are strange- and light- quark masses, and physical charm-quark mass. Using an unphysical pion-mass ensemble allows us to explore subtleties involving staggered baryon three-point correlator analyses without spending a significant amount of computing resources. Once the analysis methodology is demonstrated and established, we can then perform calculations on physical ensembles in the future.

We simultaneously fit optimized two- and three- correlators with both quark smearings to (4.59) within the Bayesian framework [99] to extract the nucleon mass $m_{+0} = m_N$, bare vector charge $\widetilde{g}_V$, and bare axial charge $\widetilde{g}_A$. We then renormalize bare charges with $Z_V = Z_A$ and compare the results. We could in principle fit both vector and axial-vector three-point correlators in one fit. However, we have found the dominant sources of excited state contaminations in those two correlators are different based on the observed three- to two-point correlator ratios [3]. For this reason, we perform two separate fits: one fit that includes both two-point correlators and vector three-point correlators and another fit that includes the same two-point correlators and axial-vector three-point correlators.

Similar priors are used in both fits. We impose a wide Gaussian prior of 1100(200) MeV on the nucleon mass m_N based on the observed nucleon masses on ensembles at similar unphysical pion masses [108–110]; we impose a wide Gaussian prior of 1600(300) MeV on the mass of the negative parity state m_{-0} based on the expected mass of the S-wave nucleon-pion state that we observed in [2]; to ensure we obtain a higher excited state mass, we impose a log-normal prior on the difference in masses between the first excited state and the nucleon ground state $m_{+0} - m_{-0}$ of 300(200) MeV. The identity of this excited state is unknown, so we let the central value to be roughly equal to the pion mass and allow a large margin of 200 MeV to take into account of various possibilities; we impose Gaussian priors of 1.0(0.3) on $\widetilde{g}_V = V_{+0,+0}$ based on the charge conservation and 1.2(0.3) on $\widetilde{g}_A = A_{+0,+0}$ based on the PDG value [46]. Other transitional matrix elements have priors of 0(5) based on the typical values of matrix elements; finally, we do not impose any priors on the overlap factors. Once priors and appropriate time ranges, which will be shown in the figure, are chosen, we minimized the augmented χ^2 to obtain estimates on parameters. The errors on those parameters are estimated from 1000 bootstrap samples.

4.2.6 Fit results

We present the results of two- and three-point correlators in figures 4.6, 4.7, and 4.8. Figure 4.6 shows the results of two-point correlator fits with either vector (g_V fit) or axial-vector correlators (g_A fit) at two different sink quark smearings, Gr2.0N30 and Gr6.0N70. The posterior estimates on the nucleon mass are $m_N = 0.704(9)$ from the g_V fit and $m_N = 0.707(6)$ from the g_A fit. The g_V fit gives a larger uncertainty than the g_A fit, which also shows up as wider one-sigma uncertainty bands in the figure. This is mainly because vector three-point correlators are insensitive to the sink smearings that we applied. As can be seen in figure 4.7, both Gr2.0N30 and Gr6.0N70 correlators are almost identical, so different radii of quark smearings are not adding new information on excited state contaminations over which we try to marginalize. Axial three-point correlators in figure 4.8 on the other hand see appreciable differences between two quark smearings with reduced excited state contaminations[4]. Then it comes at no surprise that the g_A fit will give a better nucleon mass estimate than the g_V fit. So in this work we will use the g_A fit nucleon mass as the nominal value which is equal to $m_N = 1141(10)$ MeV.

How does our nucleon mass estimate fare against existing lattice results? The answer is tricky because different calculations that use different lattice actions with different pion masses can give rise to drastically different nucleon masses on the lattice. However, as mentioned earlier in the nucleon mass chapter that there is an empirically observed relationship that states

$$m_N(a) = 800 \text{ MeV} + m_\pi(a) \tag{4.60}$$

Nucleon masses computed in different simulations all seem to obey this relationship well [108–110]. If we apply this equation to extrapolation our nucleon mass result from $m_\pi = 305$ MeV to the physical point of $m_\pi = 135$ MeV, we found $m_N = 970(10)$ MeV. This is consistent within one-sigma uncertainty with our nucleon mass result $m_N = 960(9)$ on the same lattice spacing from $\widetilde{\lambda}^{(0)}$ fit from Table 4.2.

Figures 4.7 and 4.8 show the results on three-point correlators. The posterior estimates on bare charges are $\widetilde{g}_V = 1.03(2)$ and $\widetilde{g}_A = 1.24(5)$. Despite being insensitive to quark smearings, we can see from figures that vector correlators inherently have less excited state contaminations than axial correlators, so the bare vector charge has a smaller fractional uncertainty than the axial charge. Using the renormalization constant $Z_V = Z_A = 0.991(1)$

---

[4] The curvature of a correlator, barring from large cancellations between different exponentials in the spectral decomposition, indicates the amount of excited state contaminations to the ground state.

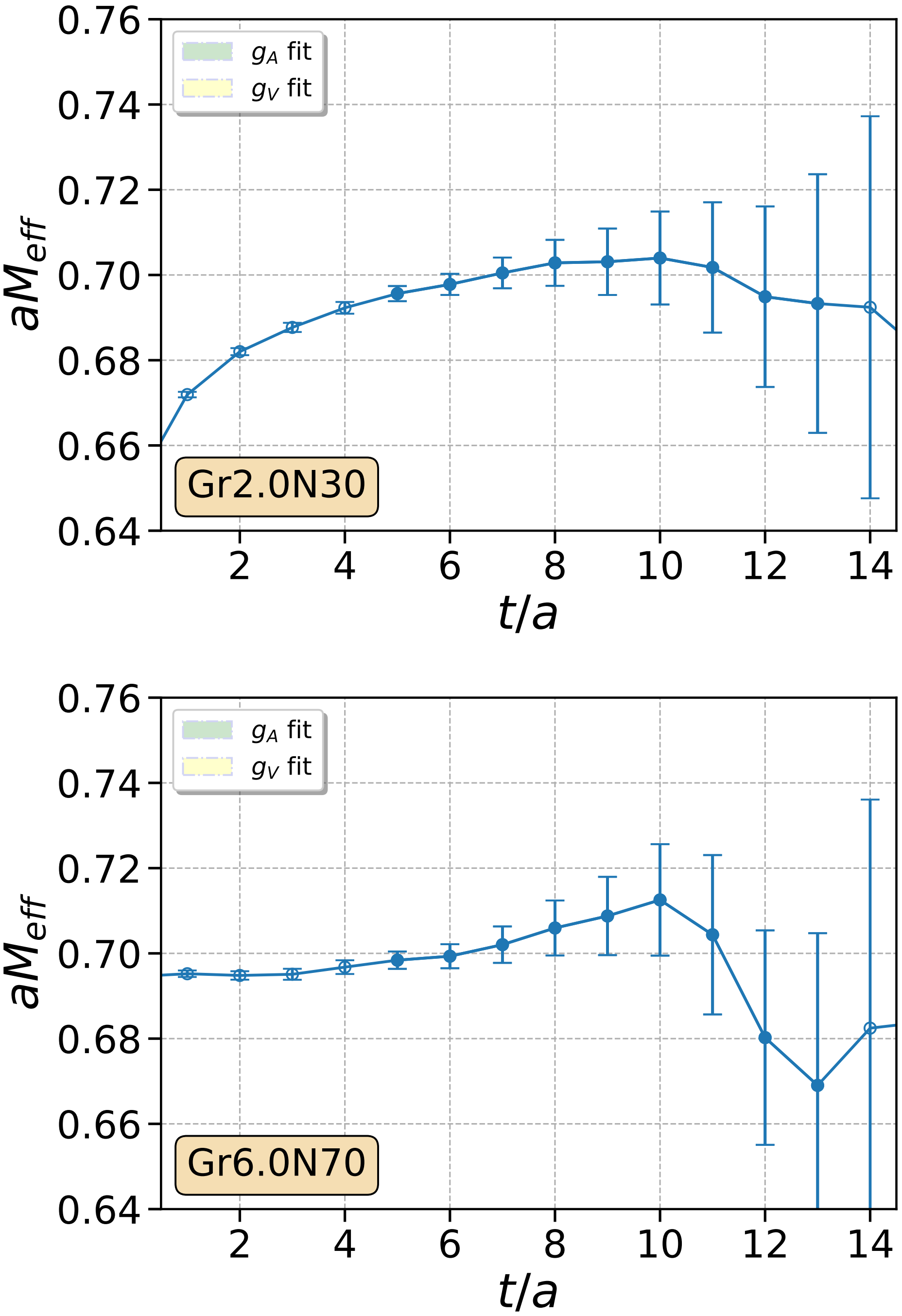

Figure 4.6: Effective masses, defined in (4.16), of the optimized two-point correlators as functions of the source-sink separation t. The top panel shows the Gr2.0N30 correlator (Gaussian smeared at sink with $\sigma = 0.2$ fm and 50 iterations) and the bottom one shows the Gr6.070N correlator ($\sigma = 0.6$ fm and 70 iterations). Solid points are those included in the Bayesian fits. Green bands show one-sigma posterior estimate of the fit with axial-vector correlators, and yellow bands show one-sigma posterior estimate of the fit with vector correlators. This figure is reproduced from our work in [3].

we get

$$
\begin{aligned}
g_V &= Z_V \widetilde{g}_V = 1.02(2) \\
g_A &= Z_A \widetilde{g}_A = 1.23(5) \\
\frac{g_A}{g_V} &= \frac{\widetilde{g}_A}{\widetilde{g}_V} = 1.21(5)
\end{aligned}
\tag{4.61}
$$

The fact that g_V is consistent with one provides a non-trivial cross check to the lattice methodology we presented here. We also present two determinations of g_A: the first result in the second line of the equation shows the renormalized charge by using the same renormalization constant as $\widetilde{g}_V$; on the other hand, the second result from the third line is renormalized by taking the ratio of unrenormalized charges. In both cases, results are consistent with each other within one-sigma uncertainty. Renormalized charges derived here cannot be compared to the continuum value of $g_A \approx 1.27$ because various systematic errors are not yet quantified. However, our results are consistent with other lattice calculations at similar quark masses albeit with different actions; see [3] for a detailed comparison between various lattice results.

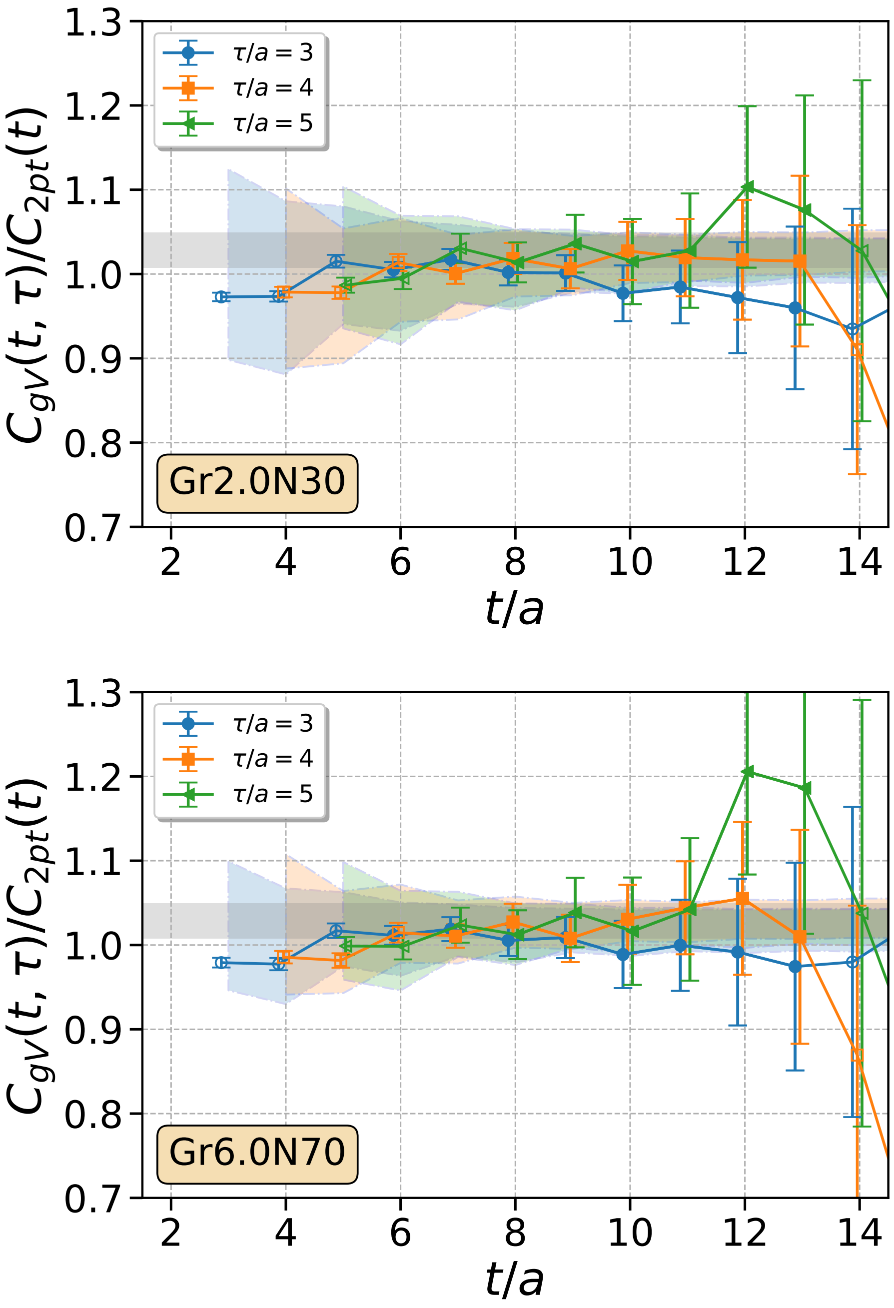

Figure 4.7: Optimized three- to two-point correlator ratio for vector correlators as functions of the source-sink separation time t and current insertion time τ. The top and bottom panels show results of Gr2.0N30 (Gaussian smeared at sink with $\sigma = 0.2$ fm and 50 iterations) and Gr6.0N70 correlators ($\sigma = 0.6$ fm and 70 iterations). Solid data points are those included in the simultaneous Bayesian fit with two-point correlators. Blue, orange, and green color bands show one-sigma posterior estimates for different τ's. The grey band shows the one-sigma posterior estimate on the bare vector charge $\widetilde{g}_V = 1.03(2)$. This figure is reproduced from our work in [3].

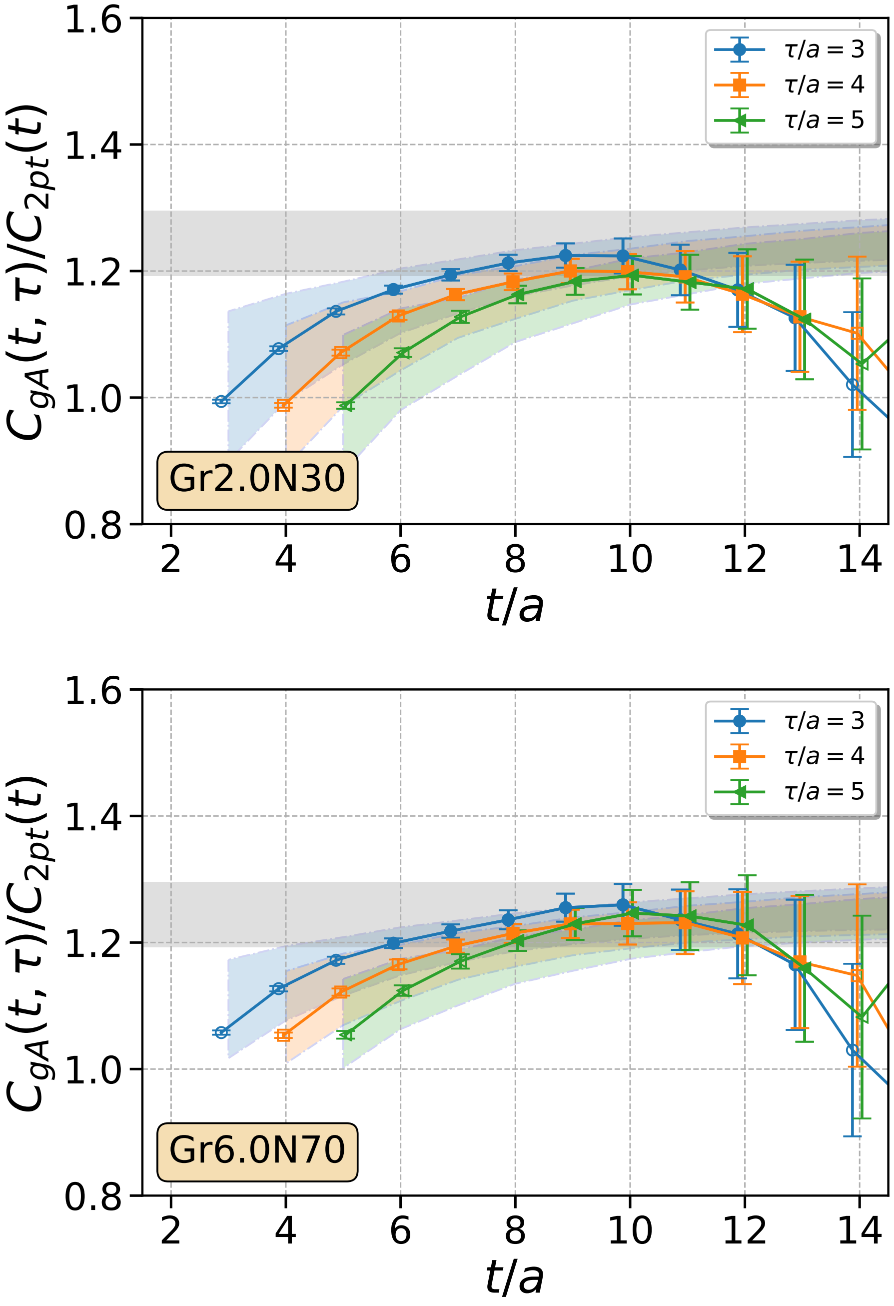

Figure 4.8: Same plot as figure 4.7 but for axial-vector three-point correlators. The grey band shows the one-sigma posterior estimate on the bare axial charge $\widetilde{g}_A = 1.24(5)$. This figure is reproduced from our work in [3].

Chapter 5

Conclusion and future work

In this dissertation, we introduced a group-theoretical method to calculate nucleon masses and matrix elements with staggered fermions. In the valence sector, the staggered action has four extra fermion tastes for each quark flavor that are degenerate in the continuum limit. Staggered QCD, therefore, simulates an augmented QCD theory but with $4 \times n_f = 8$ light, valence quarks and n_f light, sea quarks due to rooted quark determinants. $n_f = 2$ is the number of light quarks in the real world (up and down).

To relate observables with non-trivial taste quantum numbers calculated in staggered QCD to the ones in physical QCD with the correct number of valence quarks, we note that single-taste observables, or observables constructed with valence quarks of the same taste, must take on the same values in both theories [3, 82]. Non-single-taste observables, which are oftentimes much easier to work with in analyses, can then be "rotated" with successive applications of the generalized Wigner-Eckart theorem in the taste-flavor space to the single-taste ones. Ratios of single-taste to non-single-taste observables are then given by the ratios of Clebsch-Gordan coefficients that we worked out in Chapter 2. In addition, we also worked out, for the first time, the exact spin-flavor-taste quantum numbers of staggered nucleons in Chapter 3 and applied results from those two chapters to give the first complete calculations of the nucleon mass, vector charge, and axial charge with staggered fermions [2, 3].

This work demonstrates that staggered quarks are equally useful in simulating baryon physics as any other lattice fermions. It is just the beginning of a research program that ultimately aims to provide a precise calculation of the nucleon axial form factor, which can be used as an input to predict neutrino-nuclei cross sections in the CCQE region for neutrino oscillation experiments such as DUNE. What else we need to do to achieve such a calculation? Our discussions of the continuum representation theory in Chapter 2 generalizes trivially to form factor calculations since the translational symmetry that gives rise to finite momentum transfers commutes with the internal flavor-taste symmetry. Also, the same Wigner-Eckart type analysis can be applied to extract physical form factors. However, the spectra of non-zero-momentum lattice operators, obtained by adding momenta to zero-momentum operators presented in Chapter 3, are complicated by the mixing between irreps. For example, if we insert one unit of lattice momentum in the z-direction to the isospin-3/2, 16 irrep operators we use in this work, operators will now interpolate to one nucleon-like and five Δ-like states as opposed to one nucleon-like and three Δ-like states at zero momentum; see the appendix of [118] for details. We are currently exploring the optimal strategy for the nucleon axial form factor simulations. The first result on an unphysical pion ensemble will appear in the near future.

Even though we focus solely on computing nucleon masses and matrix elements in this work, the methodology we presented here is quite general and should be applicable to many other calculations. For example, operators in other lattice irreps and/or with different valence quark masses can be used to investigate the properties of Δ baryons, nucleon-pion scattering, or Ω baryons. Physical observables are still given by the single-taste observables in the staggered formalism, and we have to repeat the exercises in Chapter 2 and 3 to know how to properly normalize staggered observables. The usefulness of staggered simulations is ultimately limited by i) our ability to performance group-theoretical analyses to extract normalization factors and ii) the spectrum complexity of staggered observables. I do not imagine i) will pose too much of an issue as there are existing computer programs that can automate the processes; ii) could potentially pose a serious challenge to analyses as the existence of many nearly degenerate states with different tastes leads to complicated error estimates and continuum extrapolations. For many observables, however, staggered simulations offer unparalleled efficiency and the analysis complications are minor setbacks compared to the extra computing costs with other lattice fermions. It is then up to the reader to perform a cost-benefit analysis to decide whether it is worth it to use staggered fermions in his or her simulations.

References

[1] J. A. Formaggio and G. P. Zeller, *"From eV to EeV: Neutrino Cross Sections Across Energy Scales,"* Rev. Mod. Phys. **84**, 1307 (2012), arXiv:1305.7513 [hep-ex] .

[2] Y. Lin, A. S. Meyer, C. Hughes, A. S. Kronfeld, J. N. Simone, and A. Strelchenko, *"Nucleon mass with highly improved staggered quarks,"* Phys. Rev. D **103**, 034501 (2021), arXiv:1911.12256 [hep-lat] .

[3] Y. Lin, A. S. Meyer, S. Gottlieb, C. Hughes, A. S. Kronfeld, J. N. Simone, and A. Strelchenko, *"Computing Nucleon Charges with Highly Improved Staggered Quarks,"* Phys. Rev. D **103**, 054510 (2021), arXiv:2010.10455 [hep-lat] .

[4] A. Bazavov *et al.*, *"B- and D-meson leptonic decay constants from four-flavor lattice QCD,"* Phys. Rev. D **98**, 074512 (2018), arXiv:1712.09262 [hep-lat] .

[5] Y. Fukuda *et al.* (Super-Kamiokande), *"Evidence for oscillation of atmospheric neutrinos,"* Phys. Rev. Lett. **81**, 1562 (1998), arXiv:hep-ex/9807003 .

[6] I. Esteban, M. C. Gonzalez-Garcia, M. Maltoni, T. Schwetz, and A. Zhou, *"The fate of hints: updated global analysis of three-flavor neutrino oscillations,"* JHEP **09**, 178 (2020), arXiv:2007.14792 [hep-ph] .

[7] J. Lesgourgues and S. Pastor, *"Neutrino mass from Cosmology,"* Adv. High Energy Phys. **2012**, 608515 (2012), arXiv:1212.6154 [hep-ph] .

[8] Y. Y. Y. Wong, *"Neutrino mass in cosmology: status and prospects,"* Ann. Rev. Nucl. Part. Sci. **61**, 69 (2011), arXiv:1111.1436 [astro-ph.CO] .

[9] S. W. Li, L. F. Roberts, and J. F. Beacom, *"Exciting Prospects for Detecting Late-Time Neutrinos from Core-Collapse Supernovae,"* Phys. Rev. D **103**, 023016 (2021), arXiv:2008.04340 [astro-ph.HE] .

[10] M. Fukugita and T. Yanagida, *"Baryogenesis Without Grand Unification,"* Phys. Lett. B **174**, 45 (1986).

[11] S. Davidson, E. Nardi, and Y. Nir, *"Leptogenesis,"* Phys. Rept. **466**, 105 (2008), arXiv:0802.2962 [hep-ph] .

[12] M. J. Dolinski, A. W. P. Poon, and W. Rodejohann, *"Neutrinoless Double-Beta Decay: Status and Prospects,"* Ann. Rev. Nucl. Part. Sci. **69**, 219 (2019), arXiv:1902.04097 [nucl-ex] .

[13] D. Q. Adams *et al.* (CUORE), *"Improved Limit on Neutrinoless Double-Beta Decay in* ^{130}*Te with CUORE,"* Phys. Rev. Lett. **124**, 122501 (2020), arXiv:1912.10966 [nucl-ex] .

[14] M. Agostini *et al.* (GERDA), *"Probing Majorana neutrinos with double-β decay,"* Science **365**, 1445 (2019), arXiv:1909.02726 [hep-ex] .

[15] A. Gando *et al.* (KamLAND-Zen), *"Search for Majorana Neutrinos near the Inverted Mass Hierarchy Region with KamLAND-Zen,"* Phys. Rev. Lett. **117**, 082503 (2016), [Addendum: Phys.Rev.Lett. 117, 109903 (2016)], arXiv:1605.02889 [hep-ex] .

[16] M. Aker *et al.* (KATRIN), *"Improved Upper Limit on the Neutrino Mass from a Direct Kinematic Method by KATRIN,"* Phys. Rev. Lett. **123**, 221802 (2019), arXiv:1909.06048 [hep-ex] .

[17] J. Schechter and J. W. F. Valle, *"Neutrinoless Double beta Decay in SU(2) x U(1) Theories,"* Phys. Rev. D **25**, 2951 (1982).

[18] P. F. de Salas, D. V. Forero, S. Gariazzo, P. Martínez-Miravé, O. Mena, C. A. Ternes, M. Tórtola, and J. W. F. Valle, *"2020 global reassessment of the neutrino oscillation picture,"* JHEP **02**, 071 (2021), arXiv:2006.11237 [hep-ph] .

[19] B. Abi *et al.* (DUNE), *"Volume I. Introduction to DUNE,"* JINST **15**, T08008 (2020), arXiv:2002.02967 [physics.ins-det] .

[20] F. An *et al.* (JUNO), *"Neutrino Physics with JUNO,"* J. Phys. G **43**, 030401 (2016), arXiv:1507.05613 [physics.ins-det] .

[21] M. A. Acero *et al.* (NOvA), *"First Measurement of Neutrino Oscillation Parameters using Neutrinos and Antineutrinos by NOvA,"* Phys. Rev. Lett. **123**, 151803 (2019), arXiv:1906.04907 [hep-ex] .

[22] R. Acciarri *et al.* (MicroBooNE), *"Design and Construction of the MicroBooNE Detector,"* JINST **12**, P02017 (2017), arXiv:1612.05824 [physics.ins-det] .

[23] C. Andreopoulos *et al.*, *"The GENIE Neutrino Monte Carlo Generator,"* Nucl. Instrum. Meth. A **614**, 87 (2010), arXiv:0905.2517 [hep-ph] .

[24] U. Mosel, *"Neutrino event generators: foundation, status and future,"* J. Phys. G **46**, 113001 (2019), arXiv:1904.11506 [hep-ex] .

[25] J. Żmuda, K. M. Graczyk, C. Juszczak, and J. T. Sobczyk, *"NuWro Monte Carlo generator of neutrino interactions - first electron scattering results,"* Acta Phys. Polon. B **46**, 2329 (2015), arXiv:1510.03268 [hep-ph] .

[26] L. Bagby *et al.* (ICARUS), *"Overhaul and Installation of the ICARUS-T600 Liquid Argon TPC Electronics for the FNAL Short Baseline Neutrino Program,"* JINST **16**, P01037 (2021), arXiv:2010.02042 [physics.ins-det] .

[27] L. Aliaga *et al.* (MINERvA), *"Design, Calibration, and Performance of the MINERvA Detector,"* Nucl. Instrum. Meth. A **743**, 130 (2014), arXiv:1305.5199 [physics.ins-det] .

[28] G. Karagiorgi (SBND), *"Liquid Argon TPC Trigger Development with SBND,"* in *Meeting of the Division of Particles and Fields of the American Physical Society* (2019) arXiv:1910.08218 [physics.ins-det] .

[29] K. Abe *et al.* (T2K), *"T2K ND280 Upgrade - Technical Design Report,"* (2019), arXiv:1901.03750 [physics.ins-det] .

[30] L. Alvarez-Ruso *et al.* (NuSTEC), *"NuSTEC White Paper: Status and challenges of neutrino–nucleus scattering,"* Prog. Part. Nucl. Phys. **100**, 1 (2018), arXiv:1706.03621 [hep-ph] .

[31] T. Katori and M. Martini, *"Neutrino–nucleus cross sections for oscillation experiments,"* J. Phys. G **45**, 013001 (2018), arXiv:1611.07770 [hep-ph] .

[32] K. G. Wilson, *"Confinement of quarks,"* Phys. Rev. D **10**, 2445 (1974).

[33] A. S. Kronfeld, D. G. Richards, W. Detmold, R. Gupta, H.-W. Lin, K.-F. Liu, A. S. Meyer, R. Sufian, and S. Syritsyn (USQCD), *"Lattice QCD and Neutrino-Nucleus Scattering,"* Eur. Phys. J. A **55**, 196 (2019), arXiv:1904.09931 [hep-lat] .

[34] A. Lovato, J. Carlson, S. Gandolfi, N. Rocco, and R. Schiavilla, *"Ab initio study of* $(\boldsymbol{\nu_\ell}, \boldsymbol{\ell^-})$ *and* $(\boldsymbol{\overline{\nu}_\ell}, \boldsymbol{\ell^+})$ *inclusive scattering in* ^{12}C*: confronting the MiniBooNE and T2K CCQE data,"* Phys. Rev. X **10**, 031068 (2020), arXiv:2003.07710 [nucl-th] .

[35] T. Kitagaki *et al.*, *"High-Energy Quasielastic Muon-neutrino n —> mu- p Scattering in Deuterium,"* Phys. Rev. D **28**, 436 (1983).

[36] N. Baker, A. Cnops, P. Connolly, S. Kahn, H. Kirk, M. Murtagh, R. Palmer, N. Samios, and M. Tanaka, *"Quasielastic Neutrino Scattering: A Measurement of the Weak Nucleon Axial Vector Form-Factor,"* Phys. Rev. D **23**, 2499 (1981).

[37] K. Miller *et al.*, *"STUDY OF THE REACTION muon-neutrino D —> MU- P P(S),"* Phys. Rev. D **26**, 537 (1982).

[38] A. S. Meyer, M. Betancourt, R. Gran, and R. J. Hill, *"Deuterium target data for precision neutrino-nucleus cross sections,"* Phys. Rev. D **93**, 113015 (2016), arXiv:1603.03048 [hep-ph] .

[39] L. Alvarez-Ruso, K. M. Graczyk, and E. Saul-Sala, *"Nucleon axial form factor from a Bayesian neural-network analysis of neutrino-scattering data,"* Phys. Rev. C **99**, 025204 (2019), arXiv:1805.00905 [hep-ph] .

[40] J. C. Bernauer *et al.* (A1), *"Electric and magnetic form factors of the proton,"* Phys. Rev. C **90**, 015206 (2014), arXiv:1307.6227 [nucl-ex] .

[41] W. Xiong *et al.*, *"A small proton charge radius from an electron–proton scattering experiment,"* Nature **575**, 147 (2019).

[42] K. Borah, R. J. Hill, G. Lee, and O. Tomalak, *"Parametrization and applications of the low-Q^2 nucleon vector form factors,"* Phys. Rev. D **102**, 074012 (2020), arXiv:2003.13640 [hep-ph] .

[43] G. S. Bali, L. Barca, S. Collins, M. Gruber, M. Löffler, A. Schäfer, W. Söldner, P. Wein, S. Weishäupl, and T. Wurm (RQCD), *"Nucleon axial structure from lattice QCD,"* JHEP **05**, 126 (2020), arXiv:1911.13150 [hep-lat] .

[44] E. Shintani, K.-I. Ishikawa, Y. Kuramashi, S. Sasaki, and T. Yamazaki, *"Nucleon form factors and root-mean-square radii on a (10.8 fm)^4 lattice at the physical point,"* Phys. Rev. D **99**, 014510 (2019), [Erratum: Phys.Rev.D 102, 019902 (2020)], arXiv:1811.07292 [hep-lat] .

[45] S. Park, R. Gupta, B. Yoon, S. Mondal, T. Bhattacharya, Y.-C. Jang, B. Joó, and F. Winter (Nucleon Matrix Elements (NME)), *"Precision Nucleon Charges and Form Factors Using 2+1-flavor Lattice QCD,"* (2021), arXiv:2103.05599 [hep-lat] .

[46] P. A. Zyla *et al.* (Particle Data Group), *"Review of Particle Physics,"* PTEP **2020**, 083C01 (2020).

[47] G. P. Lepage, *"Lattice QCD for novices,"* in *13th Annual HUGS AT CEBAF (HUGS 98)* (1998) arXiv:hep-lat/0506036 .

[48] R. Gupta, *"Introduction to lattice QCD: Course,"* in *Les Houches Summer School in Theoretical Physics, Session 68: Probing the Standard Model of Particle Interactions* (1997) arXiv:hep-lat/9807028 .

[49] T. DeGrand and C. DeTar, *Lattice Methods for Quantum Chromodynamics* (World Scientific, Singapore, 2006).

[50] M. Creutz, *Quarks, gluons and lattices*, Cambridge Monographs on Mathematical Physics (Cambridge Univ. Press, Cambridge, UK, 1985).

[51] C. Gattringer and C. B. Lang, *Quantum chromodynamics on the lattice*, Vol. 788 (Springer, Berlin, 2010).

[52] I. Montvay and G. Munster, *Quantum fields on a lattice*, Cambridge Monographs on Mathematical Physics (Cambridge University Press, 1997).

[53] R. P. Feynman, *The principle of least action in quantum mechanics*, Ph.D. thesis, Princeton U. (1942).

[54] M. Luscher, *"Computational Strategies in Lattice QCD,"* in *Les Houches Summer School: Session 93: Modern perspectives in lattice QCD: Quantum field theory and high performance computing* (2010) arXiv:1002.4232 [hep-lat] .

[55] A. Bazavov *et al.* (MILC), *"Lattice QCD Ensembles with Four Flavors of Highly Improved Staggered Quarks,"* Phys. Rev. D **87**, 054505 (2013), arXiv:1212.4768 [hep-lat] .

[56] G. P. Lepage, *"The analysis of algorithms for lattice field theory,"* in *Theoretical Advanced Study Institute in Elementary Particle Physics* (1989) pp. 97–120.

[57] G. Parisi, *"The Strategy for Computing the Hadronic Mass Spectrum,"* Phys. Rept. **103**, 203 (1984).

[58] H. Nielsen and M. Ninomiya, *"Absence of neutrinos on a lattice: (i). proof by homotopy theory,"* Nuclear Physics B **185**, 20 (1981).

[59] H. Nielsen and M. Ninomiya, *"Absence of neutrinos on a lattice: (ii). intuitive topological proof,"* Nuclear Physics B **193**, 173 (1981).

[60] H. Nielsen and M. Ninomiya, *"A no-go theorem for regularizing chiral fermions,"* Physics Letters B **105**, 219 (1981).

[61] E. Poppitz and Y. Shang, *"Chiral Lattice Gauge Theories Via Mirror-Fermion Decoupling: A Mission (im)Possible?"* Int. J. Mod. Phys. A **25**, 2761 (2010), arXiv:1003.5896 [hep-lat] .

[62] M. Luscher, *"Chiral gauge theories revisited,"* Subnucl. Ser. **38**, 41 (2002), arXiv:hep-th/0102028 .

[63] M. Golterman, *"Lattice chiral gauge theories,"* Nucl. Phys. B Proc. Suppl. **94**, 189 (2001), arXiv:hep-lat/0011027 .

[64] D. B. Kaplan, *"A Method for simulating chiral fermions on the lattice,"* Phys. Lett. B **288**, 342 (1992), arXiv:hep-lat/9206013 .

[65] D. B. Kaplan, *"Chiral fermions on the lattice,"* Nuclear Physics B - Proceedings Supplements **30**, 597 (1993), proceedings of the International Symposium on.

[66] H. Neuberger, *"Exactly massless quarks on the lattice,"* Phys. Lett. B **417**, 141 (1998), arXiv:hep-lat/9707022 .

[67] H. Neuberger, *"A Practical implementation of the overlap Dirac operator,"* Phys. Rev. Lett. **81**, 4060 (1998), arXiv:hep-lat/9806025 .

[68] P. H. Ginsparg and K. G. Wilson, *"A Remnant of Chiral Symmetry on the Lattice,"* Phys. Rev. D **25**, 2649 (1982).

[69] J. B. Kogut and L. Susskind, *"Hamiltonian Formulation of Wilson's Lattice Gauge Theories,"* Phys. Rev. D **11**, 395 (1975).

[70] H. S. Sharatchandra, H. J. Thun, and P. Weisz, *"Susskind Fermions on a Euclidean Lattice,"* Nucl. Phys. B **192**, 205 (1981).

[71] A. S. Kronfeld, *"Lattice Gauge Theory with Staggered Fermions: How, Where, and Why (Not),"* PoS **LATTICE2007**, 016 (2007), arXiv:0711.0699 [hep-lat] .

[72] S. R. Sharpe, *"Rooted staggered fermions: Good, bad or ugly?"* PoS **LAT2006**, 022 (2006), arXiv:hep-lat/0610094 .

[73] M. Golterman, *"QCD with rooted staggered fermions,"* PoS **CONFINEMENT8**, 014 (2008), arXiv:0812.3110 [hep-ph] .

[74] G. C. Donald, C. T. H. Davies, E. Follana, and A. S. Kronfeld, *"Staggered fermions, zero modes, and flavor-singlet mesons,"* Phys. Rev. D **84**, 054504 (2011), arXiv:1106.2412 [hep-lat] .

[75] S. Durr and C. Hoelbling, *"Lattice fermions with complex mass,"* Phys. Rev. D **74**, 014513 (2006), arXiv:hep-lat/0604005 .

[76] A. Bazavov *et al.* (Fermilab Lattice, MILC, TUMQCD), *"Up-, down-, strange-, charm-, and bottom-quark masses from four-flavor lattice QCD,"* Phys. Rev. D **98**, 054517 (2018), arXiv:1802.04248 [hep-lat] .

[77] C. Aubin, C. Bernard, C. E. DeTar, J. Osborn, S. Gottlieb, E. B. Gregory, D. Toussaint, U. M. Heller, J. E. Hetrick, and R. Sugar (MILC), *"Light pseudoscalar decay constants, quark masses, and low energy constants from three-flavor lattice QCD,"* Phys. Rev. D **70**, 114501 (2004), arXiv:hep-lat/0407028 .

[78] G. W. Kilcup and S. R. Sharpe, *"A Tool Kit for Staggered Fermions,"* Nucl. Phys. B **283**, 493 (1987).

[79] M. F. L. Golterman, *"Staggered mesons,"* Nucl. Phys. B **273**, 663 (1986).

[80] S. Aoki *et al.* (Flavour Lattice Averaging Group), *"FLAG Review 2019: Flavour Lattice Averaging Group (FLAG),"* Eur. Phys. J. C **80**, 113 (2020), arXiv:1902.08191 [hep-lat] .

[81] M. F. L. Golterman and J. Smit, *"Lattice Baryons With Staggered Fermions,"* Nucl. Phys. B **255**, 328 (1985).

[82] J. A. Bailey, *"Staggered baryon operators with flavor SU(3) quantum numbers,"* Phys. Rev. D **75**, 114505 (2007), arXiv:hep-lat/0611023 .

[83] E. Follana, Q. Mason, C. Davies, K. Hornbostel, G. P. Lepage, J. Shigemitsu, H. Trottier, and K. Wong (HPQCD, UKQCD), *"Highly improved staggered quarks on the lattice, with applications to charm physics,"* Phys. Rev. D **75**, 054502 (2007), arXiv:hep-lat/0610092 .

[84] A. Alex, M. Kalus, A. Huckleberry, and J. von Delft, *"A Numerical algorithm for the explicit calculation of SU(N) and SL(N,C) Clebsch-Gordan coefficients,"* J. Math. Phys. **52**, 023507 (2011), arXiv:1009.0437 [math-ph] .

[85] K. Hecht and S. C. Pang, *“On the wigner supermultiplet scheme,”* J. Math. Phys. **10**, 1571 (1969).

[86] E. Condon and G. Shortley, *The Theory of Atomic Spectra*, Cambridge Univ.Pr.209 (Cambridge University Press, 1935).

[87] Y. Ne’eman, *“Derivation of strong interactions from a gauge invariance,”* Nucl. Phys. **26**, 222 (1961).

[88] M. Gell-Mann, *“The Eightfold Way: A Theory of strong interaction symmetry,”* (1961), 10.2172/4008239.

[89] R. C. Johnson, *“ANGULAR MOMENTUM ON A LATTICE,”* Phys. Lett. B **114**, 147 (1982).

[90] S. Basak, R. Edwards, G. T. Fleming, U. M. Heller, C. Morningstar, D. Richards, I. Sato, and S. J. Wallace (Lattice Hadron Physics (LHPC)), *“Clebsch-Gordan construction of lattice interpolating fields for excited baryons,”* Phys. Rev. D **72**, 074501 (2005), arXiv:hep-lat/0508018 .

[91] C. Hughes, Y. Lin, and A. S. Meyer, *“Nucleon and Ω Baryon Masses with All-HISQ Fermions at the Physical Point,”* PoS **LATTICE2019**, 057 (2019), arXiv:1912.00028 [hep-lat] .

[92] S. Borsanyi *et al.*, *“Leading hadronic contribution to the muon magnetic moment from lattice QCD,”* (2020), arXiv:2002.12347 [hep-lat] .

[93] N. Miller *et al.*, *“Scale setting the M\”obius Domain Wall Fermion on gradient-flowed HISQ action using the omega baryon mass and the gradient-flow scales t_0 and w_0,”* (2020), arXiv:2011.12166 [hep-lat] .

[94] C. C. Chang *et al.*, *“A per-cent-level determination of the nucleon axial coupling from quantum chromodynamics,”* Nature **558**, 91 (2018), arXiv:1805.12130 [hep-lat] .

[95] R. Gupta, Y.-C. Jang, B. Yoon, H.-W. Lin, V. Cirigliano, and T. Bhattacharya, *“Isovector Charges of the Nucleon from 2+1+1-flavor Lattice QCD,”* Phys. Rev. D **98**, 034503 (2018), arXiv:1806.09006 [hep-lat] .

[96] M. A. Clark, B. Joó, A. Strelchenko, M. Cheng, A. Gambhir, and R. Brower, *“Accelerating Lattice QCD Multigrid on GPUs Using Fine-Grained Parallelization,”* (2016), arXiv:1612.07873 [hep-lat] .

[97] R. C. Brower, M. A. Clark, D. Howarth, and E. S. Weinberg, *“Multigrid for chiral lattice fermions: Domain wall,”* Phys. Rev. D **102**, 094517 (2020), arXiv:2004.07732 [hep-lat] .

[98] R. C. Brower, M. A. Clark, A. Strelchenko, and E. Weinberg, *"Multigrid algorithm for staggered lattice fermions,"* Phys. Rev. D **97**, 114513 (2018), arXiv:1801.07823 [hep-lat] .

[99] G. P. Lepage, B. Clark, C. T. H. Davies, K. Hornbostel, P. B. Mackenzie, C. Morningstar, and H. Trottier, *"Constrained curve fitting,"* Nucl. Phys. B Proc. Suppl. **106**, 12 (2002), arXiv:hep-lat/0110175 .

[100] C. M. Bouchard, G. P. Lepage, C. Monahan, H. Na, and J. Shigemitsu, *"$B_s \to K\ell\nu$ form factors from lattice QCD,"* Phys. Rev. D **90**, 054506 (2014), arXiv:1406.2279 [hep-lat] .

[101] B. EFRON, *"Nonparametric estimates of standard error: The jackknife, the bootstrap and other methods,"* Biometrika **68**, 589 (1981), https://academic.oup.com/biomet/article-pdf/68/3/589/581658/68-3-589.pdf .

[102] C. Michael and I. Teasdale, *"Extracting Glueball Masses From Lattice QCD,"* Nucl. Phys. B **215**, 433 (1983).

[103] A. S. Kronfeld, *"Improved Methods for Computing Masses from Numerical Simulations,"* Nucl. Phys. B Proc. Suppl. **17**, 313 (1990).

[104] M. Luscher and U. Wolff, *"How to Calculate the Elastic Scattering Matrix in Two-dimensional Quantum Field Theories by Numerical Simulation,"* Nucl. Phys. B **339**, 222 (1990).

[105] B. Blossier, M. Della Morte, G. von Hippel, T. Mendes, and R. Sommer, *"On the generalized eigenvalue method for energies and matrix elements in lattice field theory,"* JHEP **04**, 094 (2009), arXiv:0902.1265 [hep-lat] .

[106] C. DeTar and S.-H. Lee, *"Variational method with staggered fermions,"* Phys. Rev. D **91**, 034504 (2015), arXiv:1411.4676 [hep-lat] .

[107] A. Hart, G. M. von Hippel, and R. R. Horgan (HPQCD), *"Radiative corrections to the lattice gluon action for HISQ improved staggered quarks and the effect of such corrections on the static potential,"* Phys. Rev. D **79**, 074008 (2009), arXiv:0812.0503 [hep-lat] .

[108] A. Walker-Loud, *"Baryons in/and Lattice QCD,"* PoS **CD12**, 017 (2013), arXiv:1304.6341 [hep-lat] .

[109] A. Walker-Loud, *"New lessons from the nucleon mass, lattice QCD and heavy baryon chiral perturbation theory,"* PoS **LATTICE2008**, 005 (2008), arXiv:0810.0663 [hep-lat] .

[110] A. Walker-Loud, *"Nuclear Physics Review,"* PoS **LATTICE2013**, 013 (2014), arXiv:1401.8259 [hep-lat] .

[111] G. P. Lepage, "gplepage/corrfitter: corrfitter version 8.1," (2020).

[112] W. I. Jay and E. T. Neil, *"Bayesian model averaging for analysis of lattice field theory results,"* (2020), arXiv:2008.01069 [stat.ME] .

[113] S. R. Sharpe, *"B(K) Using staggered fermions: An update,"* Nucl. Phys. B Proc. Suppl. **34**, 403 (1994), arXiv:hep-lat/9312009 .

[114] D. Hatton, C. T. H. Davies, G. P. Lepage, and A. T. Lytle (HPQCD), *"Renormalizing vector currents in lattice QCD using momentum-subtraction schemes,"* Phys. Rev. D **100**, 114513 (2019), arXiv:1909.00756 [hep-lat] .

[115] S. Gusken, *"A Study of smearing techniques for hadron correlation functions,"* Nucl. Phys. B Proc. Suppl. **17**, 361 (1990).

[116] G. S. Bali, B. Lang, B. U. Musch, and A. Schäfer, *"Novel quark smearing for hadrons with high momenta in lattice QCD,"* Phys. Rev. D **93**, 094515 (2016), arXiv:1602.05525 [hep-lat] .

[117] B. J. Owen, J. Dragos, W. Kamleh, D. B. Leinweber, M. S. Mahbub, B. J. Menadue, and J. M. Zanotti, *"Variational Approach to the Calculation of gA,"* Phys. Lett. B **723**, 217 (2013), arXiv:1212.4668 [hep-lat] .

[118] A. S. Meyer, *The Nucleon Axial Form Factor and Staggered Lattice QCD*, Ph.D. thesis, Chicago U. (2017).